Ferromagnetic Thin and Ultra-Thin Film Alloys of Manganese and Iron with Gallium and Their Structural, Electronic, and Magnetic Properties

A dissertation presented to

the faculty of

the College of Arts and Sciences of Ohio University

In partial fulfillment

of the requirements for the degree

Doctor of Philosophy

Andrada Oana Mandru

April 2016

This dissertation titled

Ferromagnetic Thin and Ultra-Thin Film Alloys of Manganese and Iron with Gallium and Their Structural, Electronic, and Magnetic Properties

by

ANDRADA OANA MANDRU

has been approved for

the Department of Physics and Astronomy

and the College of Arts and Sciences by

Arthur R. Smith

Professor of Physics and Astronomy

Robert Frank

Dean, College of Arts and Sciences

Abstract

MANDRU, ANDRADA OANA, Ph.D., April 2016, Physics

Ferromagnetic Thin and Ultra-Thin Film Alloys of Manganese and Iron with Gallium and Their Structural, Electronic, and Magnetic Properties (140 pp.)

Director of Dissertation: Arthur R. Smith

The behavior of ferromagnetic alloys of manganese and iron with gallium when coupled with different magnetic and/or non-magnetic systems is investigated. The studies explore how the structural and electronic/magnetic properties vary with thickness and composition, probing systems in the sub-monolayer, ultra-thin, and thin film regimes. Molecular beam epitaxy is used to prepare clean sample surfaces that are subsequently investigated *in-situ* down to atomic level using scanning tunneling microscopy and Auger electron spectroscopy. A variety of *ex-situ* methods are also utilized to obtain information about the overall system properties, with additional theoretical calculations accompanying the experimental findings for two of the investigated systems.

The first study refers to $L1_0$-structured ferromagnetic MnGa(111) ultra-thin films grown on semiconducting GaN(0001) substrates under lightly Mn-rich conditions. Room-temperature scanning tunneling microscopy investigations reveal smooth and reconstructed terraces, with the surface structure consisting primarily of a hexagonal-like 2×2 reconstruction. Theoretical calculations are carried out using density functional theory, revealing that a Mn-rich 2×2 surface structure gives the best agreement with the observed experimental images and Auger electron spectroscopy surface composition investigations. It is found that under such growth conditions, the Mn atoms incorporate at different rates: surfaces become highly Mn-rich, while the bulk remains stoichiometric, making the MnGa system very sensitive to the ratio of elements in its structure. Such behavior reveals a potential recipe for tuning, for example, magnetic properties by carefully controlling the surface reconstruction during growth.

With the aim of understanding how the properties change as the growth conditions are varied, we also investigate the structure, surface, and magnetism of ferromagnetic Ga-rich MnGa thin and ultra-thin films grown again on GaN(0001). For this study, the Mn:Ga composition ratio is varied from ≈ 1 (stoichiometric) to ≈ 0.42 (very Ga-rich) for different samples. We find that the $L1_0$ MnGa phase is preserved down to a Mn:Ga ratio of ≈ 0.81. As the Ga concentration increases, we observe the coexistence of more Ga-rich phases, namely Mn_3Ga_5 and Mn_2Ga_5. Room temperature scanning tunneling microscopy imaging reveals highly epitaxial films, with atomically smooth and highly reconstructed surfaces. Magnetic characterizations show how the magnetic properties evolve with changing composition and that giant perpendicular magnetic anisotropy is induced by reducing the film thickness.

Next, the initial stages of interface formation for a real-world ferromagnet/antiferromagnet bi-layer system, iron/manganese nitride, is investigated down to the atomic scale using a combination of experiment and first-principles theoretical calculations. Sub-monolayer deposition of iron onto manganese nitride surfaces results in an unexpected yet well-ordered structural and magnetic arrangement. It is shown that although the island structures seen in scanning tunneling microscopy images are of single monolayer height, their chemical composition, based on Auger electron spectroscopy, conductance map imaging, and theoretical models, does not consist of iron. It is found theoretically that models that consider iron on the surface of manganese nitride are highly unfavorable. Instead, models with iron atoms incorporated into specific subsurface layers are most stable, in excellent agreement with Auger spectroscopy measurements. Calculations also reveal the magnetic alignment of iron with the manganese nitride layers.

The last study combines iron with gallium in the form of highly magnetostrictive FeGa alloys and investigates their structural and magnetic properties when deposited onto non-magnetic MgO and antiferromagnetic manganese nitride substrates. Films with compositions ranging between ≈ 8 at.% Ga and ≈ 24 at.% Ga are investigated. From X-ray

diffraction measurements it is found that the FeGa films are single crystalline. Scanning tunneling microscopy imaging reveals that the surface morphologies are dictated by the growth temperature, composition, and substrate. The magnetic properties can be tailored by the substrate, as found by magnetic force microscopy imaging and vibrating sample magnetometry measurements. Depositing FeGa onto manganese nitride substrates leads to the formation of stripe-like magnetic domain patterns and to the appearance of perpendicular magnetic anisotropy.

Dedication

To my mother Mirela, my sister Laura, and Sean

– for all of their love and support.

Acknowledgments

I would like to thank my family for never stopping to support me in all the time that we have been away from each other. Their unconditional love made me realize that "it does not matter where you end up in life, what you do, or how much you have, what matters is who you have by your side", as a small inscription that they gave me a few years back says. Many thanks to my mother, whose packages always brought a small piece of home with them. Many thanks to my sister for knowing exactly when to make me laugh so that I stop taking things so seriously. Many thanks also to my grandpa for being proud of me and always emphasizing that hard work and dedication mostly dictate a person's path.

I am very grateful to my advisor Dr. Arthur Smith for his patience, support and useful insights throughout these years, and also for allowing me to be more and more independent, all of which made me want to become a better researcher. I also want to thank him for giving me the opportunity to teach several classes, an experience that was extremely beneficial and that I will always cherish.

I would also like to express my gratitude to my committee members Dr. David Ingram, Dr. Savas Kaya, and Dr. Nancy Sandler for being part of this process and also for their support and encouragement.

I would like to thank Jeremy Dennison and Dr. KangKang Wang for all of their help with the scanning tunneling microscope construction project, and to Dr. Abhijit Chinchore and Dr. Muhammad Haider for helpful tips about lab work. Special thanks go to KangKang for useful discussions about some of my projects. I am also very grateful to Todd Koren, Mike Myers, and Doug Shafer for their help with the lab. Special thanks go to Doug for his promptness and great ideas so that the lab would be up and running in no time. I also want to thank Dr. Steven Goss for allowing us to borrow equipment when needed, and to Dr. Martin Kordesch for coating substrates and for always being willing to help.

I want to also thank my group members Khan Alam, Zakia Alhashem, Perry Corbett, Andrew Foley, and Yingqiao Ma for useful discussions throughout these years. My special thanks go to Perry for his enthusiasm about lab work and also for his help with the atomic force microscopy and X-ray diffraction measurements. I also want to thank Dr. Jeongihm Pak for always being supportive, helpful, and for having a positive outlook on things.

I would also like to thank our collaborators Dr. Kevin Cooper, James Gallagher, Dr. Reyes Garcia-Diaz, Dr. Jonathan Guerrero-Sanchez, Dr. David Ingram, Dr. Jeremy Lucy, Andrea Richard, Dr. Noboru Takeuchi, and Dr. Fengyuan Yang for their promptness and useful insights.

Many thanks also go to Candy Dishong, Julie Goettge, Tim Grubb, Kay Kemerer, Tracy Robson, Don Roth, Chris Sandford, and Meg Van Patten for always being extremely helpful with anything that I needed. My thanks also go to Mayur, Rami, and Sneha for their helpful discussions and support, and also to Dr. Folden Stumpf for fruitful discussions and for always being nice.

I want to thank Filis Oprea, my high school physics teacher, for igniting my interest in physics, and to Dr. Mihai Girtu and Dr. Gabi Petculescu for keeping it going to the point of me considering getting a PhD.

I would also like to thank my good friends Ana, Anda, and Mihai for showing me that distance does not get in the way of friendship, and also to Monica for always making me feel like home is not that far away, but only a short flight to Chicago.

Last but not least I would like to thank Sean for his love, support, and understanding, especially when things got tough. We have been through all this together and I cannot imagine having had anybody else by my side.

Table of Contents

Page

List of Tables

List of Figures

List of Symbols

Roman symbols

a ..... *In-plane* lattice parameter
$\vec{a_1}$,$\vec{a_2}$ ..... Primitive vectors of a 2D direct lattice
$\vec{b_1}$,$\vec{b_2}$ ..... Reciprocal 2D lattice vectors
c ..... *Out-of-plane* lattice parameter
d_{hkl} ..... Inter-planar distance
dI/dV ..... Differential conductance
e_F ..... Fermi energy
$E_{A,B,C}$ ..... Binding energy associated with energy level A, B, or C
E_{ABC} ..... Kinetic energy of transition ABC
H ..... Applied magnetic field
H_a ..... Anisotropy field
H_c ..... Coercive field
H_u ..... Uniaxial magnetic anisotropy
$I_{A,B}$ ..... Peak-to-peak intensity of element A or B
I_r ..... Peak-to-peak intensity of iron (reference)
I_T ..... Tunneling current
$\vec{k}$ ..... Incident wave vector
$\vec{k'}$ ..... Diffracted wave vector
m_s ..... Local magnetization DOS of the sample
m'_s ..... Energy-integrated local magnetization density of states of the sample
m_t ..... Tip magnetization
M_r ..... Remnant magnetization
M_s ..... Saturation magnetization
$\hat{n}$ ..... Unit vector normal to the surface
$\vec{R}$ ..... Arbitrary direct lattice vector
s ..... Tip-sample separation
$S_{A,B}$ ..... Sensitivity factor of element A or B
S_r ..... Sensitivity factor of iron (reference)
T ..... Tunneling matrix
T_S ..... Sample temperature
V_S ..... Sample bias

Greek symbols

λ ..... X-ray wavelength
β ..... Angle between tip and sample magnetization directions
Φ_a ..... Analyzer work function
Φ_{sample} ..... Sample work function

Φ_{tip} . . . . . Tip work function
$\rho_{\downarrow}$ . . . . . Density of spin-down electrons
$\rho_{\uparrow}$ . . . . . Density of spin-up electrons
$\rho_{A,B}$ . . . . . Atomic density of element A or B
ρ_r . . . . . Atomic density of iron (reference)
ρ_s . . . . . Sample density of states
ρ'_s . . . . . Energy-integrated sample local density of states
ρ_t . . . . . Tip density of states
θ . . . . . Angle between incident X-ray and scattering plane

List of Acronyms

AES ..... Auger electron spectroscopy
aFM ..... Antiferromagnetic
AFM ..... Atomic force microscopy
at.% ..... Atomic percentage in a given volume
DFT ..... Density functional theory
DOS ..... Density of states
FFT ..... Fast Fourier transform
FM ..... Ferromagnetic
HV ..... High vacuum
LDOS ..... Local density of states
MBE ..... Molecular beam epitaxy
MFM ..... Magnetic force microscopy
ML ..... Monolayer
MOCVD ..... Metal-organic chemical vapor deposition
MS ..... Magnetostriction
PMA ..... Perpendicular magnetic anisotropy
RBS ..... Rutherford backscattering spectrometry
RHEED ..... Reflection high energy electron diffraction
RT ..... Room temperature
SC ..... Semiconducting
SQUID ..... Superconducting quantum interference device
STM ..... Scanning tunneling microscopy
SP-STM ..... Spin-polarized scanning tunneling microscopy
UHV ..... Ultra high vacuum
VSM ..... Vibrating sample magnetometry
XRD ..... X-ray diffraction

1 INTRODUCTION

Since the discovery of giant magnetoresistance [1, 2] and the reference to "spintronics" [3], the search began to find optimal material systems that are free of rare earth elements and have sharp interfaces between constituent layers. To date, the literature on such studies is overwhelming since an increasing number of systems are being investigated in diverse combinations. Ferromagnetic (FM) materials and their inherent properties are extensively used in today's technology. The ability to change their magnetic behavior, either by coupling them with another magnetic material (such as an antiferromagnet) or by changing their dimensions and/or composition, opened a vast field of research. Real-world applications rely on information extracted from macroscopic characteristics of ferromagnets, such as hysteresis, and extend all the way down to atomic scale magnetism where the study of surfaces and interfaces becomes essential.

The main focus of my studies was to explore the behavior of FM manganese gallium and iron gallium alloys in different spintronic and magnetic nitride systems, starting with atomic scale studies and expanding to macroscopic measurements. Both MnGa and FeGa have their Curie points well above room temperature and can have their properties tuned by varying their composition. The amount of surface data available for these alloys is very limited, thus providing a unique opportunity for the present studies. Manganese gallium is a Heusler-type alloy, meaning that even if none of its constituent atoms is FM, their alloy is. The Mn-rich regime (i.e. Mn:Ga composition ratios greater than 1) of MnGa films has been studied to a great extent, finding that its magnetic properties can be changed easily by substrate choice. We have focused on the less studied stoichiometric (Mn:Ga=1) and Ga-rich (Mn:Ga less than 1) sides of this alloy when deposited onto semiconducting GaN(0001) and looked in detail at the structural and magnetic properties. Iron gallium possesses magnetostrictive properties, i.e. it can change shape if its magnetization state is altered; the reverse is also true and by inducing a strain in the FeGa structure its magnetic

properties could be changed, making this system of high interest for the sensor and actuator industry. Since FeGa has been mainly studied in single-crystal form grown by bulk methods, the focus or our studies was on thin FeGa films when in contact with antiferromagnetic (aFM) and non-magnetic substrates. We have explored how this material system grows and also how its magnetic properties change with substrate choice. By also studying only Fe depositions onto the same aFM manganese nitride surfaces we have explored interface effects that could have a direct impact on the magnetic properties of FeGa over-layers. All studies utilized a number of techniques that are aimed at answering different questions about the investigated systems, and therefore complement each other when used simultaneously. The unexpected results obtained for some of these systems reveal the complexities associated with their properties.

The ability to grow the desired materials under controlled conditions is of high importance. One of the primary techniques used in my work is molecular beam epitaxy (MBE), which allows one to deposit one atomic layer at a time with precise control. The resulting films have atomically smooth and very clean surfaces, making them suitable for subsequent *in-situ* surface studies. Scanning tunneling microscopy (STM), another main technique used in my studies, allows us to map out the atomic structure of surfaces while also providing electronic and magnetic information down to atomic level. Since the properties of surfaces are often reflected by their composition, we also used *in-situ* Auger electron spectroscopy (AES) to determine surface elemental composition ratios.

Depending upon the nature of each study, further investigations were sometimes necessary. For example, *ex-situ* atomic force microscopy (AFM) and magnetic force microscopy (MFM) were used for characterizing large scale morphology and magnetic domain structure, respectively; X-ray diffraction (XRD) was also used for determining growth orientations and crystal quality. Additional investigations were possible due to collaborations with other groups, which helped tremendously in revealing key aspects

about my studies. For the two projects presented in Chapters 3 and 5, first-principles density functional theory (DFT) calculations accompanied our experimental findings. Due to an ongoing collaboration with Prof. Noboru Takeuchi's group at Universidad Nacional Autónoma de México, two students visited Ohio University for one year each and carried out theoretical calculations. In collaboration with Prof. David Ingram's group at Ohio University, we used Rutherford backscattering spectrometry (RBS) to determine bulk compositions. Another collaboration with Prof. Fengyuan Yang's group at The Ohio State University involved using vibrating sample magnetometry (VSM) and superconducting quantum interference device (SQUID) magnetometry to determine the bulk magnetic properties of some of our films. Chapter 2 describes the principles behind some of the aforementioned techniques.

Wide-gap SC GaN is well known for its use in electronic and optoelectronic devices, and is therefore a great candidate for coupling with magnetic atoms. As mentioned above, MnGa can have its properties tailored for a particular application depending upon its composition and/or underlying substrate. For a Mn:Ga ratio close to stoichiometric, MnGa grows under ideal epitaxial conditions and with sharp interfaces when deposited onto GaN(0001), while also exhibiting large magnetic moment values.[4] We therefore investigated in detail the surface structure of MnGa ultra-thin films grown under slightly Mn-rich conditions onto GaN(0001) substrates, using a combination of STM/AES and bulk composition measurements. Theory calculations were also carried out in order to probe the most stable surface structures; all calculations were performed by Reyes Garcia-Diaz, visiting student at Ohio University between 2011 and 2012. We obtained very good agreement between theory and experiment, finding that slightly Mn-rich growth conditions lead to very Mn-rich surfaces while the bulk remains stoichiometric. These results highlight the important relationship between surface and bulk and reveal that the properties of MnGa

are very sensitive to the elemental ratios in its structure. These results are the subject of Chapter 3.

Results from the previous study called for a better understanding of what changes could occur if the Ga concentration in the MnGa structure is altered. The main questions that this study attempted to answer refer to how the structure and magnetism of MnGa films are affected by compositional changes and also by film thickness. Chapter 4 describes the study of varying-thickness MnGa films deposited onto GaN(0001) substrates, with an emphasis on the less-studied Ga-rich regime. Due to the unknown structure, composition and magnetic properties, we combined the usual MBE/STM/AES studies with *ex-situ* structural and magnetic characterizations. From STM imaging we observe a very interesting array of surface structures that are thickness-dependent. In terms of magnetism, we find that even under very Ga-rich conditions the system remains FM, and that giant perpendicular magnetic anisotropy (PMA) is induced by reducing the film thickness to several nanometers.

Chapter 5 presents the study of Fe, the most popular ferromagnet, in contact with the antiferromagnet manganese nitride. Briefly, manganese nitride is a very rich system, with most of its phases being aFM; however, due to the different growth orientations and structure, the antiferromagnetism in this material manifests at the surface as alternating rows or alternating terraces. We chose the surface of $Mn_3N_2(001)$ (also known as the $\eta_\perp$ phase), which shows orthogonal terrace-dependent spin orientations [5], as the starting substrate for sub-monolayer (sub-ML) Fe depositions. We then combined STM and AES experiments with theory calculations to study the initial stages of interface formation between these two materials. The theoretical calculations were performed by Jonathan Guerrero-Sanchez, a visiting student between 2013 and 2014. The results were quite unexpected, revealing that this system forms alloyed interfaces while still preserving magnetic order.

We have also extended the study of only Fe depositions onto aFM substrates to combine Fe with Ga, and these investigations constitute the subject of Chapter 6. The magnetostriction

(MS) value in this system is highly dependent on the Ga concentration present in the structure and it exhibits a first peak at about 19 at.% Ga.[112] In addition, the amount of strain within the FeGa lattice dictates the resulting magnetic properties. Therefore, we deposited this material onto aFM Mn_3N_2(001) and MnN(001) substrates, as well as onto insulating MgO(001) substrates, keeping the composition around 19 at.% Ga. Similar to the study of Ga-rich MnGa/GaN system, we combined surface studies with structural and magnetic measurements to reveal how the magnetic properties and magnetic domain structure change with composition and substrate choice.

The above studies attempted to reveal and explain some of the properties of technologically important ferromagnets when coupled with non-magnetic and magnetic substrates. A summary of all results is given in Chapter 7. In my opinion, these studies also open the way to new and exciting explorations, some of which are mentioned at the end of each chapter. In addition to the studies mentioned above, my work also focused on building a back-up STM body; details about the construction are given in Appendix A. Appendix B elaborates on the calibrations of our AES system that are required to obtain better estimates of surface elemental composition ratios. Finally, Appendices C and D include a list of publications (as first- and co-author) and a list of first-author contributed oral/poster presentations, respectively.

2 TECHNIQUES

The first three sections of this chapter describe the main techniques used in my work: molecular beam epitaxy, scanning tunneling microscopy, and Auger electron spectroscopy. All of these techniques are used *in-situ* under UHV conditions. First, details about the principles of each technique are given, followed by a description of the system in which all experiments were performed. In the subsequent sections, brief details about the principles behind each of the additional *ex-situ* techniques used are presented, including the specifics of each experiment applied to our samples.

2.1 Molecular beam epitaxy

MBE represents a thin film deposition technique, which uses as basic process the interaction of high-purity atomic beams with the surface of a heated substrate. This process takes place in UHV (pressures $\leqslant 10^{-10}$ Torr), which is essential for obtaining high quality epitaxial films since the number of residual atoms impinging on the sample's surface is very small and the atomic beams travel in almost collision-free paths (the mean free paths are typically a few orders of magnitude higher than the beam source-sample separation). In the absence of UHV, the surfaces of the investigated materials become very complex and therefore difficult to study. A huge advantage of the MBE method is that one has good control over sample composition down to monolayer (ML) level. Since its development, high quality semiconductors, oxides, and metal alloys have been successfully grown; multilayer doping, a whole new field of material tailoring, was also made possible.[7–11]

The inside of an MBE chamber is schematically shown in Fig. 2.1. The elements from which the atomic beams are released rest inside a crucible (typically made of pyrolytic boron nitride) mounted inside an effusion cell. The crucible is surrounded by a filament which provides a temperature that is elevated enough to give high intensity beams. The on/off status of the atomic beam is controlled mechanically by a shutter which can be opened/closed from

outside the chamber. Elemental fluxes are typically determined using a quartz crystal sensor; as material accumulates on the sensor, its frequency changes and this change is converted into a thickness, which can then be used to calculate a flux value. The MBE chamber is also equipped with a reflection high energy electron diffraction (RHEED) system, which allows one to obtain structural information about the surface of a given solid, and also monitor the growth process in real-time. The principle behind RHEED will be described in more detail in the next section.

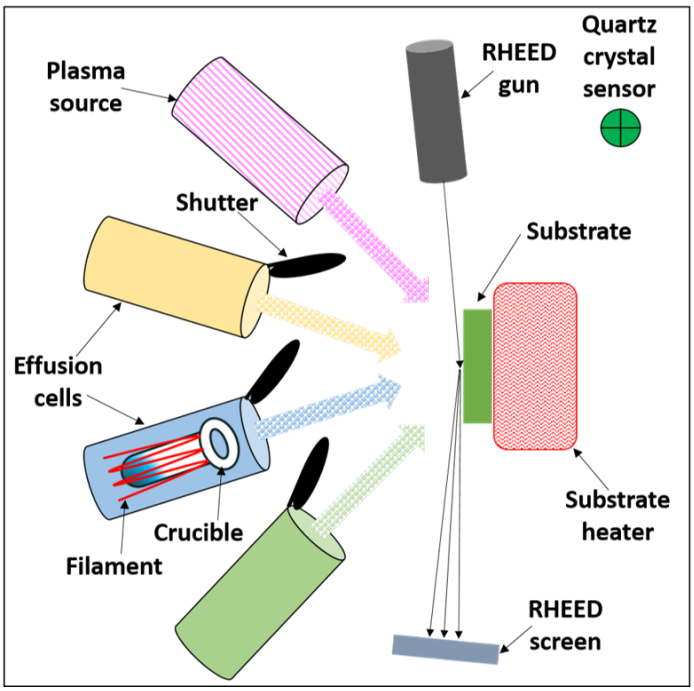

Figure 2.1: Schematics of some of the typical components found inside an MBE chamber: substrate holder and heater, effusion cells (to provide elemental atomic beams), RHEED system (for growth monitoring), quartz crystal sensor (for elemental calibration). For nitride growth, the MBE chamber can also be equipped with a nitrogen plasma source.

Since MBE depositions involve the use of a starting substrate, the quality and morphology of the resulting film depends on its lattice match with the substrate, and also on the growth temperature, atomic fluxes, and growth rate. The deposition process can

be *homoepitaxial* if the film and substrate are of the same material, or *heteroepitaxial* if the materials are different. Depending on the material and deposition conditions, three growth modes are typically observed: i) layer-by-layer (or Franck-van der Merwe) in which a new layer starts only after the previous one is completed; ii) islands only (or Vollmer-Weber) in which atom diffusion is not allowed past the island boundary; and iii) islands plus layer (or Stranski-Krastanov), an intermediate growth mode, in which island formation takes place on top of completed layers beyond a certain critical thickness.

2.1.1 Reflection high energy electron diffraction

In RHEED, a high energy ($\approx$ 20 keV) electron beam is sent at grazing incidence ($\approx 1°$) with respect to a sample's surface and the diffraction pattern resulting from their interaction is projected onto a phosphor-coated screen. The RHEED pattern provides useful information about atomic distances and associated surface structures, and also about sample quality during growth.[12, 13]

The surface of a crystalline solid can be considered as a 2D diffraction grating, defined by the reciprocal lattice vectors $\vec{b_1}$ and $\vec{b_2}$, given by [13]:

$$\vec{b_1} = 2\pi \frac{\vec{a_2} \times \hat{n}}{\vec{a_1} \cdot (\vec{a_2} \times \hat{n})} \tag{2.1}$$

and

$$\vec{b_2} = 2\pi \frac{\hat{n} \times \vec{a_1}}{\vec{a_1} \cdot (\vec{a_2} \times \hat{n})} \ , \tag{2.2}$$

where $\vec{a_1}$ and $\vec{a_2}$ are the primitive vectors of the direct lattice; $\hat{n}$ is the unit vector normal to the lattice plane.

The von Laue diffraction condition is satisfied when [14]:

$$(\vec{k} - \vec{k'}) \cdot \vec{R} = m2\pi \ , \tag{2.3}$$

where $\vec{k}$ and $\vec{k'}$ are the wave vectors of the incident and diffracted electron beams, respectively; $\vec{R}$ is an arbitrary direct lattice vector ($\vec{R}$=$n_1\vec{a_1}$+$n_2\vec{a_2}$, with n_1 and n_2 integers)

and m is an integer. In order to locate the directions of the diffracted beam, the Ewald sphere construction is used [14]; the sphere is constructed from the origin of $\vec{k}$ at the physical point on the sample's surface. The reciprocal space points can be extended normal to the surface (becoming rods) and their intersection with the Ewald sphere constitute diffraction maxima.

Figure 2.2(a) shows a 3D schematic representation of the Ewald construction. One can observe that the resulting diffraction pattern consists of sharp spots on the RHEED screen. This represents an idealized situation in which: i) the incident electron beam is considered mono-energetic and infinitely thin, and ii) the reciprocal rods are considered infinitely thin. However, in a real experiment one is dealing with instrumental broadening (given by the fact that an electron beam has a certain width and also some divergence) and/or sample broadening (which would give some finite thickness to the reciprocal rods); these facts combine to change the RHEED pattern into streaks rather that spots.[12]

Figure 2.2(b) shows a top-view of the schematics from 2.2(a), with more reciprocal rods included. At the intersection points, the Miller indices (hk) of the reciprocal lattice points are indicated. It is evident that the locations of the reciprocal rods determine the arrangement of diffraction streaks on the screen. By measuring the RHEED streak spacing, and by using Eqs. 2.1 and 2.2 above one can work backwards and obtain the lattice parameters(s) of the real space lattice of a crystalline solid, which correspond to particular crystallographic orientation(s). Furthermore, depending on the relative RHEED streak orientations between the starting substrate and overgrown film, one can determine their epitaxial relationships.

2.2 Scanning tunneling microscopy

Since its discovery in 1982 [15, 16], STM has been an invaluable tool for investigating the structure and properties of surfaces. It has been successfully used in the study of both metals and semiconductors, providing unprecedented information about surface quality, morphology, and atomic arrangements.[17, 18] Since the early 1990's, STM has been

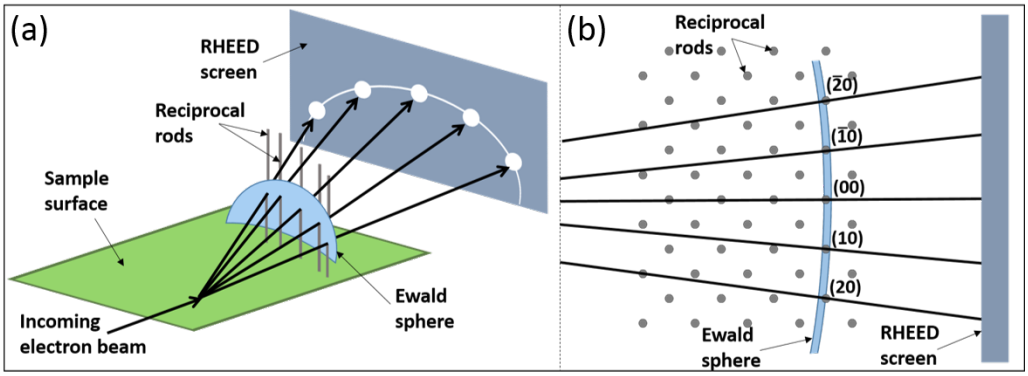

Figure 2.2: Schematics of RHEED principle; 3D (a) and top (b) views of the intersection of reciprocal lattice rods with the Ewald sphere, and the formation of RHEED patterns onto the screen.

increasingly used in determining the magnetic properties of various FM and aFM surfaces, culminating with the study of single-atom magnetism.[19–23] Such impressive results are accomplished by operating the STM in UHV and at temperatures that can range from only a few Kelvin and up RT or even higher.

During STM operation, a sharp metallic tip and a metallic (or SC) sample are brought in close proximity (a few Å) to one another. Upon applying a voltage V to the tip-sample junction, a small tunneling current I_T (in the nA regime) will flow from the tip into the sample or vice versa (depending upon the bias polarity), as shown in Fig. 2.3(a). The tip, typically made of tungsten and mounted onto a piezoelectric scanner, is first brought close to the sample (few μm) using a coarse approach mechanism; subsequently, the tip is brought and maintained into tunneling range by control electronics.

One way of operating the STM is under constant height mode, in which the tip is positioned at a fixed distance above the sample and the tunneling current is recorded as the tip scans the surface. However, the most common mode of operation is under constant current, where the tunneling current is set to a fixed value and the changes in height are recorded. This is done by using a feedback loop control, which adjusts the tip height in

order to keep the tunneling current constant; as the tip rasters across the surface, a z(x,y) map is recorded and converted into a topographical image.

For the case of a non-magnetic tip and/or sample (i.e. spin-averaged STM), if there is no bias applied [middle panel in Fig. 2.3(a)], then the Fermi levels of the tip and sample are aligned and no tunneling takes place. Once a negative bias is applied to the sample, the Fermi level of the sample is raised by e|V| and the electrons can tunnel from the filled states of the sample into the empty states of the tip [left panel in Fig. 2.3(a)]. In the reverse scenario, for the case of positive bias, the sample Fermi level is lowered by e|V| and the electrons are free to tunnel into the empty states of the sample [right panel in Fig. 2.3(a)].

In addition to surface topography, the tunneling current allows one to extract further information about the sample properties. A common way of treating I_T is to generalize the Tersoff-Hamman approximation [24], which considers very low applied voltages and s-like tip states. The generalization involves restricting the contribution of the tunneling current to tip and sample states that are available within a finite energy window; the expression for the tunneling current is [17]:

$$I_T(V) \propto \int_0^{eV} \rho_s(e_F + E)\rho_t(e_F - eV + E)T(s, V, E)dE \ , \tag{2.4}$$

where ρ_s and ρ_t are the sample and tip density of states (DOS), respectively; $T(s, V, E)$ is the tunneling matrix element (or transmission coeficient) that depends on the applied bias and work functions of the tip and sample (Φ_{tip} and Φ_{sample}), and that also contains a term which gives the exponential dependence on the tip-sample distance s; this exponential dependence is what ultimately allows the STM to achieve single-atom resolution. In general, the tip DOS and the tunneling matrix T are considered constant in Eq. 2.4 and the tunneling current is therefore a measure of the sample DOS within the considered energy window.

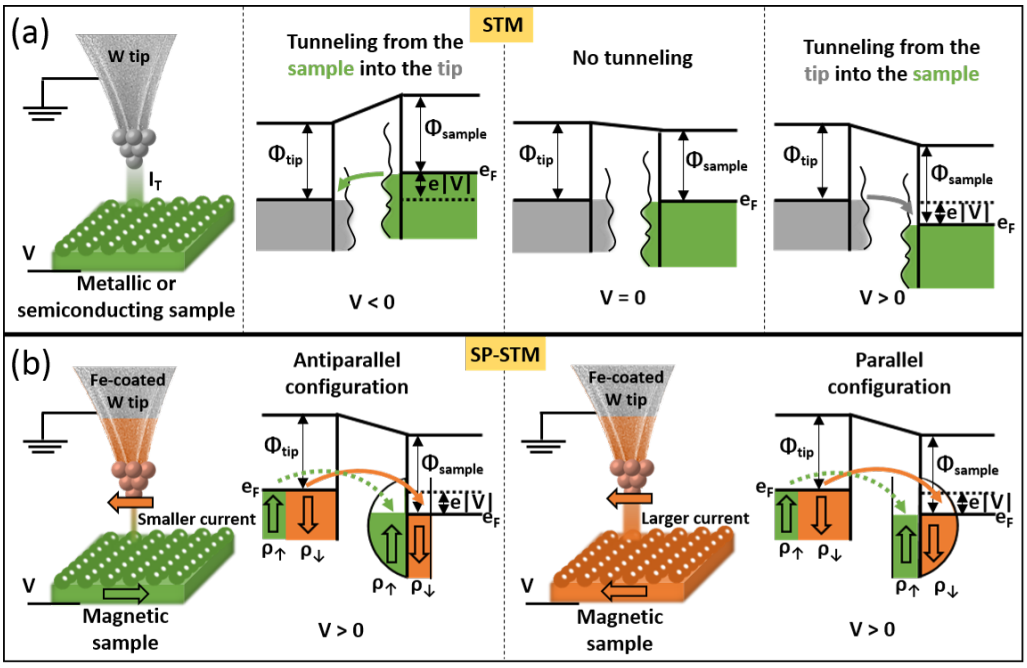

Figure 2.3: (a) Schematic representation of the tunneling process between the tip and the sample in STM. (b) A similar representation, but this time considering the spin polarization of the tip and sample electrons, for cases in which the tip and sample magnetization vectors are aligned antiparallel and parallel, and for a positive bias applied to the sample.

2.2.1 Scanning tunneling spectroscopy and dI/dV mapping

As seen in the previous section, the tunneling current is dependent on the applied bias V and also on the tip-sample separation s. By keeping s constant, one can sweep the voltage over a particular range while recording the current, thus obtaining an I-V curve. This technique is known as scanning tunneling spectroscopy (STS) and it provides excellent information about the electronic (and magnetic, as discussed below) properties of localized regions of the surface. From an I-V curve, by taking the derivative of the current (from Eq. 2.4) with respect to the applied bias, one can obtain an expression for the differential conductance dI/dV, a measure of the local DOS (LDOS) of the surface at an energy value eV:

$$dI/dV \propto \rho_s(e_F + eV)\rho_t(e_F)T(s, V, eV) \ , \tag{2.5}$$

from where is evident that the differential conductance is directly proportional to the sample LDOS $\rho_s(e_F+\text{eV})$, but it is also dependent on the tip-sample separation and applied bias. As a note, when taking the derivative of the current given by Eq. 2.4, two additional terms containing integrals appear; they were omitted in the above equation as they vanish when considering constant tip DOS and constant tunneling matrix.

If one is interested in mapping the electronic properties of a larger area of a given sample, multiple dI/dV spectra can be acquired using a lock-in technique; it involves using a lock-in amplifier to add a small modulation to the bias voltage and recording changes in I_T (that are sensitive to the slope of the I-V curve) at every pixel. Thus, one can combine all the electronic information of a portion of a sample in a single dI/dV map, which is presented in the form of an image.

2.2.2 Spin-polarized scanning tunneling microscopy

One way of obtaining magnetic information about a particular sample surface is by coating a non-magnetic tip with a magnetic material (i.e. Fe, Mn, etc.), and performing spin-polarized STM (SP-STM). This technique is based on the tunneling magnetoresistive effect, in which the current between two magnetic electrodes is dependent on the angle between their magnetization directions: for parallel magnetization directions a larger current will flow between the two, whereas a smaller current will be detected if they are antiparallel, as shown in Fig. 2.3(b). From the same figure it can be observed that now the tip and sample are split into minority and majority DOS (labeled as $\rho_\downarrow$ or $\rho_\uparrow$, depending upon the net magnetization direction of the tip or sample).

The expression for the tunneling current given below considers that the electron spin is conserved during tunneling, meaning that spin-$\downarrow$ electrons can only tunnel into spin-$\downarrow$ states and vice versa [23, 25]:

$$I_T(V) \propto \rho'_s\rho_t + m'_s m_t \cos\beta \ , \tag{2.6}$$

where ρ'_s is the energy-integrated sample LDOS, ρ_t is the non-spin-polarized LDOS of the tip apex, m'_s is the energy-integrated local magnetization DOS of the sample (given by an energy integral of the local magnetization DOS m_s of the sample), m_t is the tip magnetization ($m_t=\rho_\downarrow-\rho_\uparrow$), and β is the angle between the magnetization directions of the sample and tip. The first term ($\rho'_s\rho_t$) gives the spin averaged contribution to the current, whereas ($m'_s m_t \cos\beta$) contains the spin-polarized part; the latter is typically zero for a non-magnetic tip and/or a non-magnetic sample (described in the previous section).

By taking the first derivative of the spin-polarized current, the differential conductance can be obtained, and it is given by:

$$dI/dV \propto \rho_s(e_F + eV)\rho_t + m_s(e_F + eV)m_t \cos\beta \ . \tag{2.7}$$

Similar to the spin-averaged case described in the previous section, a spin-polarized dI/dV map can be recorded at every pixel, thus providing information about the magnetic properties of a sample region.

2.3 Auger electron spectroscopy

Since material properties often depend on the state of their surfaces and/or interfaces, having chemical information about the atomic species within a given surface is crucial. AES is a surface sensitive technique widely used to determine elemental compositions by utilizing the emission of characteristic Auger electrons. Due to the short mean free path of electrons in a solid, AES is able to only probe several atomic layers beneath the surface.[26, 27] As described below, the Auger process is a three-electron process (or four-electron, if the incident electron beam is considered). Therefore, all elements emit Auger electrons, with the exception of hydrogen and helium, and based on the measured Auger energies one can identify specific elements.

The Auger process for a KLL transition is schematically shown in Fig. 2.4 and takes place as follows. An incoming electron beam (with typical energy between 3 keV and 10

keV) ejects a core level (K) electron, leaving behind a hole. The hole is filled by an outer shell (L_1) electron. The excess energy (E_K-E_{L_1}) is then transferred to an electron from a more shallow shell ($L_{2,3}$), which is the emitted Auger electron.

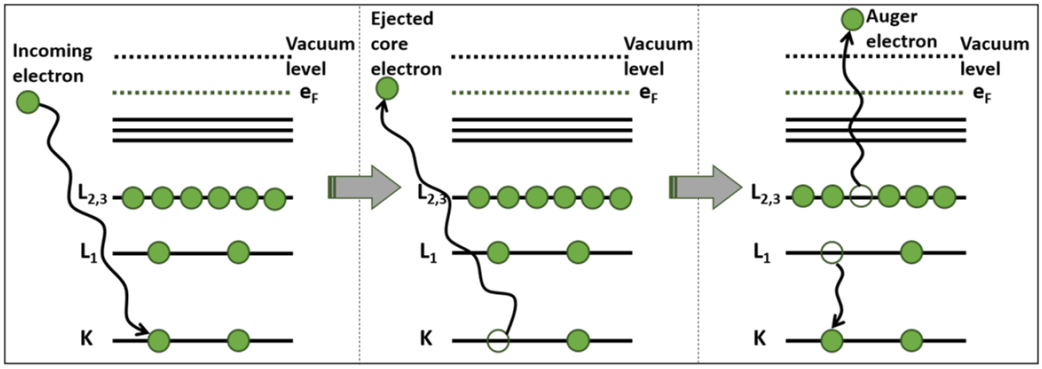

Figure 2.4: Schematic representation of the Auger process.

In general, an Auger transition is denoted as ABC, where A is the level from which the first electron is removed, B is the level from which the second electron originates, and C is the level from which the third electron (Auger electron) is emitted. The kinetic energy of an Auger transition ABC is then given by:

$$E_{ABC} = E_A - E_B - E_C - \Phi_a \ , \tag{2.8}$$

where E_A, E_B, and E_C are the binding energies associated with energy levels A, B, and C, respectively; Φ_a represents the work function of the spectrometer.

An AES spectrum plots the number of electrons N(E) being detected as a function of their kinetic energy E. Typically, the spectrum is displayed in derivative mode [dN(E)/dE versus E] to remove the large background given by secondary electrons that are emitted as a results of electron beam-sample interactions. In the Auger plot, the peak positions determine what elements are present within the surface (qualitative information), and the peak intensities are related to the concentrations of those particular elements (quantitative

information).[28, 29] One way of obtaining quantitative measures of (relative) atomic concentrations in a given sample is by measuring peak-to-peak intensities from derivative spectra and using sensitivity factors for specific transitions. However, since the measured Auger intensities are dependent on quantities that are intrinsic to the type of AES system used [26], the sensitivity to a specific element has to be determined for that particular system.

2.4 System description in lab 151

Figure 2.5 shows an image of the MBE/AES/STM system in Clippinger 151. The system consists of two interconnected UHV chambers, separated by a metal gate valve. The MBE growth chamber (to the right of the gate valve in Fig. 2.5) is pumped by a cryogenic pump, whereas the STM/AES analysis chamber (to the left of the gate valve in Fig. 2.5) is pumped by an ion pump. Base pressures for both chambers are $\approx 10^{-11}$ Torr. Not visible in the image is a high vacuum (HV) load-lock chamber, pumped by a combination of rotary and turbo pumps, and used to load/un-load substrates, tips, and small magnets. Ionization gauges are used for pressure readings in all chambers. In case of equipment malfunctions, the chamber(s) can be brought to atmospheric pressure via the load-lock chamber. Following repairs, they can be pumped back to HV values ($\approx 10^{-8}$ Torr). However, in order to achieve UHV pressures a thorough bake-out needs to be performed, by heating the various parts of the system typically between $\approx 65^{\circ}$C and $\approx 110^{\circ}$C (depending upon the component). The bake-out procedure takes place by wrapping the chamber(s) with a layer of aluminum foil, followed by placing heating tapes at specific locations, and finally by wrapping everything with another layer of aluminum foil (see, e.g., the analysis chamber in Fig. 2.5).

Starting with the growth chamber, it is equipped with a growth stage, four home-built effusion cells (containing Mn, Ga, Fe and Cr elemental sources) and a radio-frequency nitrogen plasma source. The exterior parts of the effusion cells and plasma source are water-cooled. Other capabilities include a STAIB Instruments RHEED system (20 keV

electron gun, fluorescent screen, and CCD camera), and also a quartz crystal sensor (mounted opposite to the effusion cells).

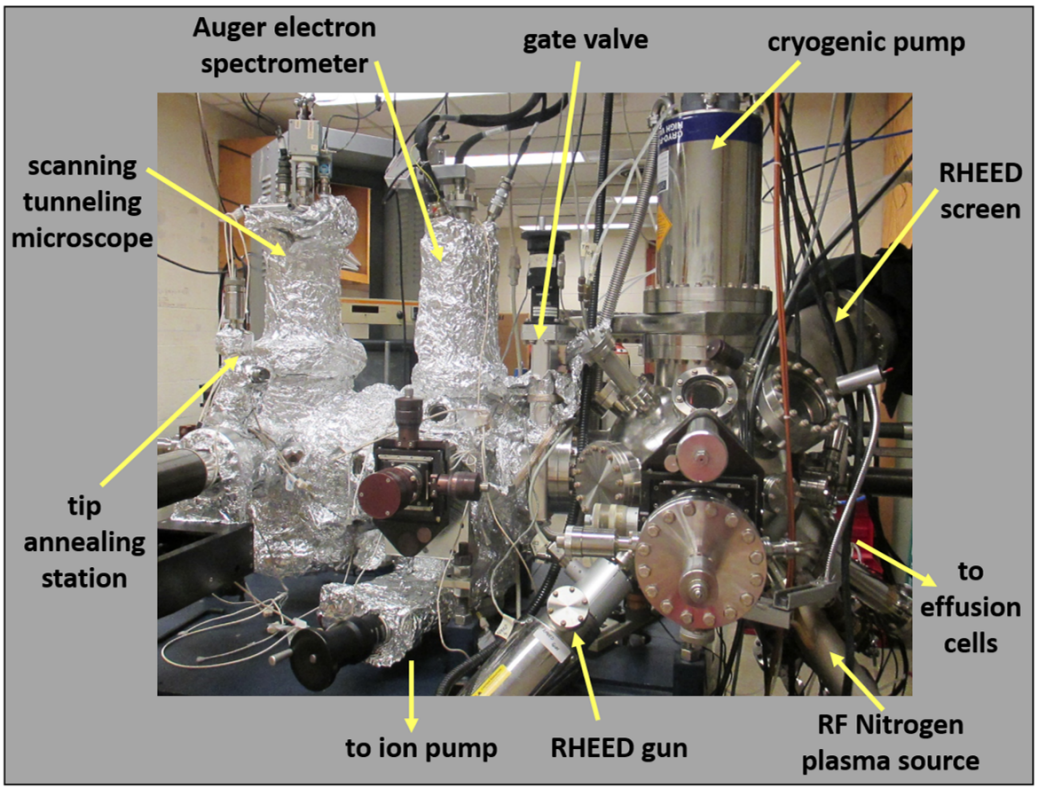

Figure 2.5: Image of the UHV MBE/AES/STM system in which the experiments were performed, with some of the main components labeled.

A typical sample preparation takes place as follows. First, the substrate (1 cm × 1 cm in size) is cleaned *ex-situ* in solvents (acetone and isopropanol) and introduced into the MBE chamber via the load-lock and analysis chambers. Once mounted onto the growth stage, the substrate is annealed at high temperature (typically between 650°C and 1000°C depending upon the substrate type) and under nitrogen plasma (depending upon the type of sample that needs to be obtained). Following annealing, the substrate temperature is set to the desired value and the growth begins by opening the mechanical shutter(s) of the effusion

cell(s). Depending upon the RHEED pattern, elemental source fluxes and/or temperature of the sample can be adjusted until the desired sample quality is achieved. During nitride growth (e.g. GaN or MnN), the pressure in the growth chamber is kept at 2.0×10^{-5} Torr. This pressure value corresponds to a particular flux of N atoms, determined by growing a GaN sample on the border between N-rich and Ga-rich conditions. The Ga temperature is adjusted during growth until a streaky 1×1 RHEED pattern is obtained; thus, we consider the N flux to be approximately equal to the Ga flux at that particular temperature.

Specifics about the preparation of each sample used in my studies are given in the corresponding chapter under "Methods". Once a sample is prepared, it is transferred *in-situ* inside the adjacent analysis chamber (described below) for STM studies, followed typically by AES analysis.

The analysis chamber hosts a home-built room temperature (RT)-STM, developed by Wang *et al.* [30] During scanning, the whole system is isolated from floor vibrations using four laminar-flow air legs; in addition, a double-stage spring suspension system is used to isolate the STM core from the analysis chamber. As part of my dissertation work, I have built a new STM body that can be used in both vertical and horizontal orientations, and that can also be integrated in a variable temperature system. Appendix A describes some details about this work. For scanning, tips made out of tungsten wire ($0.02''$ in diameter) are used. They are prepared using electrochemical etching, in 2M NaOH solution (8 g of NaOH pellets per 100 ml of distilled water) and with an applied AC voltage of ≈ 4.2 V. More recently, a new method of tip preparation was developed in our lab, and it involves a slightly modified set-up and the use of acetone vapor during etching; this method allows us to have better control over the dimensions of the tip apex.[31] Once introduced into the analysis chamber, the tips are annealed using electron bombardment in order to remove the oxide layers present due to previous air exposure. Following annealing, the tips can be coated with a magnetic material (such as Fe or Mn) for SP-STM experiments. Our sample transfer

system also allows for magnetic fields (of about 0.4 T) to be brought in close proximity to the sample (a few mm away) during SP-STM experiments. As a note, the STM images for all of my studies were acquired under constant current mode and image processing was done using mainly the WSxM software.[32]

The analysis chamber is also equipped with a 5 keV STAIB Instruments AES system. Since Auger results are often correlated with RHEED and STM observations, one has to make sure that the extracted surface composition is as accurate as possible. Whereas AES is excellent at providing qualitative information about the surface chemistry of various samples, obtaining quantitative information can be rather difficult and often not accurate, due to the inability to compute reliable sensitivity factors. Although sensitivity factors for almost all known elements are well tabulated [26], they can change depending upon the type of analyzer used in the respective AES system. In order to determine such sensitivity factors, one has to investigate control samples with known composition; in addition, a careful analysis of the obtained spectra needs to be performed. Appendix B details how the sensitivity factors for Fe, Ga, Mn, and N were determined for our specific analyzer.

The composition of element A relative to that of element B in a binary sample (after computing their corresponding sensitivity factors S_A and S_B) is determined using [26]:

$$\frac{A}{B} = \frac{I_A/S_A}{I_B/S_B} \ , \tag{2.9}$$

where I_A and I_B are the measured peak-to-peak intensities for specific transitions of elements A and B, respectively.

2.5 Additional techniques

2.5.1 Atomic and magnetic force microscopy

The AFM technique is similar to STM in many respects, except for the tip, which is replaced by a force-sensing cantilever with a small tip mounted at one end.[33] AFM relies

on the interaction between this probe tip and sample to form a topographic image of the surface. The AFM tip is kept close to the surface by a feedback mechanism (just as in the case of STM) and as it scans, the deflections of the cantilever due to forces acting on the tip are recorded. Whereas STM is limited to imaging SC and conducting samples in UHV [except for highly oriented pyrolytic graphite, which can be easily imaged in air], AFM can also image insulating samples and in ambient conditions, thus eliminating the need for vacuum sample preparation.

AFM typically operates in two modes: 1) static (or contact), where the tip is very close to the surface and repulsive forces are measured by recording the cantilever deflections; and 2) dynamic (or non-contact), in which the cantilever is intentionally vibrated close to its resonance frequency and the changes in phase and/or amplitude due to the attractive forces between tip and sample are recorded. Although the static mode can provide high resolution, damage to both sample and tip can occur due to their close proximity (especially if the sample is soft or exhibits pronounced surface roughness). As a result, the dynamic operating mode is normally used since it works for a variety of samples without much loss of resolution.

The use of AFM has been extended to measure other sample properties. By using a similar probe tip, but coated with a magnetic material (such as Co), one can sense the magnetic stray field distribution of a magnetic sample, by observing changes in the cantilever deflection. During MFM image acquisition (known as lift mode) two scans for each line of the image are performed: one follows the topography of the surface (with the tip being closer to the surface); the other takes place at a fixed height (set by the user) above the surface, and records the magnetic signal. Thus the magnetic and topographic information can be separately, but simultaneously recorded.[34–37]

All measurements were performed in our laboratory using a modified Park Scientific Instruments AFM/MFM operated in dynamic mode. The AFM measurements for Chapter

4 were conducted by Joseph Corbett. Commercial tips made of SiN were used for AFM scans, whereas Cr/Co/SiN tips were used for MFM imaging. WSxM software was used for AFM/MFM image processing.[32] For the results of Chapter 6, Fast Fourier Transforms (FFTs) of the MFM images were performed using Gwyddion software.

2.5.2 X-ray diffraction

By looking at the manner in which atoms within a crystalline material scatter X-rays, one can obtain information about the atomic arrangement within that particular material. Each crystalline solid has a specific structure, causing the X-rays to diffract in different directions. Whenever constructive interference occurs, Bragg's diffraction condition, which relates the wavelength λ of the incoming X-rays to the path difference ($2d \sin\theta$) between two X-rays reflected from adjacent crystal planes, is satisfied [14]:

$$n\lambda = 2d \sin\theta \ . \tag{2.10}$$

Here n is an integer, d is the inter-planar distance, and θ is the angle between the incident X-ray beam and the scattering plane within the solid.

A typical diffractometer consists of an X-ray source, a goniometer, a sample holder, and a detector. The X-rays are produced by the interaction of an electron beam with a target material, such as Cu or Mo. The resulting X-rays have a wavelength that is comparable to the inter-atomic distances within a solid. An XRD spectrum plots X-ray intensity versus 2θ since for typical scan geometries the sample moves by θ and the detector moves by 2θ (for this reason the XRD scan is sometimes called a θ-2θ scan).

Equation 2.10 allows one to determine the inter-planar distance d (since λ is known), from which the *in-plane* (a) and *out-of-plane* (c) lattice constant could be calculated. For epitaxial films deposited on a substrate, XRD therefore provides valuable growth orientation information. The diffraction pattern also contains rich information about the crystallinity of the material (dependent on the intensity of the diffraction peaks) and also about strain

present in the lattice (which can manifest as asymmetry, broadening and/or shifting of the diffraction peaks).

The XRD measurements for my studies were performed at Ohio University using a Rigaku MiniFlex II diffractometer with a Cu Kα radiation source (λ = 1.541 Å) and located in Clippinger 353. The XRD measurements for Chapter 4 were conducted by Joseph Corbett. The scans typically covered 2θ angles between 5° and 110°. Measurements were performed for most studies, whether to obtain the orientation and lattice parameters of unknown films, or to make sure that the expected sample was obtained; the latter is of high importance since for some materials even a slight imbalance in the flux during growth can have significant effects on the resulting film orientation. Scans of the starting substrates (e.g. MgO and GaN) were performed in order to locate the expected peak positions before overgrowing a new material.

2.5.3 Rutherford backscattering spectrometry

RBS is a common technique used to determine the composition of layered solids.[38] The typical instrument set-up for RBS consists of an ion source (e.g. α particles), a particle accelerator (up to several MeV), and a detector. During a measurement, the high-energy beam is directed toward the specimen, and the backscattered energy distribution from collision with sample nuclei is recorded. Since the nuclei of different atoms will scatter the incident ions differently, there will be distinct signals in the resulting plot. By comparing scattering signals with known cross sections, the composition of a given sample can be determined, thus eliminating the need for calibration samples. Relative concentrations of elements can also be determined by measuring signal intensities.

All RBS measurements for my studies were carried out at Ohio University using a 4.5-MV Tandem accelerator with 2.200-MeV and 3.035-MeV α beams, located in Edwards Accelerator Laboratory. The measurements and data analysis were conducted by Kevin

Cooper (for the results of Chapter 3) and by Andrea Richard (for the results of Chapters 4 and 6). During measurements, the samples were typically oriented at $\approx 75^{\circ}$ with respect to the incident beam in order to get better depth profiles of the regions of interest. Following acquisition, the spectra were modeled using the Genplot/RUMP software. Typical errors in elemental concentrations are around 10%, and they mainly come from difficulties in the modelling associated with sample roughness and/or peak shape.

2.5.4 Vibrating sample magnetometry and superconducting quantum interference device magnetometry

Some of the most useful information about the properties of a magnetic material can be extracted by measuring its hysteresis loop. The most commonly used techniques for obtaining magnetic information are VSM and SQUID magnetometry. During VSM measurements, the sample is mechanically vibrated while placed in an uniform magnetic field (generated typically by an electromagnet); pick-up coils are mounted onto the electromagnet and the change in flux associated with the vibrating sample induces an AC voltage in these coils, which is proportional to the magnetic moment of the sample.[39] In SQUID, superconducting detection coils together with quantum mechanical effects are employed.[40, 41] For both measurements, a magnetic moment versus applied field hysteresis loop is recorded. Whereas VSM measurements can be performed relatively quickly, SQUID data acquisition can be slower due to the use of superconducting magnets (which limits the rate at which the magnetic fields can be changed). However, for ultra-thin samples (i.e. small-volume samples), SQUID magnetometry is more suitable due to the increased sensitivity and signal-to-noise ratio; in addition, higher applied fields can be achieved by using a superconducting magnet.

Magnetometry measurements were performed at The Ohio State University using a Lake Shore Cryotronics Model 7400 VSM and a Quantum Design SQUID magnetometer.

The measurements were conducted by Jeremy Lucy (for the results of Chapter 4) and by James Gallagher (for the results of Chapter 6). Measurements were performed in fields up to ± 16 kOe for VSM and ± 30 kOe for SQUID; the samples needed to be cut down to about 0.5 cm × 0.5 cm for all measurements so that they could easily be incorporated into the experimental set-up.

In general, we are interested in the magnetization (magnetic moment per unit volume) values for a given sample. Since most of the error in the magnetization comes from the volume of the sample, careful measurements af the samples' dimensions after cutting were done and an error was obtained. Then, together with thickness values, the volume of a given film was calculated. The errors in the measurement of both sample volume and magnetic moment were propagated in the final values of the magnetization. Also, since all of our FM films are deposited onto a particular substrate, additional measurements of just the substrate were performed; these contributions were then subtracted from the film/substrate hysteresis loops, thus obtaining the signal from the FM films only.

3 Ferromagnetic Manganese Gallium Films on Gallium Nitride: Slightly Manganese-Rich Growth Conditions

3.1 Introduction

Manganese gallium, an important Heusler-type alloy [42, 43], is a promising system for coupling with a SC, since many of its phases are found to be FM at room temperature for both Mn- and Ga-rich regimes.[44–47] In addition, the magnetic properties of MnGa are highly dependent on the Mn:Ga ratio present in the structure, as well as on substrate choice and thermal treatment.[45, 48–52] The properties of Mn-rich MnGa thin films and nanostructures have been thoroughly investigated. Giant PMA, high coercivity and spin polarization are some noteworthy properties that are of great interest in a large pool of applications.[53–61] Considering the less Mn-rich and stoichiometric (Mn:Ga=1) regimes, FM $L1_0$-structured MnGa(111) films have been studied in great detail. A recent paper has reported a study of how structural, electronic and magnetic properties change with stoichiometry for MnGa layers grown by MBE onto wide-gap SC GaN(0001) substrates.[62] The MnGa/GaN bilayer system is very promising due to the wide interest in developing nitride spintronic systems and because of the observed ideal lattice matching and sharp growth interface.[4]

Despite their importance, surface investigations of MnGa alloys in general, or specifically MnGa/GaN, are very sparse in the literature. The focus of this chapter is to present detailed results concerning the surface structure of $L1_0$-structured MnGa ultra-thin films grown on GaN. Out of the two possible polarities of GaN, Ga-polar and N-polar [63, 64], we choose the Ga-polar surface [or GaN(0001)] for MnGa depositions. In general, surface structures during MBE growth can play an essential role in the resultant film properties.[65] For the case of our MnGa films, an important open question is how the surface reconstructions seen in RHEED play a role in determining the magnetic and electronic properties. In other words, it is well-known that as the Mn flux increases, the bulk

film magnetic properties of MnGa change [4, 62]; therefore, we want to understand how Mn atoms incorporate into the surface structure which in turn may tell us how they incorporate into the bulk film.

The results presented in this chapter were published in Applied Physics Letters **103**, 161606 (2013).[66]

3.2 Methods

3.2.1 Experimental methods

The MnGa films are heteroepitaxially grown on freshly deposited GaN(0001) films on commercially available metal-organic chemical vapor deposition (MOCVD) grown GaN(0001)/sapphire substrates. Once solvent cleaned, the GaN(0001) substrate is introduced into the MBE chamber and annealed for 30 min at $\approx 650^{\circ}$C. Then, a film of about 100 nm of GaN is grown at a substrate temperature of $\approx 700^{\circ}$C, upon activating the nitrogen plasma and opening the Ga shutter. The Ga flux and/or substrate temperature are then adjusted slightly until a streaky RHEED pattern is obtained. We verify that a Ga-polar sample was obtained by observing the RHEED patterns at temperatures below 100°C. Once the desired GaN surface is obtained, the substrate temperature is set to $\approx 250^{\circ}$C and MnGa(111) ultra-thin films ($\approx$ 23 nm in height) are deposited while maintaining the Mn to Ga flux ratio at about 1.09. The MnGa films are *not* annealed after growth.

The freshly grown sample is transferred *in-situ* to the adjacent UHV analysis chamber for RT STM and AES studies. After removal from the vacuum chamber, RBS measurements are performed in order to establish the film stoichiometry.

3.2.2 Theoretical calculations

Calculations are carried out using spin polarized DFT as is implemented in the plane waves-self-consistent field code from Quantum ESPRESSO.[67] The Exchange-Correlation

functional is treated within the Generalized Gradient Approximation with the Perdew-Burke-Ernzerhof parametrization.[68] The electron-ion interaction is calculated using ultra-soft pseudo-potentials.[69] The energy cutoff used is 30 Ry. Bulk parameters (a and c) are optimized for the FM case, which is found to have the lowest energy. For the surface energy calculations, the super-cell approximation is used in which a slab with an artificial periodicity along the z direction is created. Each slab consists of seven atomic (111) layers with four atoms per layer and a 2×2 in-plane periodicity. Each of the inner five layers contains two Ga and two Mn atoms, corresponding to two 1×2 ideal bulk MnGa(111) unit cells. The bottom and top most layers have a variable number of Ga and Mn atoms, according to the calculated geometry. A vacuum space of more than 10 Å is used between slabs in order to avoid interactions. Simulations of STM images are obtained by using the Tersoff-Hamman approximation.[70]

3.3 Results and discussion

3.3.1 Growth and surface structure

Figures 3.1(a) and 3.1(b) show the RHEED patterns obtained along two high-symmetry azimuths of a freshly deposited GaN film. The streaky pseudo-1×1 patterns of this Ga-polar surface are indicative of atomically-smooth surfaces.[64] Figures 3.1(c) and 3.1(d) show RHEED patterns recorded during growth for the MnGa over-layers taken along the GaN $[11\bar{2}0]$ and $[1\bar{1}00]$ azimuths, respectively. These directions correspond to $[11\bar{2}]$ and $[1\bar{1}0]$ directions of MnGa(111), as previously established; also, the fact that the RHEED patterns of MnGa are opposite to those of GaN reveals that MnGa(111) hexagonal-like lattice grows with a 30° rotation with respect to the GaN substrate.[4] It can be observed that very sharp MnGa RHEED streaks are obtained, suggestive of high-quality epitaxial growth; additional $2 \times$ streaks are observed along both directions of MnGa and they indicate a 2×2 surface reconstruction.

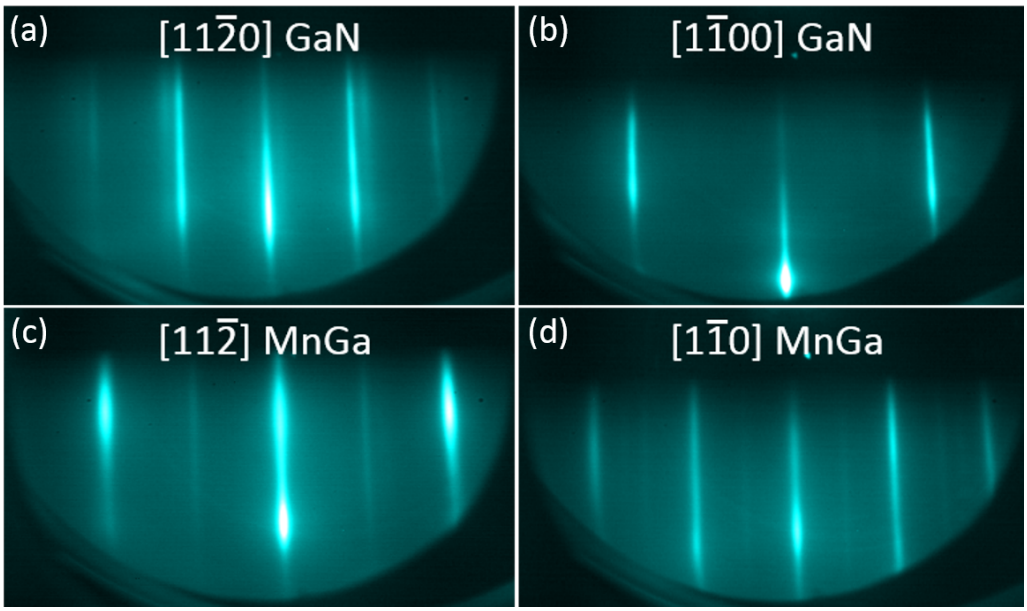

Figure 3.1: (a) and (b) RHEED patterns recorded for the GaN film upon cooling below 100°C. (c) and (d) RHEED patterns of MnGa obtained during growth and taken along GaN [11$\bar{2}$0] and [1$\bar{1}$00] azimuths, corresponding to [11$\bar{2}$] and [1$\bar{1}$0] directions of MnGa, respectively.

The high-quality epitaxial growth observed from RHEED also reflects in the surface quality of MnGa. Figure 3.2(a) shows a 3D-rendered, atomic-row-resolved STM image of an atomically smooth (111) surface of an ultra-thin MnGa film grown as described above, acquired at a (sample) bias voltage V_S = -11.0 mV and tunneling current I_T = 279 pA. Clear abrupt atomic steps and smooth terraces are characteristic of the surface. The step height is measured to be ≈ 2.2 Å, consistent with known experimental lattice constants[4, 62] as well as values based on theoretical calculation, assuming that the surface normal is [111]. The row-row spacing is measured to be ≈ 4.6 Å, which is equal to twice the primitive atomic row spacing in the (111) plane for MnGa along [11$\bar{2}$].

The fact that atomic rows run parallel to some step edges and at ≈ 60° to other step edges is more clearly seen in the plan-view STM image presented in Fig. 3.2(b). There, we see that the row structure is closely linked to the step edge structure. We also notice that the

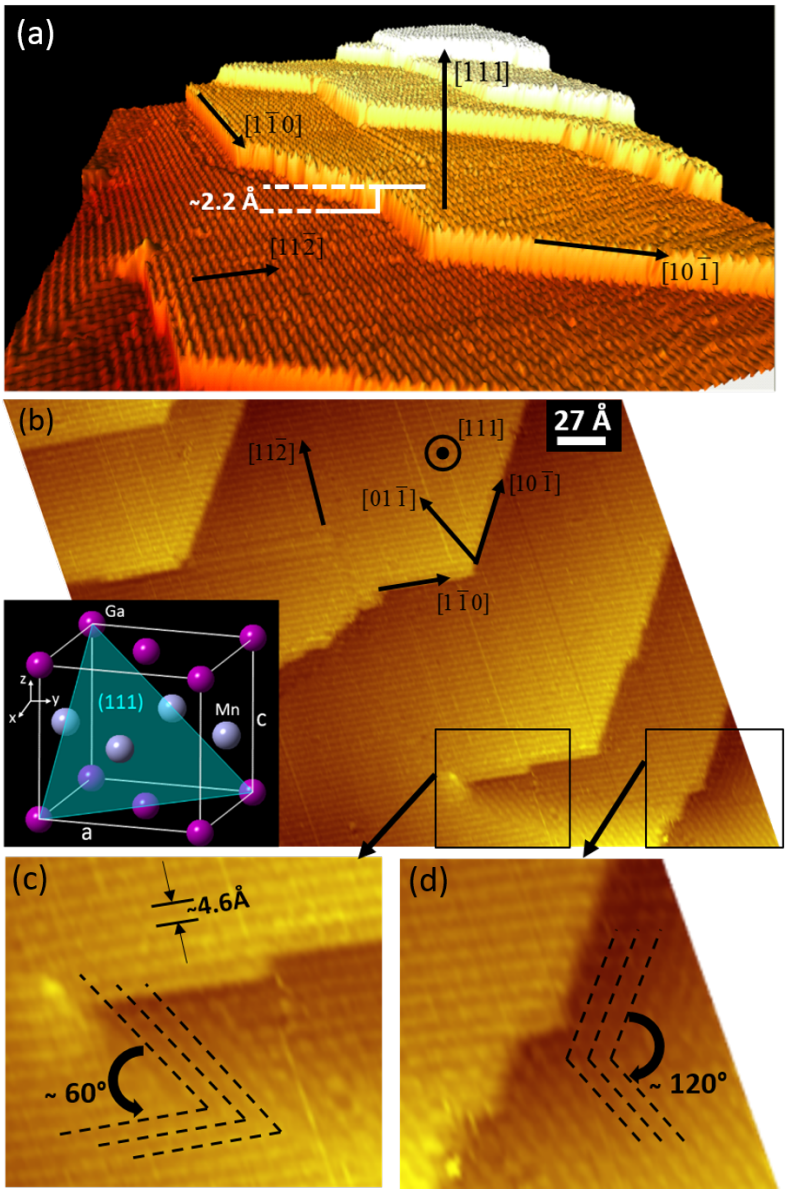

Figure 3.2: (a) 3D-rendered image of the single atomic steps observed in the MnGa epitaxial structure. (b) Normal plan view STM image of the MnGa structure shown in (a) after drift correction; the inset shows the face-centered tetragonal structure of MnGa, with the (111) plane highlighted. Scanning parameters: V_S = -11.0 mV and I_T = 279 pA. (c) and (d) Zoom-in views corresponding to the rectangular boxed areas indicated in (b) showing different domains which come together at ≈60° and ≈120°, respectively.

atomic rows on adjacent terraces typically run in the same direction. However, this is not always the case, as can be seen inside the black boxed regions in Fig. 3.2(b); zoom-ins of

those regions are shown in Figs. 3.2(c) and 3.2(d) where the atomic rows in some areas run at $\approx 60^\circ$ or $\approx 120^\circ$ to nearby areas, suggesting the existence of rotated crystalline domains. The approximately 60° rotated domains can be explained by the fact that a stoichiometric MnGa film has only twofold symmetry about [111] while the GaN substrate has threefold symmetry about [0001]. Thus, the formation of three rotated domains naturally occurs during heteroepitaxy as nucleation takes place.

Thus we have the peculiar situation that although the row-like structure of the surface indicates twofold symmetry, the tendency of the surface to form steps edges at 60° and 120° to each other reveals the nearly hexagonal (hexagon-like) nature of the (111) MnGa surface, consistent with the well-known film-substrate epitaxial lattice matching as found by RHEED.[4] In fact, MnGa is a face-centered tetragonal crystal, not a perfect cube; but the STM images reveal that atomic diffusion and surface step energetics favor the formation of step edges running along $[1\bar{1}0]$, $[01\bar{1}]$, and $[10\bar{1}]$ (i.e. hexagon-like surface directions), as indicated in Fig. 3.2(b).

With a very sharp STM tip, row-like regions such as those shown in Fig. 3.2(b) can be atomically resolved into a hexagonal-like 2×2 structure, as shown in Fig. 3.3(a). As clear from this figure, the 2×2 is very well ordered, appearing as a protrusion-type structure. This structure is believed to form under Mn-rich conditions and is observed as a 2×2 RHEED pattern while growing the film. It was proposed by Lu *et al.* that excessive Mn at the surface could result in a periodic substitution of Mn into Ga sites, leading to a 2×2 substitutional model as shown in Fig. 3.3(d).[4] As shown in Fig. 3.3(b), the line section measurement along $[1\bar{1}0]$ reveals a periodicity of ≈ 5.4 Å, agreeing very well with twice the Mn-Ga interatomic spacing, corresponding to $2 \times$, as seen in the model of Fig. 3.3(d). Along $[11\bar{2}]$, the line section shows a high peak - low peak profile where the spacing between high peaks is ≈ 9.2 Å and the spacing between high and low peaks is ≈ 4.6 Å, the inter-row spacing

[see Fig. 3.3(c)]. The low peak corresponds to the saddle point between neighboring bright peaks in the STM image.

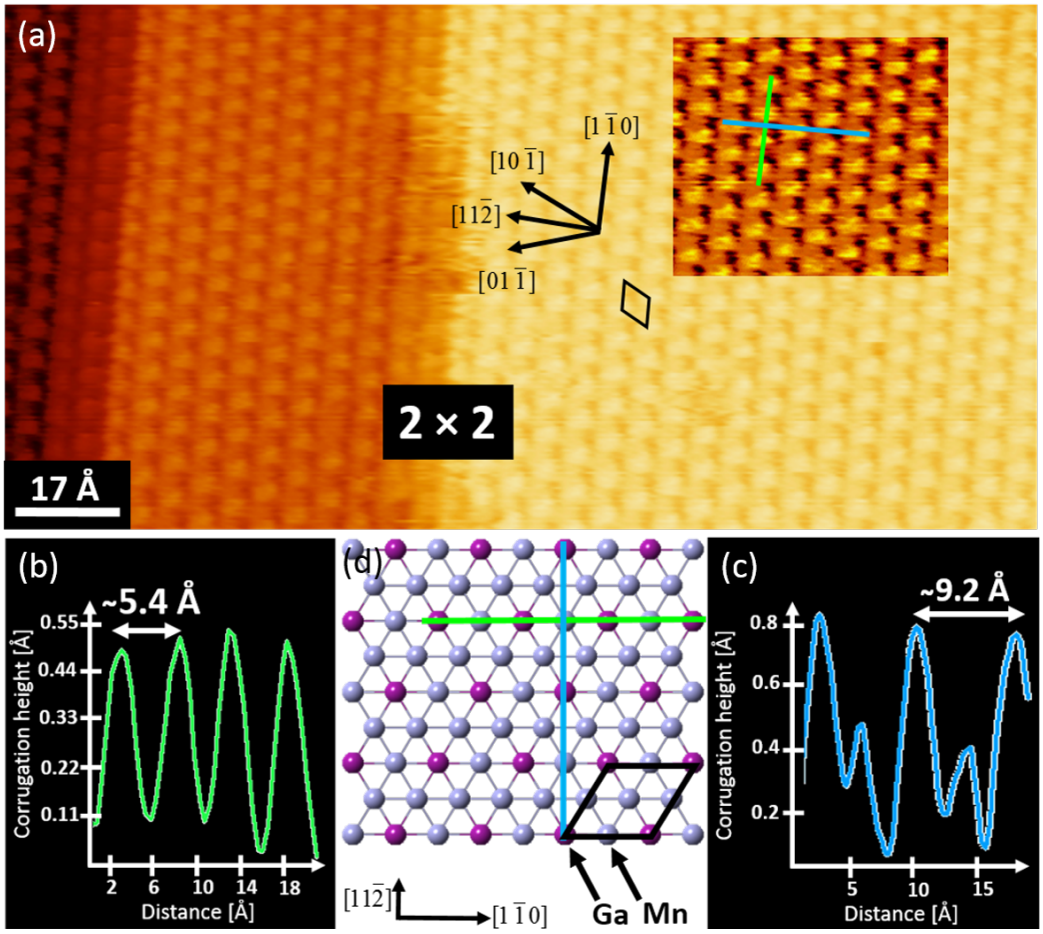

Figure 3.3: (a) STM image taken on another area of the same sample, showing a 2 × 2 (hexagonal-like) surface reconstruction of MnGa; a piece of the upper (bright) terrace was adjusted for contrast, and line profiles were taken along the green and blue path lines. Scanning parameters: V_S = -12.3 mV and I_T = 402 pA. A simple flattening was applied to the image. (b) and (c) Line profiles along the paths shown in (a). (d) Theoretical model for the 2 × 2 reconstruction, showing the paths (green and blue lines) corresponding to the line profile paths in (a).

3.3.2 Comparison with theory

Comparing the 2×2 line profiles to the substitutional model in Fig. 3.3(d), it appears that the Ga atoms protrude more than the Mn atoms in the STM image. Since clearly it is important to evaluate the 2×2 model theoretically, we have carried out calculations to determine which atoms in a substitutional model dominate the local density of states (LDOS) and as well the formation energy of this model in comparison to energies of competing 2×2 models such as adatom models. Lattice parameters a and c were also calculated for the bulk $L1_0$ FM structure and they were found to be 3.83 Å and 3.72 Å, respectively. These values are in good agreement with previous experimental measurements.[52, 62, 71]

Shown in Fig. 3.4 is a plot of surface formation energies for various structural models considered for the cases of both 1×2 and 2×2 structures observed in the STM images. The models include ideal (1Ga 1Mn), vacancy (1Ga, 1Mn), adatom (Ga, Mn), and substitutional (3Ga 1Mn, 1Ga 3Mn). As can be seen, the substitutional and ideal models are found to be lowest in energy within separate ranges of the chemical potential considered. In particular, the 1Ga 3Mn model is lowest in energy over the Mn-rich regime, followed by the ideal model within an intermediate regime, followed by the 3Ga 1Mn model over the Ga-rich regime. The fact that either ideal or simple substitutional models are preferred is consistent with experimental observations (from both STM and MBE growth) of either $1 \times$ or $2 \times$ structures in the vicinity of the stoichiometric flux ratio; this allows for a smooth variation of film stoichiometries to be obtained. In subsequent comparisons between experiment and theory, STM simulations are only done for the ideal and substitutional models, namely the ideal 1Ga 1Mn 1×2 and the substitutional 1Ga 3Mn 2×2.

Referring now to Fig. 3.5, a direct comparison is made between the 2×2 from the experiment and the 2×2 from the theoretical calculation. Presented in Fig. 3.5(a) is the simulated STM image at distance of 3.0 Å above the surface and corresponding to the experimental STM image with V_S of -12.3 mV; I_T for the experimental STM image is 402

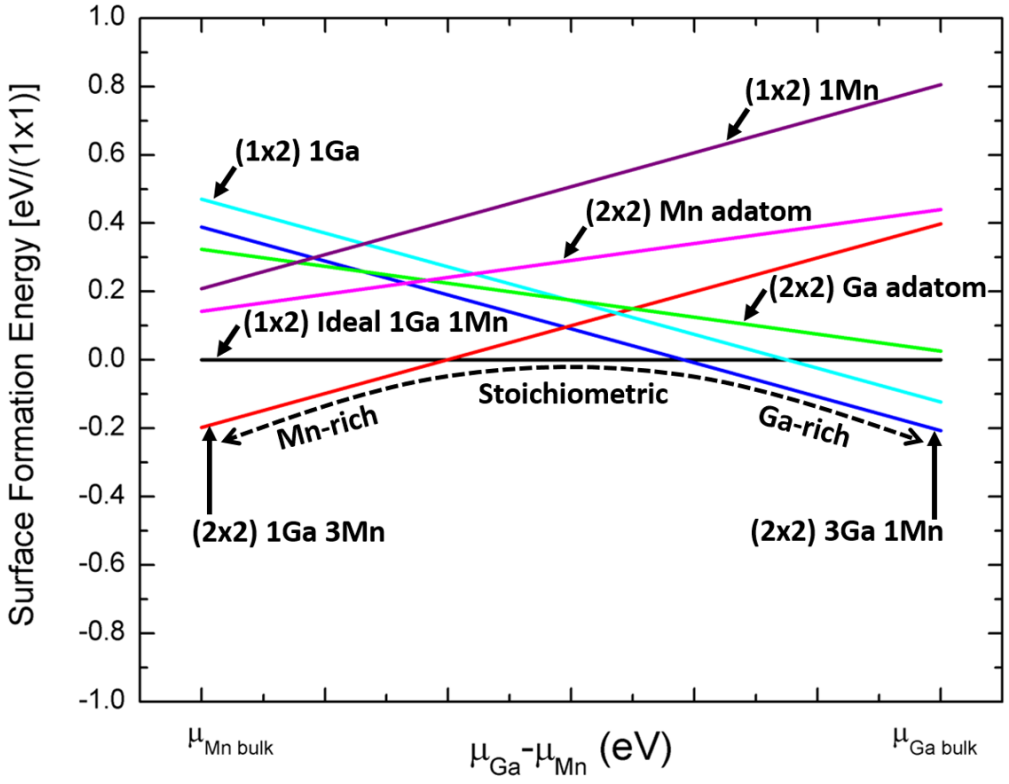

Figure 3.4: Surface formation energy plot for various MnGa surface structure models ranging from a Mn-rich 2×2 (1Ga 3Mn) to the ideal stoichiometric 1×2 (1Ga 1Mn) to a Ga-rich 2×2 (3Ga 1Mn). Also included are both vacancy (1Ga, 1Mn) and Ga/Mn adatom models for 1×2 and 2×2 structures, respectively.

pA. Overlaid onto the simulated image is the 2×2 substitutional model showing registry between the simulation and the atomic positions of the model; these are then compared to the actual STM image with similar model overlay in Fig. 3.5(b).

As seen, the agreement between theory and experiment is very good. Bright features in the STM image are reproduced in the simulation at 2×2 symmetry positions. The positions of the bright features correspond to the Ga sites. The Mn atoms protrude less than the Ga atoms, and this is observed in both simulated and actual STM images. Calculations involving different orbitals around the Fermi level indicate that the Mn atoms dominate the LDOS, in agreement with previous results [72]; however, the LDOS of each Mn is very

localized around the atom. Theoretically, since the two Mn atoms in the Mn row [see Fig. 3.5(a)] are lower than the Mn and Ga (which are at the same height) in the Mn-Ga row by 0.15 Å, and due to the delocalized nature of the Ga atom density, the Ga atom appears brighter. Note that these calculated atomic height differences are not to be compared to the STM corrugations.

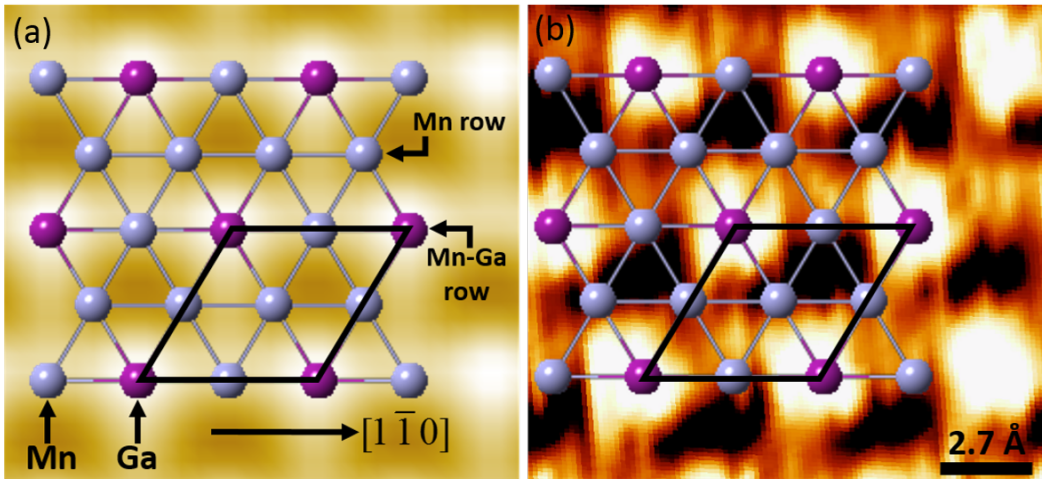

Figure 3.5: Simulated (a) and experimental (b) STM images for the Mn-rich 2 × 2 reconstruction. The theoretical model from Fig. 3.3(d) was overlaid on both images. The simulation in (a) corresponds to the bias voltage of -12.3 mV for the experimental STM image in (b). STM tunneling current is I_T = 402 pA.

From MBE RHEED measurements a 1 × 2 is also commonly seen, and as well this is found in the STM images. Shown in Fig. 3.6(a) is a region of the same sample containing both the 2 × 2 (lower left corner) and the 1 × 2 (directly adjacent), and as well a third type of reconstruction shown in the middle to upper right corner of the image which has a symmetry of 2 × 3. This third structure is much less common on the studied sample but most likely corresponds to a region with slightly higher (or possibly, lower) Mn concentration. The two domains of the 2 × 3 reconstruction look similar but actually have slightly different structure, intersecting at ≈ 90°, corresponding to the surface azimuthal directions [1$\bar{1}$0] and [11$\bar{2}$].

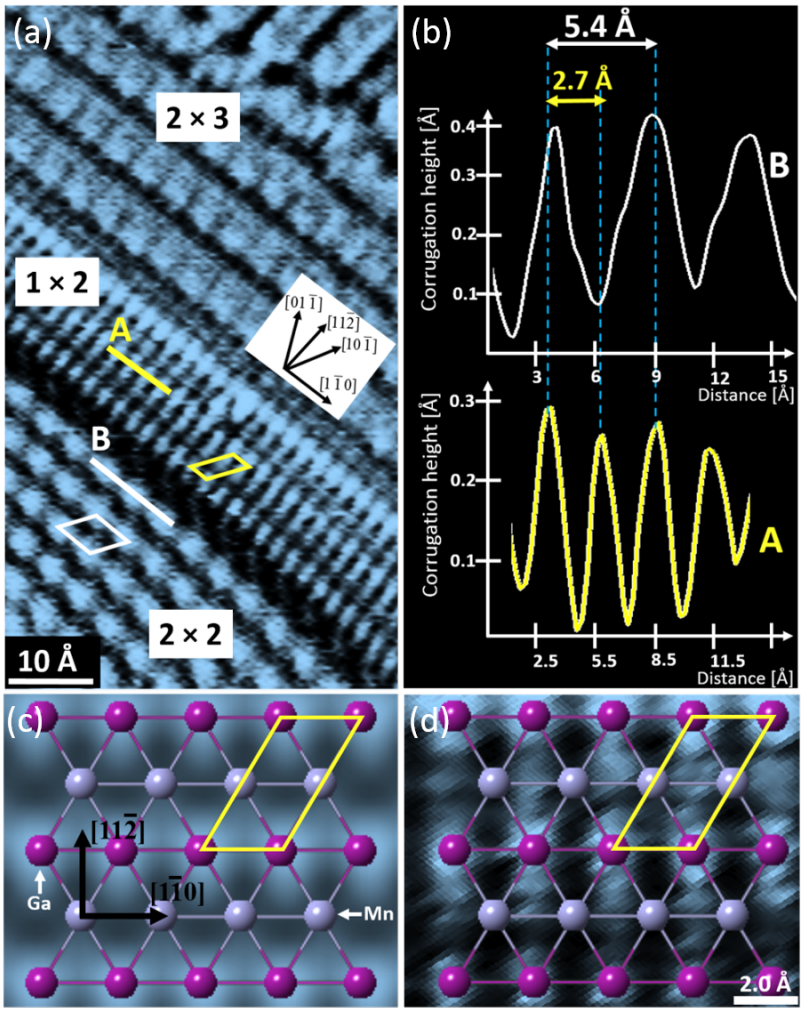

Figure 3.6: (a) STM image taken on a different region of the same sample. Three different reconstructions are observed: a 2×2 (lower left corner), a row-like 1×2 (center region), and a more complex one in the remaining space. Scanning parameters: V_S = -6.2 mV and I_T = 293 pA. (b) Line profiles for the 1×2 (A) and 2×2 (B) showing the double spacing of the 2×2 as compared to the 1×2. (c) and (d) Simulated and experimental [zoomed from (a)] STM images for the 1×2, corresponding to the bias voltage V_S = -6.2 mV. The theoretical model for the 1×2 was overlaid on both images.

To verify the 2×2 and 1×2 spacings, line sections are shown in Fig. 3.6(b). There one sees that the corrugation spacing along $[1\bar{1}0]$ for the 2×2 is exactly 2 times the spacing of the 1×2, as expected, which is also clear from the image.

It may be seen that the 1×2 region is actually a small domain on the surface, surprising given that the Mn:Ga flux ratio was so close to 1:1. Nonetheless, we can directly compare the experimental STM image of the 1×2 with the 1×2 simulation based on theoretical calculations, and this is done in Figs. 3.6(c) and 3.6(d). Together with the model overlays, theory and experiment are found to agree very well with each other, with the bright features in the STM image corresponding to the Ga sites in the model.

3.3.3 Connection with RBS and AES results

Despite very good agreement between the STM images and theoretical simulations, an important question comes up since we see in the experiment that only very little of the surface has the stoichiometric 1×2 structure. A relatively large fraction of the surface corresponds to the 3:1 Mn:Ga ratio. This is very interesting since the intended Mn:Ga flux ratio was only 1.09. Based on that, one would expect to find most of the surface having the stoichiometric 1×2 structure and only very little of the 2×2 Mn-rich structure. Therefore, we carried out RBS measurements on the same sample, and based on those measurements we find that the 23 nm thick film has a Mn:Ga composition ratio of 0.99 ± 0.05, thus giving a 60% (40%) confidence that the bulk sample is Ga-rich (Mn-rich). Moreover, we can say with almost 100% confidence that the bulk film has stoichiometry less than the intended 1.09. These RBS numbers are unlikely to be affected by film roughness since the rms roughness is very small, only 0.4 nm.

An estimate of the overall surface composition based on sampling of STM images resulted in a weighted average Mn:Ga ratio of 3.0 ± 0.1. This value was obtained by considering that the 2×2 reconstruction (with Mn:Ga ratio of 3:1) represents $\approx 80\%$ of the surface, the 1×2 (with Mn:Ga ratio of 1:1) $\approx 2\%$, and the 2×3 (with Mn:Ga ratio ranging from 2:1 to 4:1, since we do not know the exact proportions) the remaining $\approx 18\%$. To further verify the surface composition of the film, we carried out AES measurements,

finding a Mn:Ga ratio of 1.4 ± 0.1 after correcting the Mn and Ga derivative spectra for sensitivity factors. Of course, we would not expect a number larger than this since AES is also sensitive to the underlying stoichiometric layers. A rough prediction of the AES result can be done by assuming the contributions from one surface layer (having a Mn:Ga ratio of 3:1) and four bulk layers (with 1:1 stoichiometry). The resulting value of such an estimate, assuming an exponential diminishing of the contributions, is found to be 1.8 ± 0.1. This number is within two standard deviations from the measured AES value.

Resolving of these two seemingly conflicting results, namely a higher-than-expected Mn concentration in the surface as well as a lower-than-expected Mn concentration in the bulk, leads to the following conclusion. Evidently, MnGa growth proceeds with preferential Mn segregation to the surface. Slightly Mn-rich flux conditions lead to very Mn-rich surfaces, while simultaneously less Mn incorporates into the bulk. In order to achieve a stoichiometric film, it may thus be necessary to grow under slightly Mn-rich conditions, with the added advantage that the lower surface energy leads to very smooth growth.

3.4 Conclusions and future directions

Manganese gallium samples grown under epitaxially smooth and slightly Mn-rich growth conditions were investigated using STM. It is found that the growth surface is highly epitaxial with a clear step/terrace structure. The results for the observed 1×2 and 2×2 structures were compared to structural models and simulated STM images from theoretical calculations. The energies of various models were also presented in order to further establish the locations of the individual atomic species within the two reconstructions. Very good agreement between the STM images and the simulations was found, with Ga atoms dominating the images for both the 2×2 and 1×2 reconstructions.

This study highlights the important relationship between surface and bulk, finding that under slightly Mn-rich growth conditions the Mn atoms in MnGa incorporate at different

rates: surfaces become highly Mn-rich, while the bulk retains a 1:1 stoichiometry. Such behavior reveals a potential recipe for tuning, for example, magnetic properties by carefully controlling the surface reconstruction during growth.

From these results, it is clear that MnGa is very sensitive to the ratio of elements in the structure; in addition, the imbalance in the number of atoms at the surface can affect the properties, becoming crucial as the films thickness decreases. Future work looking with STM at the surface structure and quality as a function of varied flux conditions and film thicknesses could provide further insights into how Mn atoms incorporate into the surface/bulk, and also into some of the overall film properties.

4 Transitioning into the Gallium-Rich Regime of Ferromagnetic Manganese Gallium Films on Gallium Nitride

4.1 Introduction

A natural question that follows from the previous study is how the surfaces and overall properties of MnGa change with composition. Despite the extensive literature on Mn-rich and stoichiometric MnGa alloys, the Ga-rich regime has received far less attention.[49, 73–76] In particular, the growth, structure, and magnetism of Ga-rich MnGa when deposited onto wide-gap GaN are still not addressed. From a technological point of view, in addition to having useful magnetic properties, an important requirement is to obtain epitaxial films with (atomically) smooth surfaces and sharp interfaces. We have therefore combined several techniques to study the structure, surface, and magnetic properties of MnGa films grown on GaN(0001) over a range of Mn:Ga composition ratios that covers the Ga-rich regime. Since the magnetic properties of MnGa alloys in general are dependent on the layer thickness, we have also investigated films with varying thicknesses. By exploring how all these properties change as we cross the stoichiometric limit into the Ga-rich side, a more comprehensive understanding of the MnGa system can be achieved, ultimately adding useful information to a larger spectrum of Mn:Ga compositions.

The results presented in this chapter were published in Applied Surface Science **367**, 312 (2016).[77]

4.2 Methods

The MnGa films are grown using MBE following the same recipe as already described in Chapter 3. The Mn:Ga composition ratios in this case are varied from ≈ 1.00 (stoichiometric) to ≈ 0.42 (very Ga-rich), and thin (≈ 30 nm and ≈ 50 nm) and ultra-

thin (≈ 3.3 nm and ≈ 7.8 nm) samples are investigated. Similar to the previous study, the MnGa films are *not* annealed after growth.

After preparation, the samples are transferred *in-situ* to the adjacent UHV analysis chamber, where RT STM and AES surface studies are performed. Following removal from the vacuum chamber, structural and magnetic characterizations are performed. The orientation of the MnGa films is determined by XRD. The composition of the 30 nm and 50 nm thick samples is determined by RBS. Magnetometry measurements are performed on the thin samples using VSM at RT and in fields ranging from +16 kOe to -16 kOe for field directions both *in-plane* (0° ± 0.5°) and *out-of-plane* (90° ± 0.5°). Magnetic characterization for the ultra-thin samples are performed at RT using a SQUID magnetometer with applied fields of up to ± 30 kOe for both the *in-plane* and *out-of-plane* sample geometries. The diamagnetic contribution of the GaN substrate is subtracted from both VSM and SQUID hysteresis loops. *Ex-situ* imaging is also performed using an atomic force microscope operated in dynamic mode.

4.3 Results and discussion

4.3.1 Structural results

Table 4.1 indicates the measured bulk (RBS) Mn:Ga ratios for the five thin MnGa films [no RBS measurements were performed on the ultra-thin samples, F and G, due to their small MnGa film thickness]. It can be seen that the Mn:Ga ratio varies from stoichiometric 1:1 (Sample A) to very Ga rich (sample E). Corresponding XRD scans are shown in Fig. 4.1(a), with 2θ spanning 40°-50° (the scans were taken over a wider 2θ range, but we only show the region in which the main MnGa peaks appear).

Comparing the RBS and XRD measurements, we obtain very good agreement between bulk Mn:Ga ratios and the observed phases. For samples A and B, the main phases are identified as corresponding to $L1_0$ MnGa, as expected. As the Ga concentration increases

Table 4.1: MnGa film thickness, Mn:Ga RBS and Mn:Ga AES ratios. The values marked with † are estimated given the coverage observed in AFM (see text for details).

Sample	MnGa film thickness [nm]	Mn:Ga RBS ratio	Mn:Ga AES ratio
A	50.0 ± 2.0	1.00 ± 0.15	1.21 ± 0.24
B	50.0 ± 2.0	0.95 ± 0.10	1.02 ± 0.20
C	50.0 ± 2.0	0.81 ± 0.08	0.95 ± 0.19
D	50.0 ± 2.0	0.58 ± 0.06	0.61 ± 0.12
E	30.0 ± 1.0	0.42 ± 0.08	0.45 ± 0.09
F	3.3 ± 0.3	-	0.98 ± 0.19
G	7.8 ± 1.8†	-	0.56 ± 0.11†

(sample C), we observe the coexistence of $L1_0$ MnGa and more Ga-rich phases, namely Mn_3Ga_5 and Mn_2Ga_5. Figure 4.1(b) shows the region in which MnGa(111) peaks appear for samples A, B, and C; as the Mn concentration increases a slight shift to the right is evident, in excellent agreement with previous observations by Bedoya-Pinto *et al.* [62] This shift is attributed to small changes in the d_{111} spacing as a result of changes in lattice parameter c. A plot showing the evolution of d_{111} spacing with sample stoichiometry is also shown in Fig. 4.1(b). We also find that the $L1_0$ phase is preserved down to a Mn:Ga ratio of 0.81, in agreement with previous reports.[60]

For samples D and E, the MnGa peaks disappear completely and only the two main Ga-rich phases are observed. For purely one phase samples containing either Mn_3Ga_5 (Mn:Ga ≈ 3:5) or Mn_2Ga_5 (Mn:Ga ≈ 2:5), we would expect to have Mn:Ga RBS ratios of ≈ 0.6 and ≈ 0.4, respectively. In turn, we measure slightly less than 0.6 for sample D - implying that we have some 2:5, and slightly more than 0.4 on sample E - agreeing again with the XRD data, which shows amounts of 3:5. Indeed, for alloys with a nominal composition $Mn_{37}Ga_{65}$, both Mn_3Ga_5 and Mn_2Ga_5 were found within the same crystal, although by further annealing

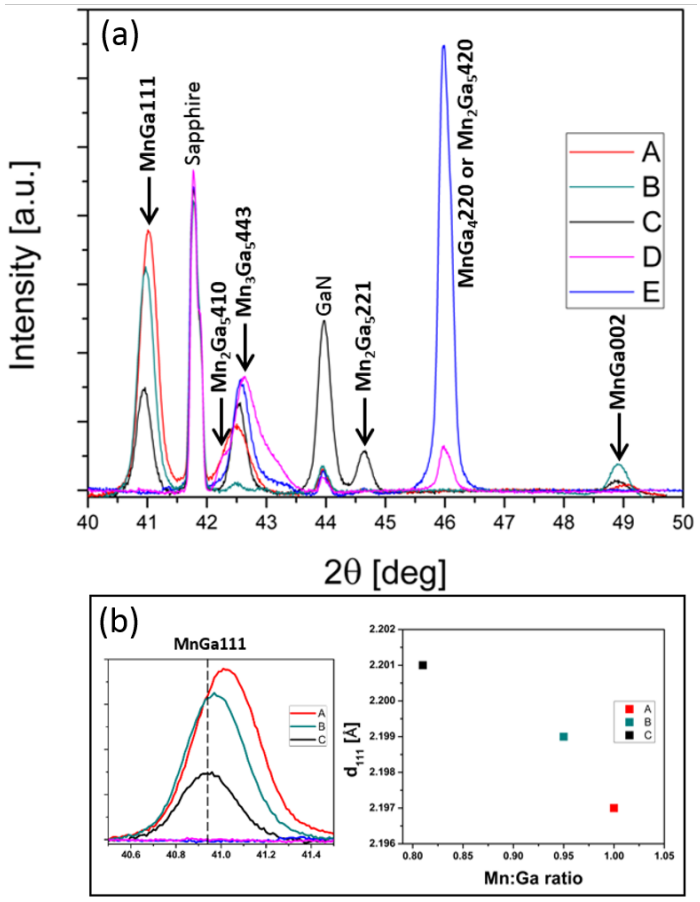

Figure 4.1: (a) θ-2θ XRD scans for MnGa films grown on GaN(0001); sample compositions range from stoichiometric (Mn:Ga $\approx$ 1) for sample A to highly Ga-rich (Mn:Ga $\approx$ 0.42) for sample E. (b) The evolution of d_{111} with sample stoichiometry as determined from shifts in the MnGa111 peak region for the more Mn-rich samples, A, B, and C.

only the stable Mn_3Ga_5 was preserved.[78] We note that the Mn:Ga composition ratio of $Mn_{37}Ga_{65}$, i.e. 0.587, is very close to our measured RBS Mn:Ga ratio of $\approx$ 0.58 for sample D.

Lattice parameters (a and c) and interplanar distances (d_{hkl}) for the observed phases and orientations are indicated in Table 4.2; we also report the lattice parameters for bulk samples.[46, 71, 75, 76] The three main phases observed in XRD are known to be tetragonal [4, 46, 75], although the peak at $\approx 46^\circ$ could also be identified as corresponding to the

Table 4.2: MnGa phases, lattice parameters and orientations as obtained from XRD; reference columns a^* and c^* represent values for bulk samples, taken from [71], [75], [46], and [76]. The values for the MnGa phase correspond to stoichiometric (Mn:Ga=1) sample A.

Phase	a [Å]	c [Å]	a^* [Å]	c^* [Å]	hkl	d [Å]
MnGa	3.85	3.72	3.89 [71]	3.65 [71]	111 002	2.197 1.86
Mn_3Ga_5	12.49	25.00	12.66 [75]	24.62 [75]	443	2.13
Mn_2Ga_5	8.82	2.68	8.86 [46]	2.71 [46]	410 420 221	2.14 1.97 1.97
$MnGa_4$	5.57	-	5.59 [76]	-	220	1.97

cubic $MnGa_4$ crystal. However, based on RBS and AES values (discussed below) it is more probable that this peak corresponds to Mn_2Ga_5 for our samples.

4.3.2 Surface studies

Referring back to Table 4.1, we can now compare the surface AES and bulk RBS Mn:Ga ratios. As it can be seen, the agreement is excellent for samples D and E, showing that these films are Ga-rich in both bulk and on the surface. Somewhat larger discrepancies are observed for samples A, B, and C; these differences can be explained by the appearance of highly 2×2 Mn-rich surfaces (described in the previous chapter), where although the bulk of the film was stoichiometric, the surfaces presented mainly a Mn-rich 2×2 reconstruction. This same reconstruction is observed (in varying amounts) on samples A, B, and C (see STM discussion below), thus giving rise to Mn:Ga AES ratios larger than RBS values.

For the case of ultra-thin sample F, AES measurements indicate that this sample is closest in surface composition to samples B and C (see Table 4.1). Indeed, STM

investigations reveal similar structures on all of these samples. Figure 4.2(a) shows an STM image taken on sample F, where two main surface structures are visible. The featureless (lower) areas, when better resolved, can be identified as the well-studied Mn-rich 2×2 surface reconstruction (see inset). On the top left corner (upper region) we observe row structures intersecting at $\approx 90^{\circ}$ and with varying periodicities. A closer look at the row structure is shown in Fig. 4.2(b); it can be seen that the rows are separated by either ≈ 9.2 Å or ≈ 12.1 Å, and are interrupted by grid- and double stripe-like patterns, emphasized by the square and rectangular boxes, respectively. This structure has been previously observed by STM on similar samples and briefly described in the previous chapter, where it was identified as a minority phase. While the 2×2 reconstruction seems to be independent of the film thickness, the row region becomes less complex as the thickness of the film increases. An STM image taken on sample B, and presented in the inset of Fig. 4.2(b), shows the evolution of this row structure with increasing film thickness. Atomic arrangements such as those indicated by the square and rectangular boxes in Fig. 4.2(b) are no longer visible; instead, structures having 3- and 4-row periodicities become dominant.

The exact surface Mn:Ga composition ratio for the row structure is unknown; it could be less Mn-rich than the 2×2 structure or it can even be very Ga-rich. In addition, the row and 2×2 structures can be found in varying amounts on the surface of a given sample, thus leading to different Mn:Ga surface ratios for samples A, B, C, and F. Being the most Mn-rich in bulk, using STM sample A is found to also exhibit the largest amount of 2×2, consistent with higher AES ratios (see Table 4.1).

Considering now the more Ga-rich samples, when measuring the Mn:Ga AES ratio for sample G, a N peak is detected in addition to Ga and Mn peaks, an indication that the GaN layers are also probed. Therefore, a representative ratio for this sample is not easily measured, since the Ga peak is proportional to the total number of Ga atoms, from both MnGa and GaN surface layers (this observation does not apply to sample F since N is not

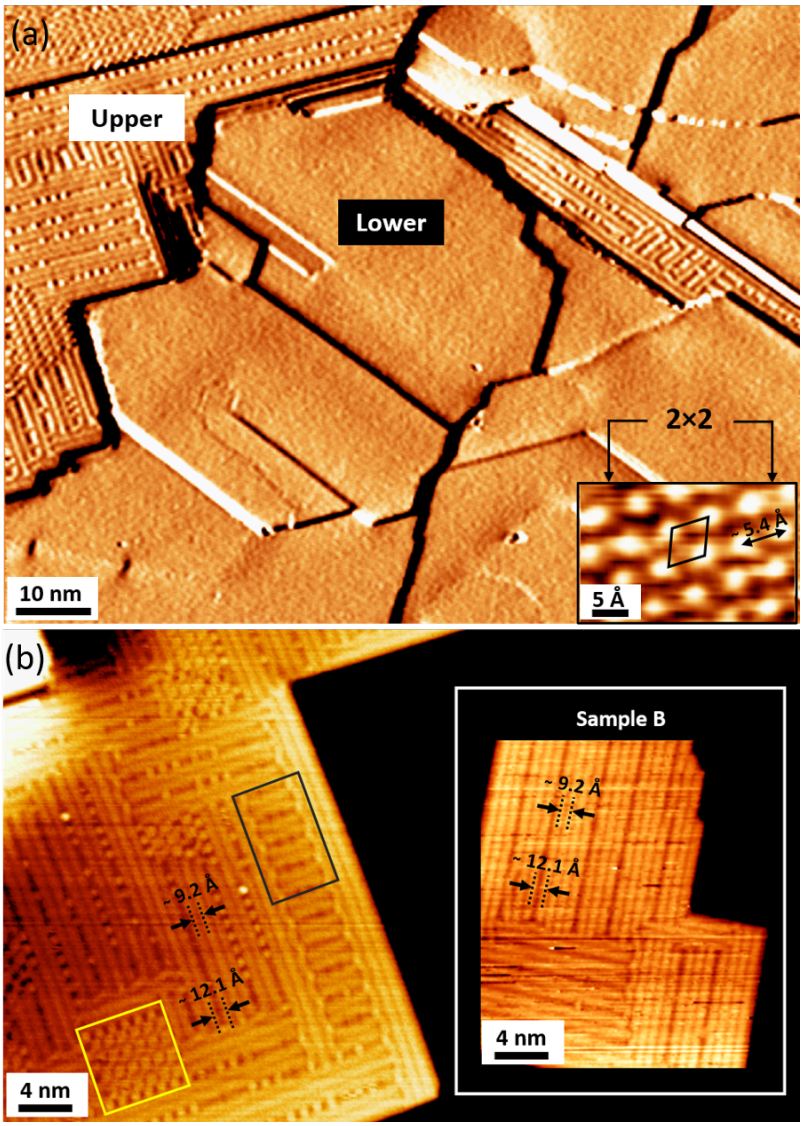

Figure 4.2: (a) Room temperature STM image (shown in derivative mode) taken on sample F and acquired at a sample bias V_S = -300 mV and tunneling current I_T = 0.1 nA; the inset shows the 2 × 2 reconstruction observed on the lower terraces. (b) STM image taken on the upper region in (a) [scanning parameters: V_S = -300 mV and I_T = 0.1 nA], where row structures with two different periodicities (≈ 9.2 Å and ≈ 12 Å) are mainly visible; enclosed by square and rectangular boxes are different atomic arrangements that appear in addition to the row structures. The inset from (b) represents an STM image taken on sample B, showing the evolution of the structure in (b) as the film thickness increases [scanning parameters: V_S = -100 mV and I_T = 0.1 nA].

detected in the AES spectrum). However, the N peak can be explained by looking at Fig. 4.3(a), which shows a 10 µm × 10 µm AFM scan of sample G. It can be seen that the growth is not uniform and results in the formation of 3D islands. These islands cover ≈ 46 % of the surface and their heights are measured to be on average ≈ 17 nm; based on the measured coverage, this height corresponds to a uniform MnGa film of ≈ 7.8 nm, as given in Table 4.1. The Mn:Ga AES ratio reported in Table 4.1 for sample G is an estimate based on the contribution to the AES signal of only Ga atoms contained in the MnGa islands visible in the AFM scans. This way, we find that sample G is close in surface composition to sample D. In fact, this conclusion is also supported by comparing STM images taken on samples D and G, from where we find similar surface structures (see STM results below). By looking at Fig. 4.3(b), which shows a 10 µm × 10 µm AFM scan of sample D, it can be observed that as the thickness increases the sample morphology is preserved and the film becomes more uniform, with GaN layers no longer visible.

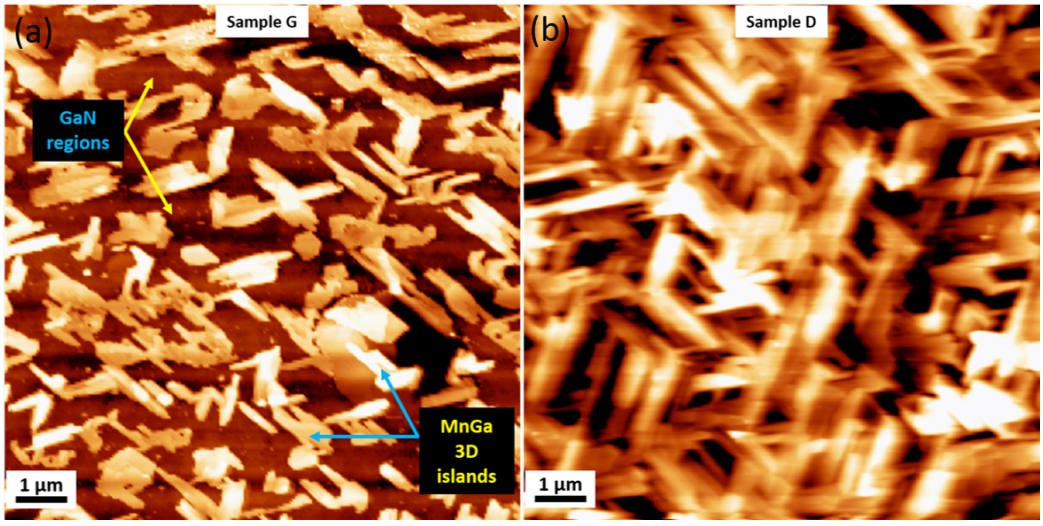

Figure 4.3: (a) 10 µm × 10 µm AFM image taken on sample G; 3D MnGa islands cover ≈ 46 % of the surface, with the remainder of ≈ 54 % consisting of exposed GaN layers. (a) 10 µm × 10 µm AFM image taken on sample D; it can be seen that as the thickness increases, the film becomes more uniform.

Upon investigating the surface of sample G with STM, two distinct and adjacent row structures are mainly observed and they are shown in Fig. 4.4(a) [presented in derivative mode]: i) on the left (lower) terrace, a relatively uniform row structure can be seen; ii) on the right (upper) terrace, a more complex row structure is visible, consisting of interrupted raised rows (some indicated by arrows) and small patches of more uniform arrangements (highlighted by the dashed box). The difference in height between the left and right regions varies between 1.6 nm and 2.3 nm, in agreement with AFM height measurements on a given island.

A 3D perspective view of the area shown in Fig. 4.4(a), with emphasis on the lower region, is presented in Fig. 4.4(b). The uniform row region shows a large modulation on the surface, with a wavelength of about 35 nm and an amplitude of $\approx$ 1 Å. This type of surface effect is unique to ultra-thin sample G and can be explained by composition and/or strain gradients within the structure.[80, 81] It is well known that the stability of the film surface can be influenced by the degree of lattice mismatch between the film and the substrate, leading, for example, to changes from layer-to-layer into 3D island growth; the film surface can also be influenced by stresses generated by compositional inhomogeneities. Some examples include the well-studied InGaN/GaN and SiGe/Si systems.[82–84] In these strained structures, the degree of relaxation was found to affect the incorporation rate of one of the species, thus inducing a composition strain effect. Undulations observed on the surface were attributed in some cases to transitions from a homogeneous lattice strain to a more periodic inhomogeneous lattice strain, caused by increasing the layer thickness.

Closer views of the two structures from Fig. 4.4(a) are shown in Figs. 4.4(c) and 4.4(d). A line profile taken along line path L1 in Fig. 4.4(c) shows that the rows are separated by $\approx$ 7.8 Å, and that their corrugation heights differ by up to 0.4 Å; along a given row, we measure the distance between two features to be $\approx$ 5 Å. Fig. 4.4(d) shows a similar area to the one on the right in Fig. 4.4(a); taking a line profile along part of this image (line path

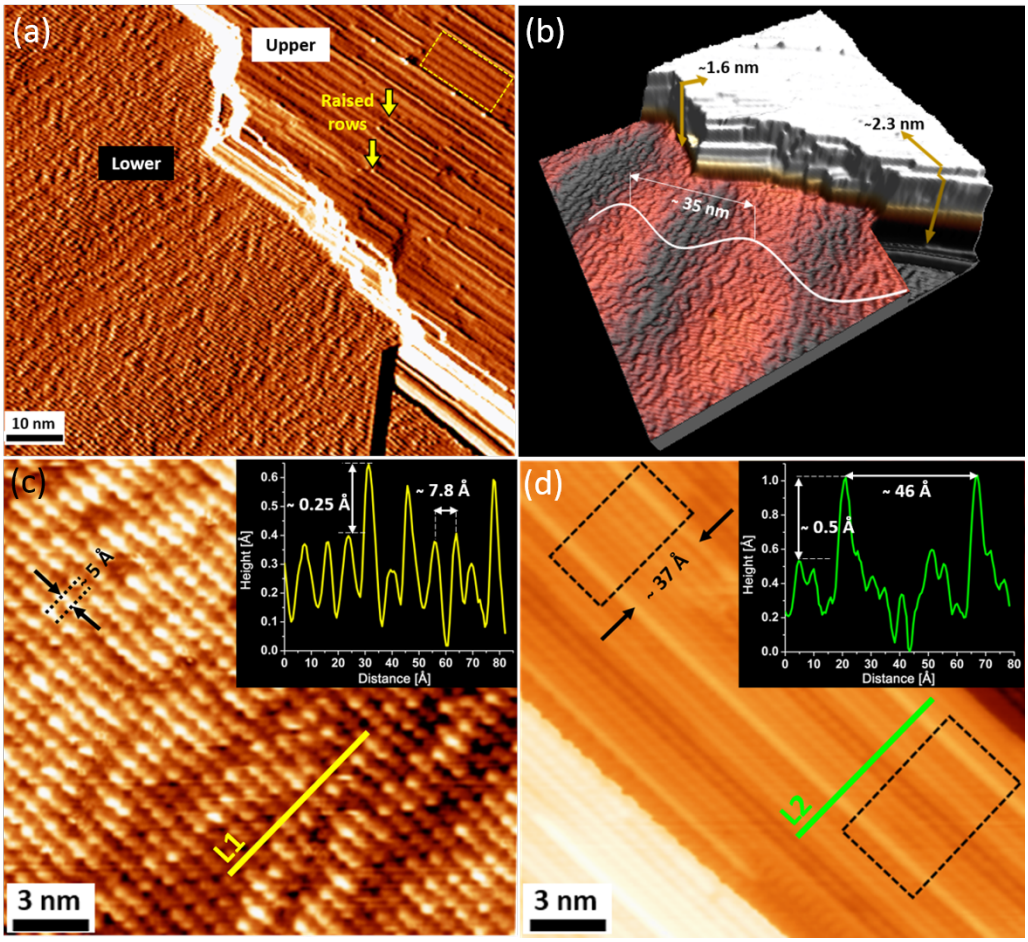

Figure 4.4: (a) Room temperature STM image (shown in derivative mode) taken on sample G; the dashed box encloses a more uniform region found on the upper terrace. (b) 3D perspective view of the area from (a), where a large wavelength modulation is visible on the lower terrace. (c) Closer view at the row structure shown on the lower terrace in (a). (d) Image showing a similar area to the one on the higher terrace from (a); dashed boxes emphasize row structures of different periodicities enclosed by bright raised rows. The insets represent line profiles taken along path lines L1 and L2. Images are acquired at V_S = -100 mV and I_T = 0.1 nA.

L2) shows that in this case also, we have different corrugation heights (which can be as high as 0.65 Å) between rows running parallel to each other. The surface shown in Fig. 4.4(d) is complex, as indicated by the atomic arrangements enclosed by dashed boxes, which are different depending upon the distance separating the raised rows. In addition, measurements

taken on the right terrace in Fig. 4.4(a) reveal relatively random raised-row spacings ranging between ≈ 11 Å and ≈ 68 Å, further suggesting the complexity of these surface structures.

Topographic STM images taken on sample D are shown in Figs. 4.5(a) and 4.5(b). Once again, a raised-row structure is observed, with spacings similar to the ones measured on the surface of Sample G [on the right terrace in Fig. 4.4(a)]. A more uniform structure can be seen in the center of Fig. 4.5(a), with spacings denoted as α and measured to be ≈ 17 Å (see inset). Some of the highest rows on the surface are found to be separated by multiples of α. Comparing Figs. 4.5(a) and 4.5(b), after performing drift correction, it can be observed that similar structures appear on the same sample, only rotated by ≈ 60°. Although all observed phases have an underlying tetragonal unit cell (twofold symmetry), the formation of 60°-rotated domains takes place during growth, given the threefold symmetry of the GaN substrate. In total, three different rotation orientations are seen, also visible in the AFM scans from Fig. 4.3. A similar behaviour was observed previously on the $L1_0$-structured MnGa(111) thin films grown on GaN, described in the previous chapter.

It should be mentioned that the two surface structures that appeared for the more Mn-rich samples (Fig. 4.2) are not observed on the Ga-rich samples. This is consistent with XRD results, which do not show any $L1_0$ MnGa peaks for samples D and E.

Due to the complex surface reconstructions observed in STM, a match with a theoretical model for the proposed Ga-rich phases, Mn_3Ga_5 and Mn_2Ga_5, is very challenging. First, the unit cells of these phases are very large, with 14 atoms per unit cell for Mn_2Ga_5 [46] and 264 atoms per unit cell for Mn_3Ga_5 [75], as shown in Fig. 4.6. Second, as can be observed from XRD measurements the growth takes place along high-index planes for both crystals, which can result in very complex surface arrangements. Moreover, for the case of $L1_0$-MnGa(111), results from the previous chapter showed that not only the surfaces are reconstructed, but the STM images were dominated by Ga atoms. In another study, investigating sub-ML amounts of Mn deposited on GaN(0001), the Mn atoms were found to dominate the surface LDOS in

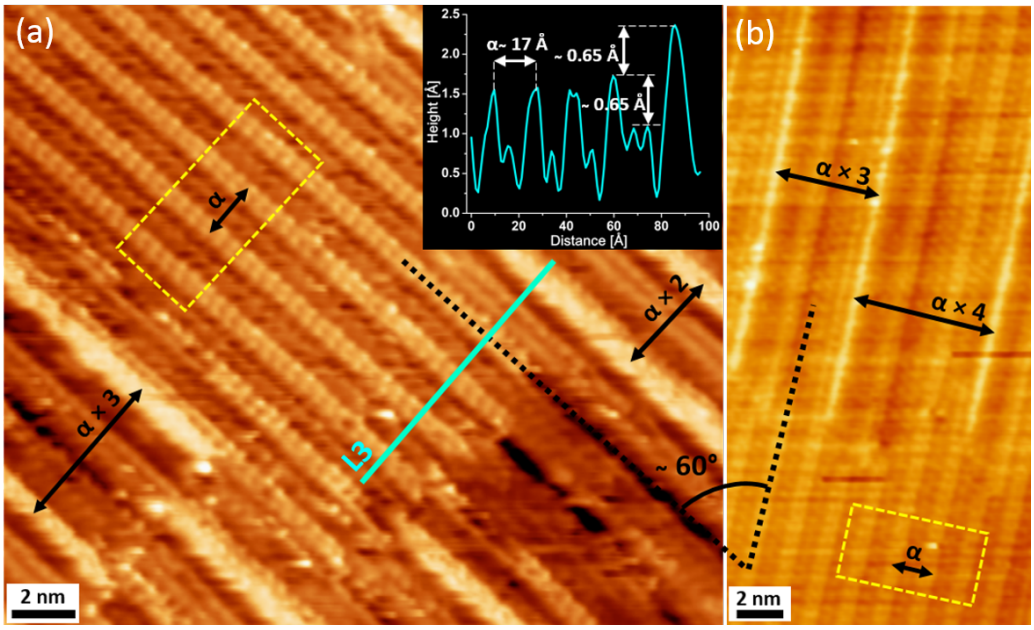

Figure 4.5: (a) and (b) Room temperature STM images of two areas of sample D, showing similarly reconstructed surfaces, only rotated by ≈ 60°; dashed boxes in (a) and (b) enclose uniform row arrangements separated by α, and additional measurements indicate that the raised rows are separated by multiples of α. The inset in (a) represents a line profile taken along line path L3. Both images were acquired at V_S = -130 mV and I_T = 0.1 nA.

the observed $\sqrt{3} \times \sqrt{3}$-R30° MnGa structure.[79] Therefore, it is reasonable to assume that we have similar behavior in the current study, with possibly Mn and/or Ga atoms dominating the surface of different structures, thus complicating the STM image interpretation.

4.3.3 Magnetic properties

Figures 4.7(a) and 4.7(b) show VSM magnetization versus magnetic field loops measured for the thin samples, for magnetic fields oriented parallel and perpendicular to the sample surface. The magnetization values are normalized by the sample volume and parameters extracted from the VSM loops are reported in Table 4.3. Overall, all films exhibit magnetic anisotropy to some degree, as visible from the more square *in-plane* hysteresis

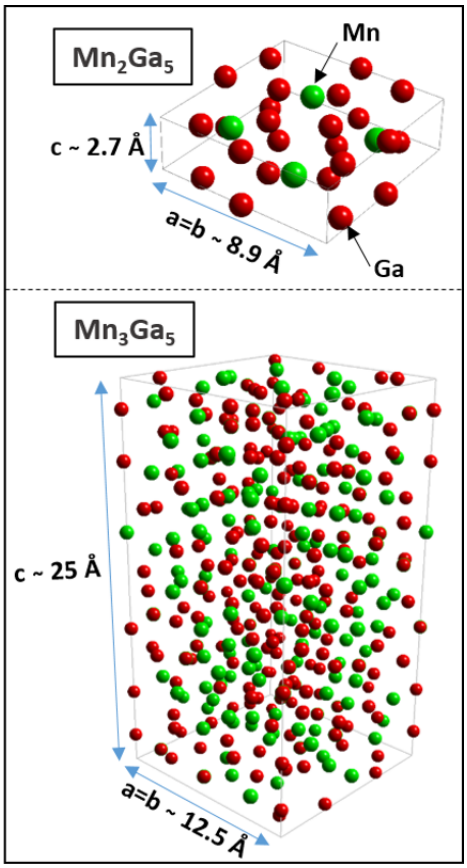

Figure 4.6: Unit cells corresponding to Mn_2Ga_5 (top) and Mn_3Ga_5 (bottom) alloys. The models were constructed using atomic coordinates from reference [46] for Mn_2Ga_5 and reference [75] for Mn_3Ga_5.

loops. Also, we observe a gradual decrease in magnetization as the Ga-concentration increases.

Starting with the more Mn-rich samples (A, B, and C), it can be seen that the highest magnetization (371 emu/cm^3) is obtained for the stoichiometric (Mn:Ga=1) sample A. This value is consistent with previous published results for MnGa films of similar composition grown on GaN(0001) substrates.[4, 52, 62] Reports on $L1_0$ MnGa films deposited on GaAs as well as GaN substrates find that as the Mn content increases the lattice constant *c* decreases. Furthermore, with increasing Mn concentration, a decrease in magnetization, accompanied by an increase in coercivity, is observed. This behavior was explained by the induced strain

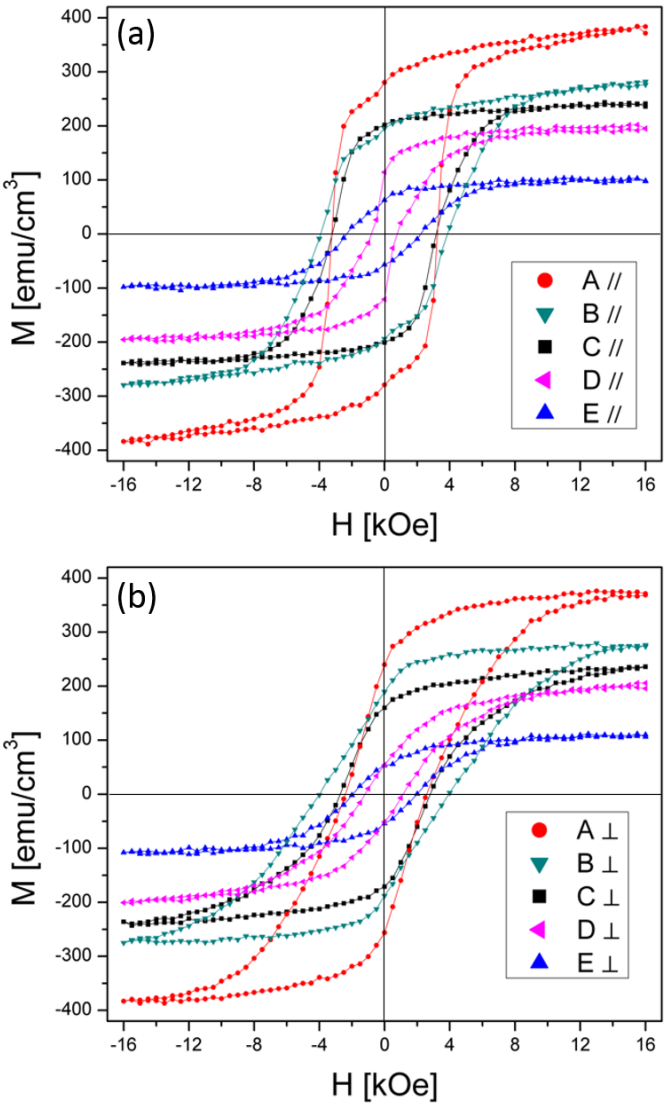

Figure 4.7: Room temperature VSM plots for samples A, B, C, D, and E showing magnetization vs. applied field for a magnetic field oriented parallel (a) and perpendicular (b) to the samples.

in the MnGa lattice.[45, 62, 85] Although we observe a similar tendency for lattice constant c and consequently for the d_{111} spacing [see Fig. 4.1(b)], the trends in magnetization and coercivity are quite different and cannot be easily quantified. As the Ga concentration increases (or Mn concentration decreases), we observe a decrease in magnetization (down to

235 emu/cm^3 for sample C), although not a drastic change in coercivity. In fact, samples A and C have about the same coercive field (3.2 kOe), whereas sample B has the highest value (3.9 kOe). In addition to strain present in the lattice, our films are not purely one phase as determined by XRD. Therefore, we have to take into consideration the appearance of more Ga-rich phases and their effect on the magnetic properties. For example, by looking at Fig. 4.7(a), small kinks in the (*in-plane*) M-H curves for samples A and B are visible, reflecting the interaction between different magnetic phases. The effects of strain and competing magnetic phases cannot be easily separated and can modify not only the magnetization and coercivity, but also the magnetic anisotropy.[45]

Compared to the more Mn-rich films, the M-H curves for samples D and E show smaller magnetization values along with decreased coercivity. A closer look at sample D reveals a stepped hysteresis loop. Both Mn_3Ga_5 and Mn_2Ga_5 (detected by XRD within this sample) are known to be FM and their magnetic interaction can result in loops of this shape, as previously shown for Ga-rich MnGa films deposited onto NaCl substrates.[47, 73] For the most Ga-rich sample E, the loop is more uniform, in agreement with the sharp Mn_2Ga_5 peak (suggestive of mainly one phase) observed in XRD. Comparing samples D and E, we observe that as we increase the Ga-concentration, the magnetization decreases and the coercivity increases.

Magnetic anisotropy is known to be induced by depositing MnGa films on various substrates, as shown by Wang *et al.* [52]; the growth temperature and subsequent thermal treatment also play a role in the resulting magnetic properties.[45, 47] However, all of our films were deposited onto the same substrate, at the same temperature, and no annealing took place after growth. Therefore, the mechanism responsible for tailoring the magnetic properties for the thin films is the change in Mn:Ga ratio during growth.

Another way of tailoring the magnetic properties is by decreasing the thickness of our films. This is clear from the SQUID magnetometry data shown in Figs. 4.8(a) and 4.8(b)

Table 4.3: Saturation magnetization, remnant magnetization, and coercive field values for all MnGa on GaN(0001) films extracted from VSM and SQUID hysteresis loops. The values marked with $^{\perp}$ represent the saturation magnetization for the perpendicular loops.

Sample	M_s [emu/cm^3]	$M_{r\parallel}$ [emu/cm^3]	$H_{c\parallel}$ [kOe]	$M_{r\perp}$ [emu/cm^3]	$H_{c\perp}$ [kOe]
A	371	280	3.2	240	2.4
B	276	196	3.9	190	4.0
C	235	202	3.2	160	2.7
D	195	114	0.8	54	1.2
E	100	63	2.3	53	2.0
F	$1627^{\perp}$	24	0.2	143	0.1
G	$887^{\perp}$	39	0.9	130	0.1

for ultra-thin samples F (more Mn-rich) and G (more Ga-rich). Compared to thicker films of similar composition (samples B and C), the coercivity of sample F drastically decreases for both orientations. For the parallel orientation of sample G, the coercivity (0.9 kOe) is comparable to that of sample D (0.8 kOe) and a similar stepped hysteresis loop is observed.

Unexpectedly, in addition to becoming soft ferromagnets ($H_c \approx 0.1$ kOe for the perpendicular direction), samples F and G exhibit giant PMA; in the parallel orientation not even fields as high as 30 kOe can saturate the samples, whereas fields as small as 9 kOe are enough to saturate the perpendicular direction. Magnetic parameters extracted from SQUID loops are reported in Table 4.3.

Even more unexpected are the giant saturation magnetization values for the perpendicularly magnetized films ($\approx$ 1627 and $\approx$ 887 emu/cm^3 for samples F and G, respectively). Considering an $L1_0$ structure for film F (based on the STM and AES results), we calculate the magnetic moment per Mn atom to be 4.84 $\pm$ 0.52 μ_B, surprisingly large considering the fact that for thicker film B, the calculated moment is only 0.81 $\pm$ 0.12 μ_B.

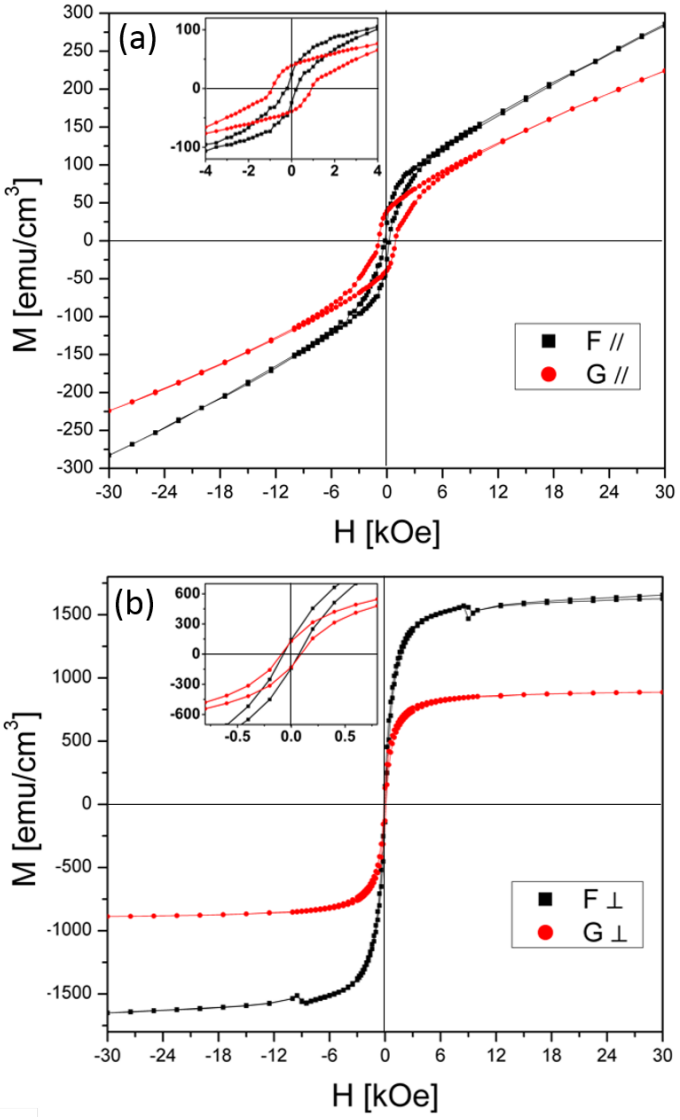

Figure 4.8: (a) and (b) Room temperature SQUID hysteresis loops for samples F and G with magnetic field oriented parallel and perpendicular to the sample surface, respectively; the insets represent closer views at the remnant magnetization and coercivity values.

Combined with the large PMA, it appears that i) most of the Mn 5d-electrons contribute to the magnetization and ii) they are almost fully magnetically aligned perpendicular to the film surface. The mechanism responsible for the increased moment is unclear; surface/interface anisotropy contributions combined with the very small thickness could be a possible cause. However, further investigations are necessary.

Although large PMA is observed in (Mn-rich) $L1_0$- and DO_{22}-structured thicker (≈ 100 nm) MnGa films, in general the coercivities are very large (≈ 5–25 kOe) and the magnetization values are significantly lower (≈ 80–280 emu/cm^3).[56, 60, 61] It is interesting to note that our magnetization and coercivity values for the ultra-thin films are more quantitatively comparable to $L1_0$-structured FePt (M_s ≈ 1000–1250 emu/cm^3 and H_c ≈ 1 kOe) and CoPt (M_s ≈ 800 emu/cm^3 and H_c ≈ 0.2–1 kOe) thin and ultra-thin films prepared under various conditions.[86–89] This comparison is all the more remarkable considering the fact that FePt and CoPt systems are alloys comprised of transition metals, whereas the MnGa system is a Heusler-type alloy. The common denominator for these three systems is the fact that, under certain conditions, they crystallize in the $L1_0$ phase, which is responsible for some of their special magnetic properties.[87]

Although the thicker samples also exhibit anisotropy, it is mostly *in-plane* and not as pronounced as for the ultra-thin samples. For the case of film F, we find the anisotropy field H_a to be 248 ± 8 kOe (this field represents the intersection point between the *in-plane* and *out-of-plane* loops, found by extrapolating the *in-plane* loop). We also calculate the uniaxial magnetic anisotropy constant (which is a measure of the energy required to rotate the magnetic moment along the hard-axis) using K_u=K_{eff}+$2\pi M_s^2$, where K_{eff} is the area between the *in-plane* and *out-of-plane* loops, and $2\pi M_s^2$ gives the shape anisotropy contribution. Thus we find that K_u= 2.19 ± 0.28 × 10^8 erg/cm^3; this value is extremely large, about five to seven times larger than some $L1_0$-structured FePt and CoPt films, and about ten times larger than Mn_xGa films grown on GaAs substrates.[60, 87]

It appears that the giant PMA is induced somewhere between 50 nm and our respective thicknesses for samples F and G; further investigations can look into finding this transition point. We expect that if the observed anisotropy comes from a surface effect, then it should disappear quickly with increasing thickness, similar to the case of Co/Pt multilayers [90]; if the anisotropy comes from bulk, then it should persist to large thicknesses, just as FePt

films. Furthermore, strain present in the ultra-thin films can also affect the anisotropy. Although strain could be responsible for the large PMA in film G (as already discussed, STM imaging reveals such effects), film F does not appear to exhibit strain effects. RHEED measurements on films F (≈ 3.3 nm) and B (≈ 50 nm) do not indicate any *in-plane* lattice constant differences between these two films, which is expected given the fact that $L1_0$ MnGa(111) grows with almost no lattice mismatch on GaN.[4] Therefore, there must be a different mechanism that is responsible for the large PMA in film F. Upon decreasing the sample thickness, interface and surface contributions to the magnetic anisotropy become significant, leading, for example, to changes in the easy magnetization axis from *in-plane* to *out-of-plane*. A combination of all the above effects can play a role in the resulting film properties.

4.4 Conclusions and future directions

In summary, we combined various techniques to study the structural and magnetic properties of Ga-rich MnGa films deposited onto GaN(0001) substrates. Films with compositions ranging from stoichiometric to very Ga-rich and with thicknesses in the range 3.3 nm to 50 nm are investigated. Structurally, as we cross the stoichiometric limit into the Ga-rich regime, we observe that in addition to the expected $L1_0$ phase, more Ga-rich phases develop. Using STM imaging at room temperature, we probe the surface structure and film quality. We find that all films have very smooth and highly reconstructed surfaces. Magnetic investigations show that all MnGa films exhibit ferromagnetism, even the ones pertaining to the very Ga-rich case. In addition, giant PMA is observed as the thickness of the films is reduced to several nanometers, together with an unexpected increase in magnetic moment for the $L1_0$-structured ultra-thin film. We emphasize the importance of surface studies in determining the composition, thickness, and structure for the ultra-thin films, parameters that would be challenging to quantify otherwise.

These new studies on the MnGa system raise a lot of intriguing questions. First, STM surface structure identification would be very useful, especially when trying to understand the new magnetic properties observed for the ultra-thin films. However, theory calculations are necessary in this case, which may not be easily carried out due to the large unit cells of Mn_2Ga_5 and Mn_3Ga_5. Second, it is still a mystery why giant PMA and large magnetic moments are induced as the film thickness decreases. In order to explain and understand these observations, it is necessary to investigate in detail several same-composition samples with varying thickness. Third, all of our films were deposited at $\approx 250^{\circ}$C and none of them were annealed after deposition; therefore, it would be very interesting to see how the morphology, surface structure, and magnetic properties are affected by changing the deposition temperature or by applying post-growth thermal treatment.

5 Interface Formation Between Ferromagnetic Iron and Antiferromagnetic Manganese Nitride Nanopyramids

5.1 Introduction

The importance of iron to the field of thin and ultra-thin films cannot be overstated, and its relevance to modern spintronic material applications is without question. Being *the* canonical ferromagnetic (FM) material, its properties in various material systems continue to be of very high interest till the present day. For example, many recent studies focused on the growth and properties of Fe on topological insulators, 4d transition-metal surfaces, wide band-gap semiconductors, and carbon-based materials such as C_{60} and graphene.[92–97]

Clearly of great importance to any material system is how the Fe grows and couples magnetically to it. This is of fundamental importance to the field of magnetic exchange-bias systems [98, 99], which are ubiquitous in modern magnetic recording technology since the discovery of giant magnetoresistance.[1, 2] Ideally, the FM material, coupled directly to an aFM layer (such as Cr), would form a perfect atomically-sharp interface, and the two magnetic layers would couple directly across the interface. However, studies have shown that the perfect interface model is unrealistic, and the complication in the structural arrangement can lead to complex magnetic arrangements as well.[100, 101] Exploring the manner in which Fe adapts to different aFM surface environments could lead to new insights into this complex behavior and open new pathways to achieving more successful devices as well as fundamental understandings.

In the present study, we choose manganese nitride [$Mn_3N_2(001)$], having a Néel temperature of 652°C (well below the Curie point of Fe, 770°C), as the aFM surface. This surface is well-studied experimentally, including by SP-STM, detailing its structural, electronic, and magnetic properties. Consisting *in the bulk* of two MnN layers followed by one Mn layer with purely *in-plane* aFM spin directions [102], this structure manifests at

the surface a more complex orthogonal, terrace-dependent spin ordering.[5] Such a surface forms an ideal yet challenging testing ground to see the effect of Fe, and as shall be shown, the results are hardly predictable.

The results presented in this chapter were published in Phys. Rev. B **91**, 094433 (2015).[91]

5.2 Methods

5.2.1 Experimental methods

Samples are prepared using MBE by first depositing $Mn_3N_2(001)$ films on MgO(001) substrates. The growth of various phases of manganese nitride, including $Mn_3N_2(001)$, was reported previously by Yang *et al.* [103] First, the MgO(001) substrate is introduced into the growth chamber and annealed at $\approx 1000°C$ for 1 hour under nitrogen plasma. Then, by leaving the plasma active, the temperature of the substrate is decreased to $\approx 450°C$ and the Mn shutter is opened. The Mn to N flux ratio is kept at ≈ 0.39 during growth.[103] [Note: after growth, the sample is imaged using STM to ensure that the $Mn_3N_2(001)$ surface was obtained.] Iron is subsequently deposited at substrate temperatures ranging from RT ($\approx 25°C$) and up to $\approx 200°C$. The Fe flux for all depositions is $6.5 \pm 0.9 \times 10^{13}$ atoms/cm^{2}s and the coverages range between ≈ 0.15 and ≈ 0.41 ML; the samples are *not* annealed after Fe deposition.

Following Fe depositions, the samples are investigated using STM, with differential conductance (dI/dV) maps concurrently acquired with topography images in order to identify the electronic and magnetic properties of our samples. After imaging, AES measurements are conducted in order to obtain surface elemental composition ratios.

5.2.2 Theoretical calculations

First principles total energy calculations are performed under spin-polarized DFT as implemented in the plane waves-self-consistent field code of the Quantum ESPRESSO package.[67] The generalized gradient approximation adopted in a Perdew-Burke-Ernseroff functional is used to treat the exchange-correlation potential.[68] To expand the valence Kohn-Sham states we use a cutoff energy of 30 Ry and Vanderbilt ultra-soft pseudopotentials in order to replace the effect of core electrons.[104] Energetic convergence is achieved when the Hellman-Feynman forces are less than 0.002 Ry/Å. Brillouin zone integration is done using a Monkhorst-Pack smearing of 0.01 Ry and a special $6 \times 6 \times 1$ k-points grid.[105, 106] First, the bulk of Mn_3N_2 is modeled with a body-centered tetragonal structure. After relaxation, an aFM structure is found to be most stable. We also find the lattice parameters to be a=b=2.94 Å and c=11.97 Å, which are in good agreement with previous reports.[107] The Fe adsorption on the surface is analyzed with the surface formation formalism, which is adapted for the Mn_3N_2 system following the work of Qian *et al.* [108]

5.3 Results and discussion

5.3.1 Growth and surface morphology

Presented in Fig. 5.1 are an STM topograph (a) and corresponding dI/dV map (b) of the $Mn_3N_2(001)$ substrate prior to Fe deposition. The surface consists of atomically smooth square-like terraces separated by single atomic height steps, forming a pyramidal morphology. RHEED patterns corresponding to such surfaces and taken along the [100] of Mn_3N_2 right before Fe depositions are shown in Figs. 5.3(a)-(d). Using dI/dV mapping, the electronic structure of the nanopyramids is investigated; at small negative sample bias, the sequence *at the surface* consists of one (B) bright terrace (higher dI/dV signal) followed by two (C and A1) darker terraces (lower dI/dV signal), still having a 3-layer periodicity. As will be shown, all surface layers are MnN layers, with differences between A1, B, and C

coming only in deeper layers. The 3-layer sequence at the surface is consistent with previous electronic studies of the $Mn_3N_2(001)$ surface.[5]

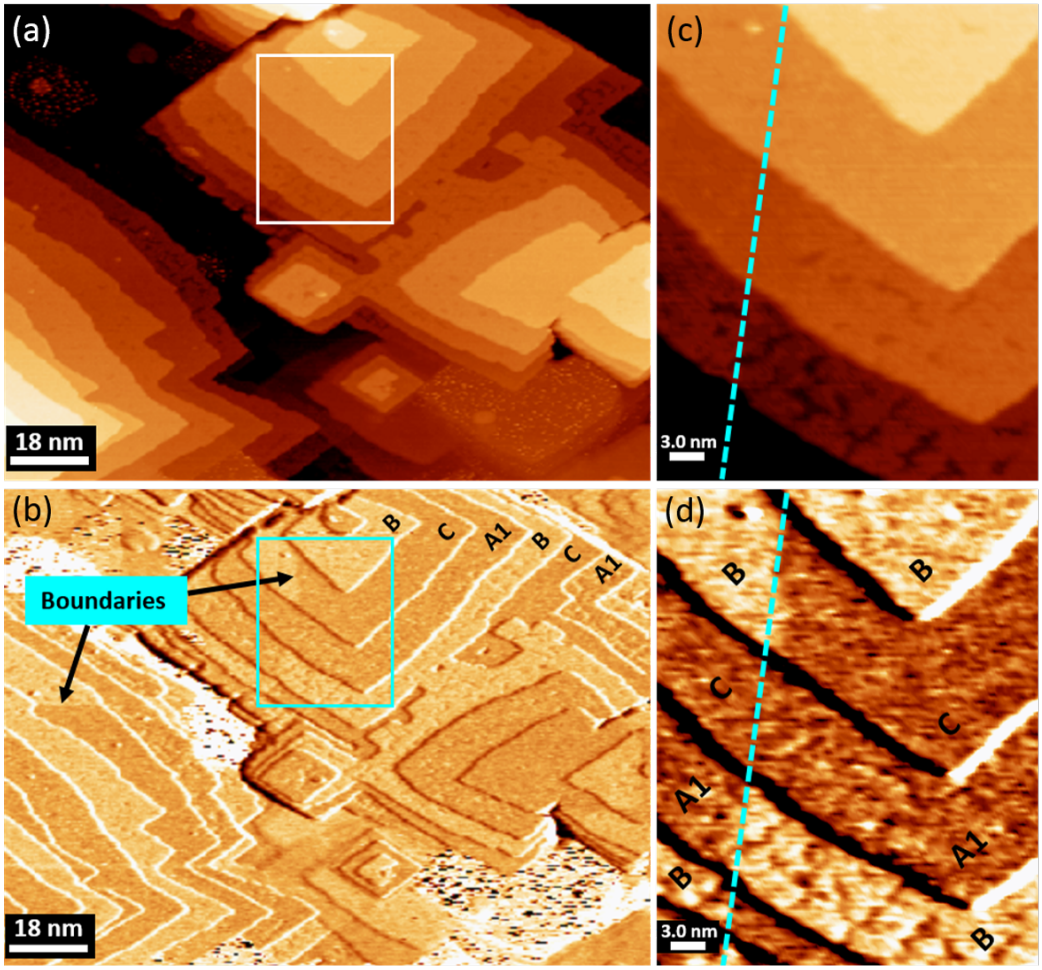

Figure 5.1: (a) STM topograph and (b) corresponding dI/dV map of the $Mn_3N_2(001)$ substrate acquired at V_S = -0.3 V and I_T = 0.1 nA. (c) and (d) represent zoom-in views corresponding to the rectangular boxed areas shown in (a) and (b), respectively. For particular terraces, both B and A1/C terminations are present on the same terrace (with boundaries indicated by dashed lines).

Zoom-in views of the rectangular boxed regions from Figs. 5.1(a) and 5.1(b) are shown in Figs. 5.1(c) and 5.1(d). It can be observed in Fig. 5.1(d) that on a single terrace, both B and A1/C terminations are present, with boundaries indicated by dashed lines. This type

of mixed terrace is commonly seen and is due to stacking faults; although within a terrace these interruptions appear, across multiple terraces the expected sequence is preserved [with occasional exceptions, see e.g. Fig. 5.4(b)].

Figure 5.2 shows STM topographs corresponding to four different growth conditions. Focusing on Fig. 5.2(a), which shows a topographical image of a $Mn_3N_2(001)$ nanopyramid surface after depositing $\approx$ 0.15 ML Fe at a sample temperature of 200 °C), one can see small islands ($\approx$ 1–2 nm in width) having random shapes and decorating all visible terraces. As shown below [inset to Fig. 5.4(a)], their heights are only a single atomic layer. It may also be noticed that there is a clear roughening of the step edges as compared to the bare substrate from Fig. 5.1(a), indicating a possible reaction of the Fe with the substrate. For a higher coverage of $\approx$ 0.36 ML Fe [Fig. 5.2(c)], one sees more expanded island shapes as well as even more step edge roughening; sharp terrace corners are no longer visible. The deposition amount quoted in the insets from Fig. 5.2 is an estimate based on the atomic flux monitor calibration and the STM measured island coverage; the coverages measured from STM are determined by averaging over multiple images of the same sample.

The RHEED patterns recorded after Fe depositions [see Figs. 5.3(e)-(h)] show no change in the lattice constant and no additional phases, implying that the islands are coherent with the substrate; these observations are also valid for the [110] crystallographic directions of Mn_3N_2 (not shown).

Figs. 5.4(a) and 5.4(b) show an STM topograph and corresponding dI/dV map, respectively, for the 0.15 ML case. The island heights are all about the same (2.28 ± 0.13 Å), as seen in the line profile shown in the inset to Fig. 5.4(a). The measured step heights and electronic contrasts between adjacent pairs of terraces (A1-B, B-C, and C-A1) are consistent with the surface before Fe deposition (shown above in Fig. 5.1) and also with previously published results[5], showing that the terrace electronic properties are unaffected by the islands. One unique feature of this surface region is the presence of a stacking fault

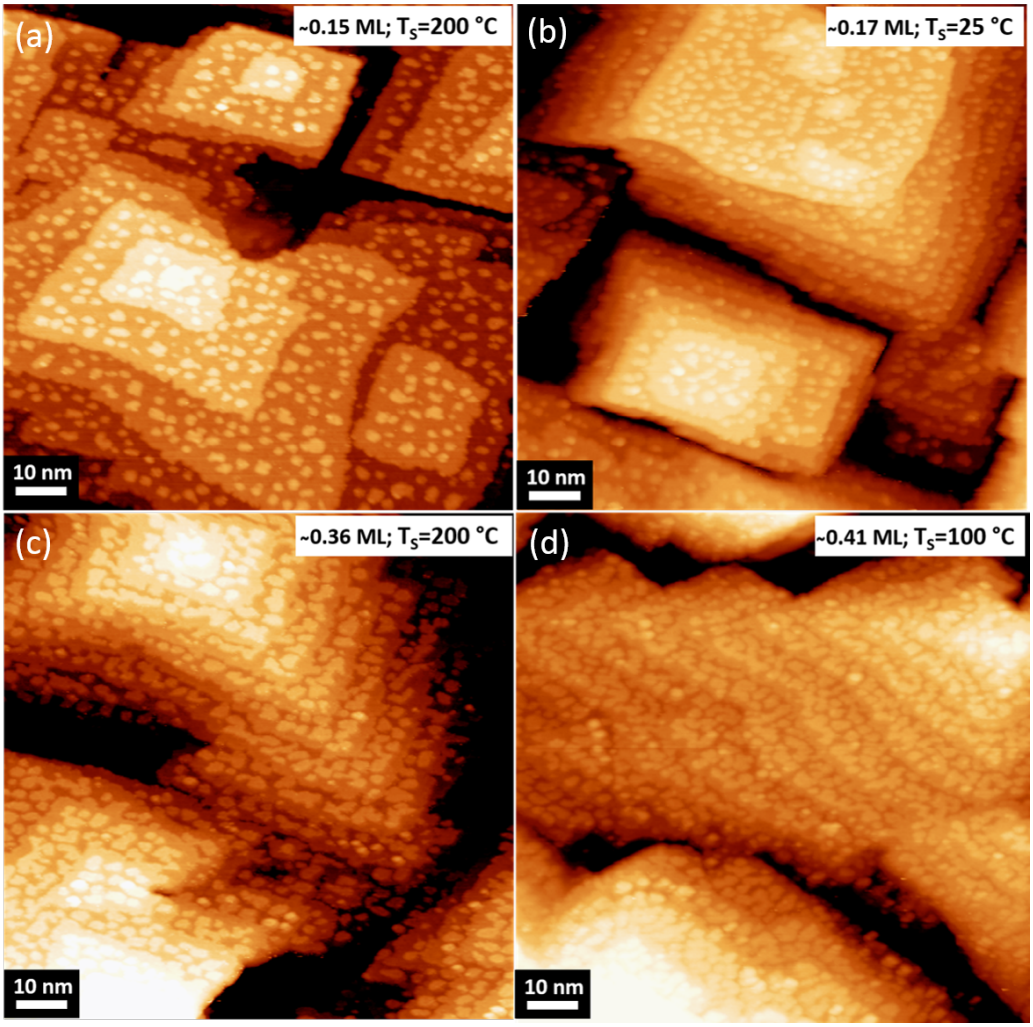

Figure 5.2: STM topographs for four different island coverages and corresponding substrate temperatures during growth. Scanning parameters for all samples: V_S = -0.7 V and I_T = 0.1 nA.

boundary within one of the terraces, as indicated by a dashed line; this boundary has to be taken into account when interpreting the dI/dV contrast on the islands from differing terraces presented in Fig. 5.4(c) (discussed below).

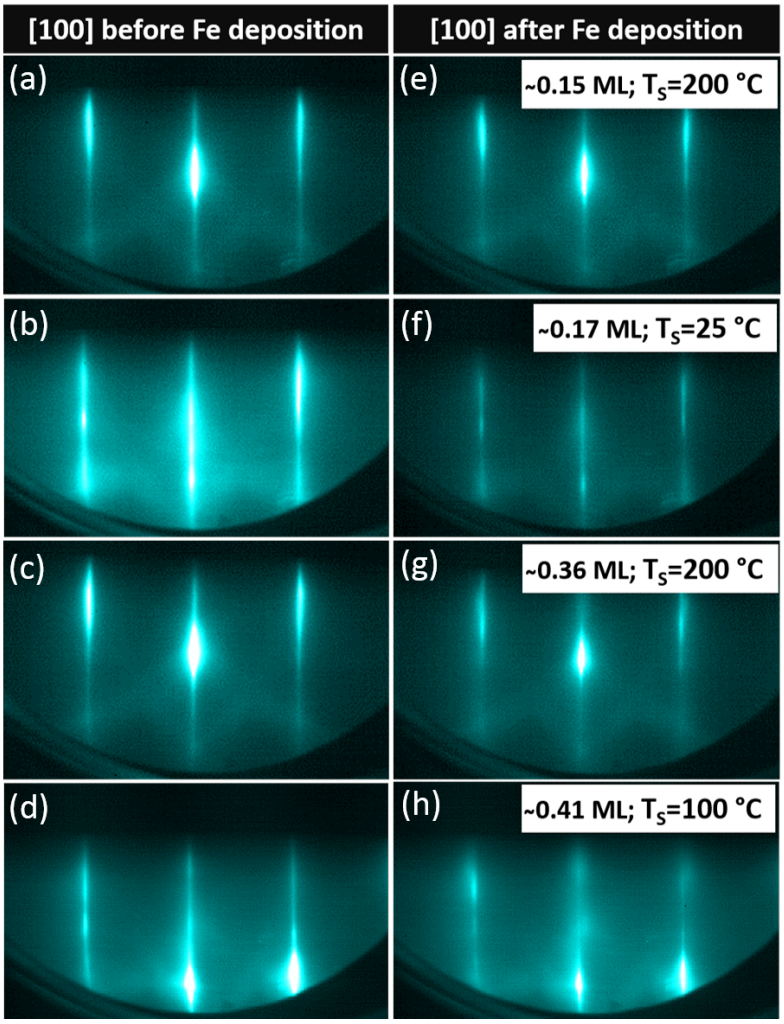

Figure 5.3: RHEED patterns recorded along the [100] direction of Mn_3N_2 before (a)-(d) and after (e)-(h) Fe depositions.

5.3.2 Surface composition and structural models

An important question that cannot be answered by examining the STM images alone refers to the composition of the observed islands. We performed AES measurements in order to obtain the surface elemental compositions, by measuring AES peak intensities obtained from derivative spectra with corrections for Fe and Mn sensitivity factors. Surprisingly, we find Fe:Mn ratios of only a few percent (see the last column in Table 5.1).

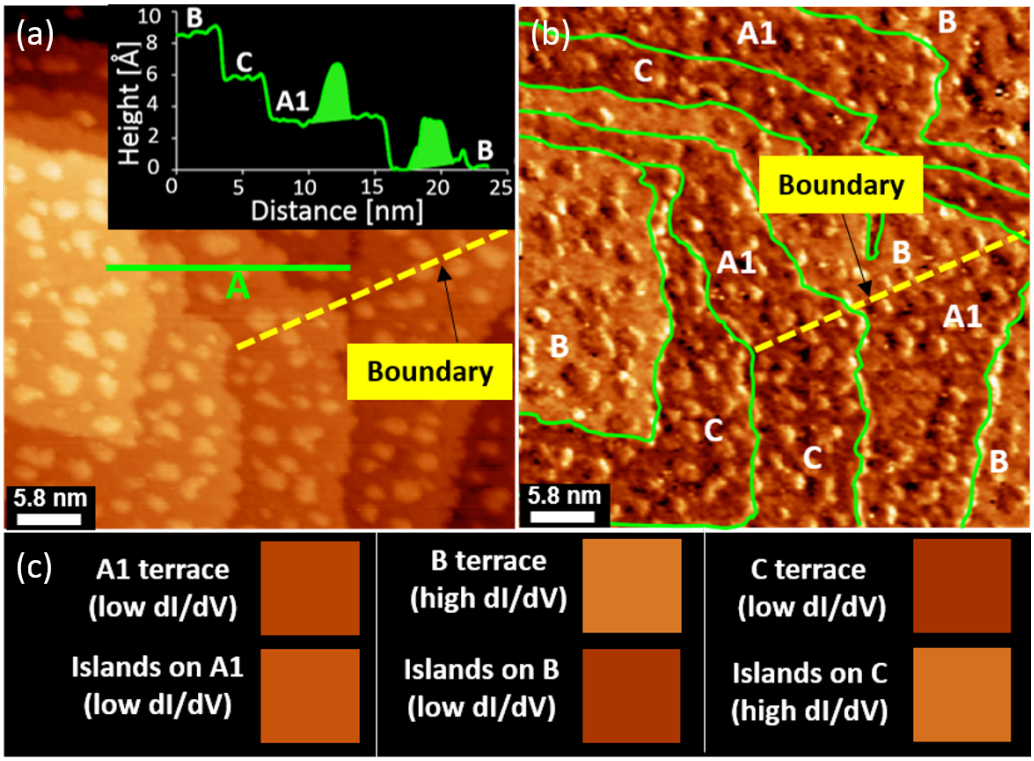

Figure 5.4: (a) STM topograph and (b) corresponding dI/dV map for the 0.15 ML case (V_S = -0.3 V; I_T = 0.1 nA). The inset in (a) is a line profile taken along path A. (c) Contrast map from (b) showing the electronic contrast differences between islands and corresponding substrate terraces.

To know whether or not such values are consistent with Fe atoms at the surface, it is necessary to model the AES Fe:Mn ratios. Since this requires some models for the stacking sequences of Mn and MnN layers, we turn to theoretical calculations. Beginning with just the $Mn_3N_2(001)$ substrate, Fig. 5.5(a) shows a partial atomic model (with 4 terraces) of a manganese nitride nanopyramid. Three different models (as indicated within dashed boxes), corresponding to the three unique terraces seen in the STM images, are presented: 1) model A1, consisting of MnN-Mn-MnN-Mn-MnN... [an inversion of the expected layer sequence Mn-MnN-MnN-Mn-MnN... within the top two layers (model A - not shown)]; 2) model B, consisting of MnN-MnN-Mn-MnN-MnN...; and 3) model C, consisting of

Table 5.1: Island coverages, estimated AES Fe:Mn ratios for the case of Fe islands only, Mn islands only (with Fe in deeper layers) on the surface, and measured Fe:Mn AES ratios.

Coverage (ML)	Case of Fe islands (%)	Case of Mn islands (%)	Measured (%)
0.15 ± 0.02	6.38 ± 0.32	2.27 ± 0.61	2.16 ± 0.75
0.17 ± 0.01	7.29 ± 0.36	2.50 ± 0.67	2.84 ± 0.44
0.36 ± 0.04	16.82 ± 0.84	5.09 ± 1.40	5.17 ± 0.37
0.41 ± 0.02	19.62 ± 0.98	5.67 ± 1.60	5.71 ± 0.58

MnN-Mn-MnN-MnN-Mn..., which has the identical layer sequence as model A1 only within the first three layers.

In terms of surface energy, the presented three models are all lowest energy over a particular range of chemical potential (see Fig. 5.6). First and surprisingly, the calculations show that the inverted A1 model is energetically much more favorable than model A over the entire range of chemical potential. Model C becomes more favorable than model A1 at less Mn rich conditions at about 1 eV, and model B becomes most favorable at even less Mn rich conditions at about -0.2 eV. Further details on the bare $Mn_3N_2(001)$ surface were published separately by our collaborators.[109]

The AES ratio is then modeled by taking into account the contributions from the islands as consisting only of Fe and the underneath layers being MnN and/or Mn (with their successive contributions to the AES signal exponentially diminishing). Since the AES signal reflects an average of a large area of the surface covering many nanopyramids, we also take an average of the three different possible stacking sequences A1, B, and C, all of which are observed by STM on the same sample. In this manner, for the 0.41 ML coverage case we estimate an Fe:Mn ratio of $\approx$ 19.62 %, whereas we only measure $\approx$ 5.71 %. The same trend is obtained for all the coverage cases (see Table 5.1). This disagreement indicates that the islands are not (or not entirely) made of Fe atoms.

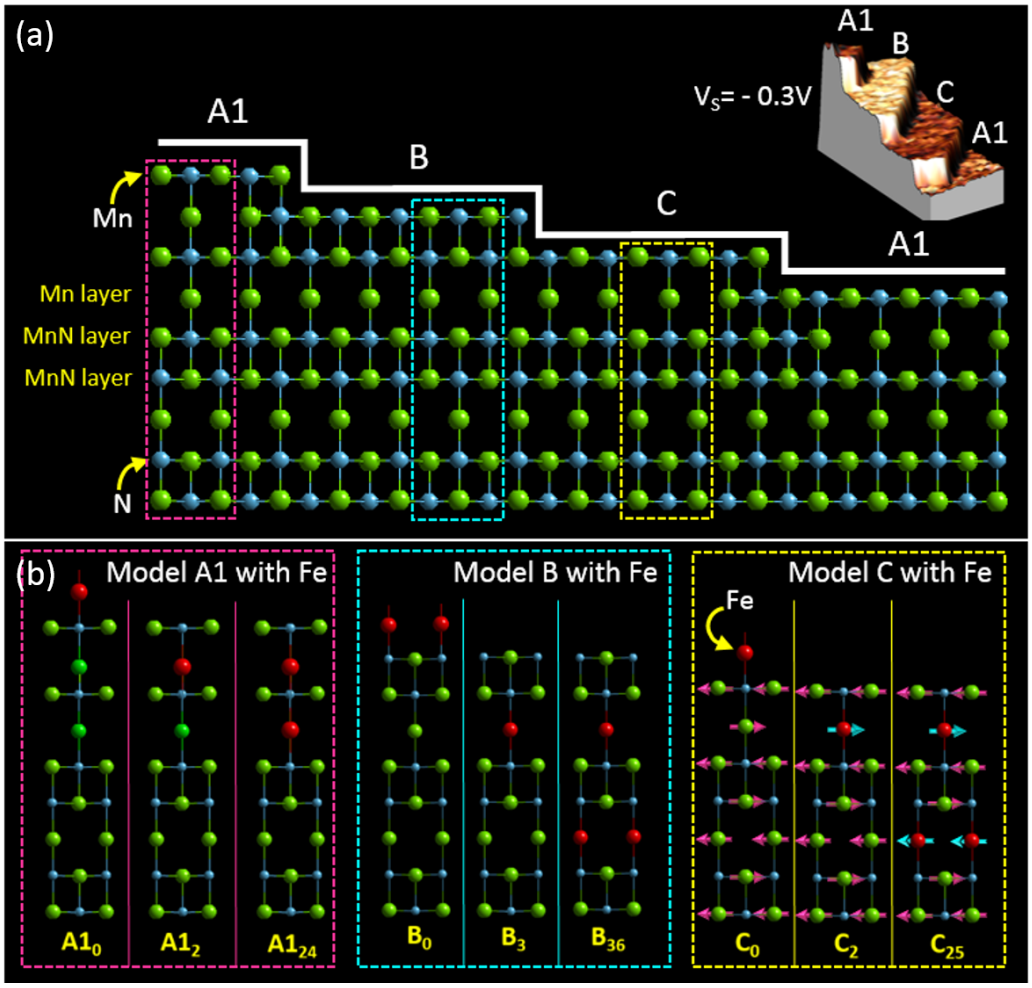

Figure 5.5: (a) Atomic model of $Mn_3N_2(001)$ nanopyramids in which three different types of terraces can be observed: A1, B, and C; the inset represents a 3D-rendered STM image of part of one pyramid to show the correspondence with the actual model. (b) Atomic models for A1, B and C terraces with Fe atoms (in red) at different locations. In addition, the panel for model C shows the magnetization directions of different layers. Differently colored arrows on the Fe and Mn atoms indicate the different magnetic moments.

Therefore, we consider the possibility that the Fe atoms react somehow with the $Mn_3N_2(001)$ surface, perhaps incorporating into the top few surface layers, which could lead to islands having a different composition. In order to identify possible locations for Fe atoms within the $Mn_3N_2(001)$ structure, Fe is introduced, and Fig. 5.5(b) shows the A1, B, and C models each with three model variations in which Fe occupies different site

locations (including on top and within the $Mn_3N_2(001)$ structure). Each model is denoted via subscripts referring to the layers in which Fe atoms are located. We find that Fe atoms do not occupy Mn sites within MnN layers since this is energetically unfavorable. Instead, Fe atoms are found to favorably occupy Mn sites within the Mn layers, and doing this even results in an overall lowering of the total surface energies at the N-rich side, as can be seen in Fig. 5.6 where models B_3 and B_{36} become more favorable than model B. Importantly, the results show that it is highly unfavorable for Fe atoms to be at the surface as models $A1_0$, B_0, and C_0 are very high in energy. But placing Fe into successive sub-surface Mn layers continually lowers the energy, first for models $A1_2$, B_3, and C_2 and then for models $A1_{24}$, B_{36}, and C_{25}. Iron atoms in more than one layer are better than in only one layer.

Naturally, the Fe atom incorporation leads to Mn atom replacement and subsequent removal of Mn from sub-surface layers. We therefore propose that the observed islands are formed from the ejected Mn. In order to confirm this picture, we once again carried out AES Fe:Mn ratio simulations, placing Fe atoms into lowest energy configurations ($A1_{24}$, B_{36}, and C_{25}). Taking an average of the simulated ratios based on the three possible configurations results in estimates, for the various Fe depositions, which are in excellent agreement with the measured AES Fe:Mn ratios (see Table 5.1).

Possible incorporation pathways for Fe atoms are: 1) at the step edges (indicative of this is the roughening observed after Fe deposition - see Fig. 5.4); 2) through direct exchange with surface Mn atoms; and 3) through the defects that are present on the terraces (as also observed in Fig. 5.1). Since we observe islands on all terraces (including the very top ones) we have to consider possibilities in which the ejected Mn atoms can migrate up and/or down the terrace steps, and maybe even up through the defect sites. Of course this behavior is only speculative, and theoretical calculations would be necessary to clarify these dynamical processes that lead to island formation.

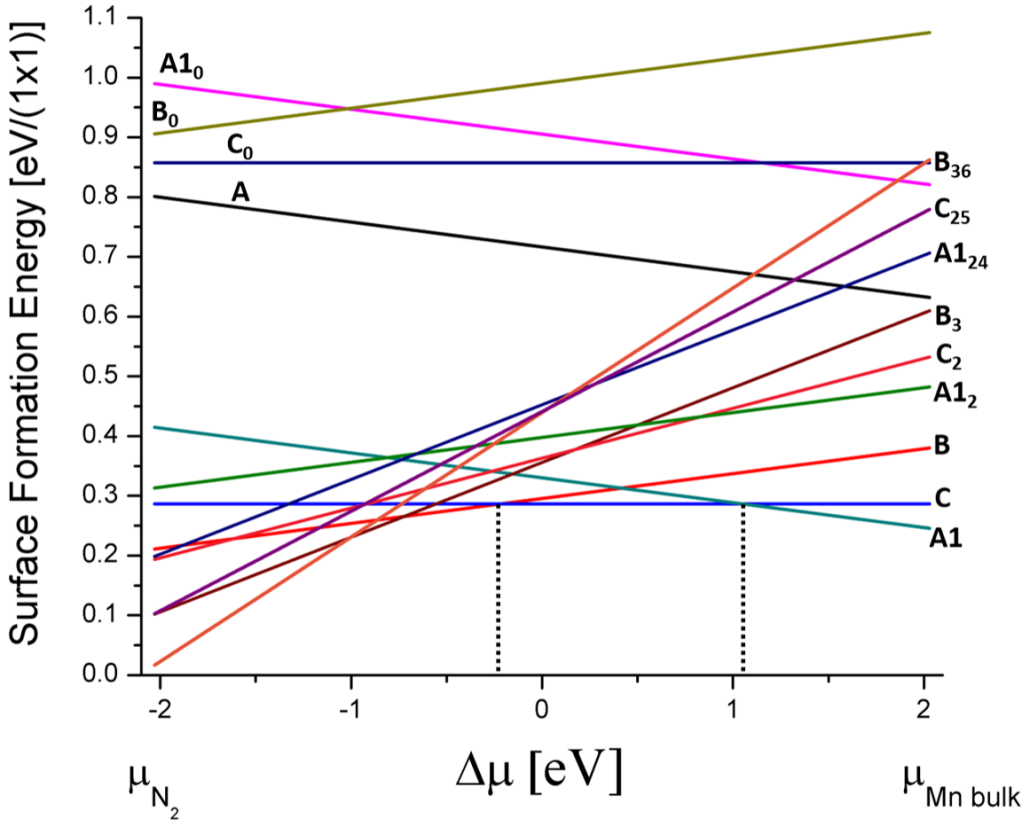

Figure 5.6: Surface formation energy plots versus chemical potential for the models shown in Fig. 5.5.

Referring back to Figs. 5.4(b) and 5.4(c), the electronic contrast of the islands from differing terraces can now be discussed in terms of Mn islands residing on top of $A1_{24}$-, B_{36}-, and C_{25}-structured surfaces. We consistently find not less than three different island contrasts, dependent only on the island's terrace. As shown in Fig. 5.4(c), we observe dark islands on bright (B) terraces, light islands on dark (C) terraces, and dark islands on dark (A1) terraces. Due to the stacking fault (indicated by the dashed line), which results in a sequence of three low dI/dV (dark) terraces, the middle one contains two types of island contrasts, dark on dark above the A1 region and light on dark above the C region. Although the data was acquired using an Fe-coated W tip, the contrast observed here is purely electronic based on 1) a lack of expected magnetic contrast on the terraces themselves;[5] and 2) the fact that an

applied *out-of-plane* magnetic field of ≈ 0.4 T did not result in any changes to the islands dI/dV contrasts.

Having established three dI/dV electronic contrasts for the islands, we note that this is exactly consistent with the 3-layer periodicity of the $Mn_3N_2(001)$ structure. In fact, the islands' contrasts are consistent with a continuation of the same chemical sequence as for the $Mn_3N_2(001)$ itself. This may indicate that either 1) the electronic properties are determined largely by the Mn atoms; or 2) some islands may contain N, a possibility not entirely unexpected based on the theoretical finding (as well as on the actual growth procedure) that all terraces (first layers) consist of MnN. Atomic rearrangements at the surface could result in N atom exchanges (Note: surface N content does not affect the Fe:Mn ratios).

As further proof of the chemical nature and electronic properties of the islands, we carried out additional experiments, depositing Mn onto $Mn_3N_2(001)$ nanopyramids. Figures 5.7 and 5.8 show dI/dV maps after Mn depositions. In Fig. 5.7, acquired at V_S = -0.3 V, we observe the same contrast as in Fig. 5.4 with terraces A1 and C being electronically equivalent at this bias, and with corresponding islands having different contrasts. In Fig. 5.8, which was acquired at V_S = -0.7 V, one can observe that although layers A1 and C are slightly different electronically, the islands' contrasts follow, just as in the case of Fe-induced islands, the 3-layer periodicity of the substrate. For the case of Mn depositions, the different island shapes are most likely the consequence of a different diffusion mechanism responsible for island formation, compared to the case of Fe-induced islands. Nevertheless, this fact did not alter the observed electronic contrast.

5.3.3 Predicted magnetic alignment

After having determined the locations of the Fe atoms within the $Mn_3N_2(001)$ nanopyramids, theory calculations also find the magnetic moment directions and values for the Fe_{Mn} substitutions. Interestingly, the Fe atoms adopt the same magnetization directions

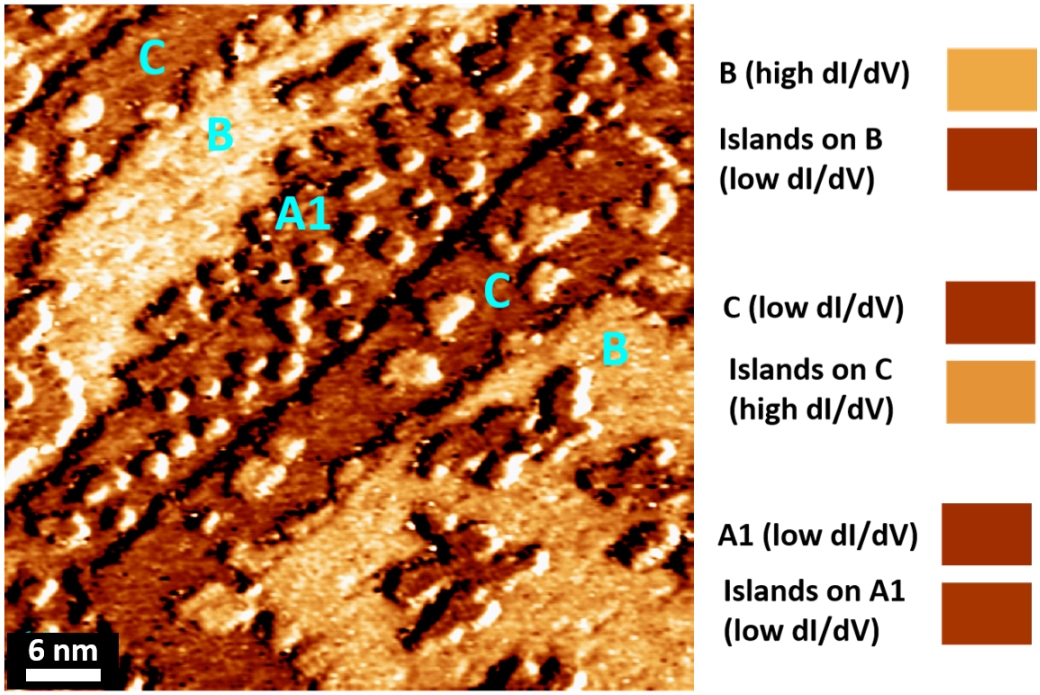

Figure 5.7: dI/dV map after Mn deposition on $Mn_3N_2(001)$ and corresponding contrast maps showing the differences between terraces and islands, for V_S = -0.3 V and I_T = 0.1 nA.

as for the replaced Mn atoms, i.e. Fe atoms couple ferromagnetically with atoms within the same layer [other Fe atoms (Fe-Fe coupling) and/or not yet substituted Mn atoms (Fe-Mn coupling)] and antiferromagnetically with adjacent layers [as depicted in the panel for model C from Fig. 5.5(b)]. These results are valid for all three models (A1, B, and C).

For the specific case of the lowest energy models ($A1_{24}$, B_{36}, and C_{25}), compared to a 0.00 eV/[Fe-Fe(Mn) pair] energy value for Fe-Fe and Fe-Mn FM coupling within the same layer, the aFM coupling is far less favorable, with values ranging from 0.35–0.77 eV/(Fe-Fe pair) for Fe-Fe, and 0.32–0.72 eV/(Fe-Mn pair) for Fe-Mn. The actual magnetic moment values for the Fe_{Mn} substitutions range from 2.50–2.68 μ_B while the Mn atoms in the same sites had magnetic moments ranging from 3.21–3.43 μ_B. Further details regarding the magnetic coupling between Fe and $Mn_3N_2(001)$ were published separately by our theory collaborators.[110]

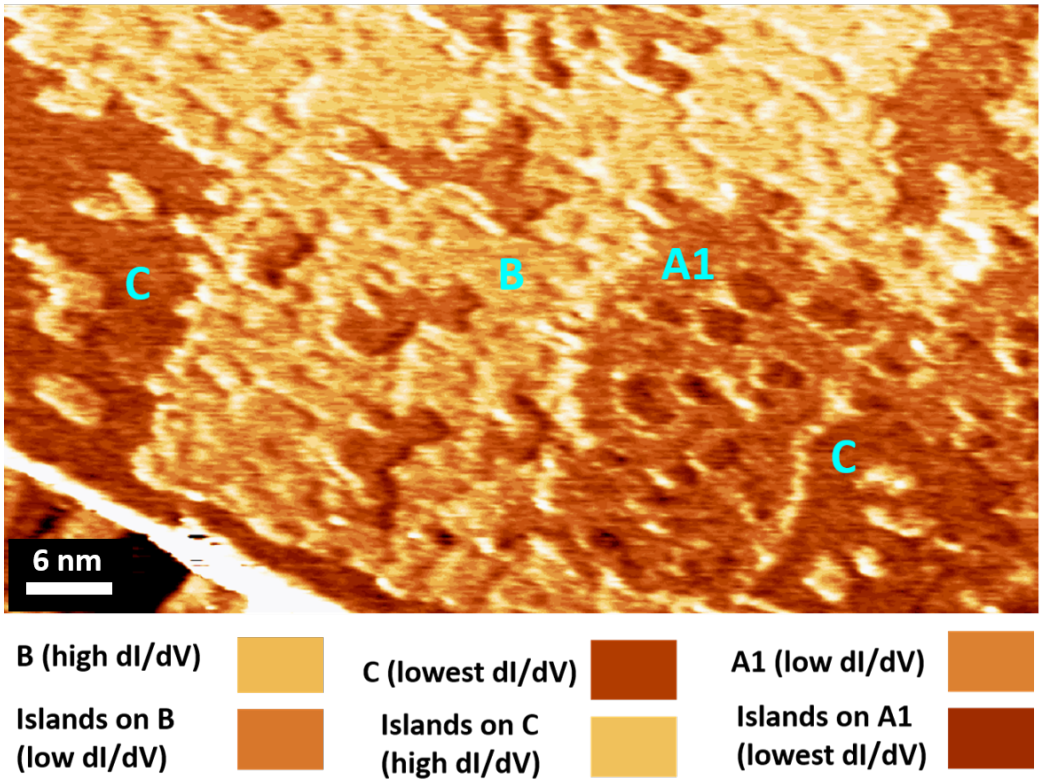

Figure 5.8: dI/dV map after Mn deposition on $Mn_3N_2(001)$ and corresponding contrast maps showing the differences between terraces and islands, for V_S = -0.7 V and I_T = 0.1 nA.

5.4 Conclusions and future directions

In conclusion, we find that the simple deposition of Fe onto $Mn_3N_2(001)$ results in the unexpected substitution of Fe for Mn within Mn layers and the formation of Mn (possibly MnN) islands on top. While the islands take on an electronic character consistent with a simple continuation of the normal 3-layer chemical periodicity of $Mn_3N_2(001)$, the Fe atoms take on the magnetic character of the substituted sites. Extending beyond this study to the formation of a possible Fe/$Mn_3N_2(001)$ exchange-biased system, such a complex interfacial structure as we find here would undoubtedly play a very important role in the overall magnetic behavior. It is furthermore very likely that similar behavior to that shown here will occur in other aFM/FM systems, necessitating similar investigations.

It would be desirable to obtain experimental evidence for the magnetic character of the substituted Mn sites within the sample. Future studies using magnetic dichroism could potentially address this point; however, such experiments are highly non-trivial due to the high Néel point of Mn_3N_2.

For the case of Mn depositions onto $Mn_3N_2(001)$, a future study can explore in detail the electronic and magnetic properties of the resulting Mn islands. Along the same lines, one could also try depositing sub-ML amounts of other elements onto this surface. For example, our theory collaborators performed some initial calculations for Ga atoms coupled with $Mn_3N_2(001)$. It appears that Ga atoms prefer residing on the surface, contrary to the case of Fe. It was previously found that by depositing sub-ML amounts of Mn on top of semiconducting GaN(0001) and GaN(000$\overline{1}$) surfaces, structures with different magnetic properties are induced.[79, 111] Essentially we are dealing with the same three elements Mn, Ga and N, only combined in different structures; therefore, we expect that by depositing Ga on $Mn_3N_2(001)$ surfaces interesting properties will result.

6 Structural and Magnetic Properties of Magnetostrictive Iron Gallium Thin Films

6.1 Introduction

Extending the previous study of only Fe depositions onto aFM manganese nitride substrates, we have combined Fe with Ga to study highly magnetostrictive FeGa (or Galfenol) alloys. It has been previously found that incorporating small amounts of Ga within the body-centered cubic Fe matrix results in about a ten-fold increase in the MS value as compared to that of pure Fe (which is $\approx$ 20 ppm). This ability of changing its shape due to magnetization changes, combined with good mechanical properties and weak temperature dependence of the MS, makes FeGa very attractive for the sensor and actuator industry.[112–114]

The FeGa system has been extensively studied in bulk single-crystal form, finding that the MS is dependent on the heat treatment (e.g. cooling rate) and also on the Ga concentration in the structure, with a first peak ($\approx$ 375 ppm) at about 19 at.% Ga.[113, 115–120] *[Note: what is meant by bulk single crystal form is a single crystal grown by bulk methods; this terminology will be used throughout this chapter].* Since strain and magnetism are strongly coupled in this system, FeGa in the form of thin films deposited onto various substrates could have their magnetic properties altered, making this alloy very intriguing. Studies of sputtered and MBE-grown FeGa films onto non-magnetic substrates such as MgO(001), GaAs(001), and ZnSe/GaAs(001) focused on their magnetism as a function of composition and thermal treatment.[121–132] For the case of FeGa films grown on SC ZnSe/GaAs(001), the observed tetragonal distortions from the ideal cubic bulk lattice were attributed to the composition-dependent arrangement of Ga atoms within the structure. Such changes were found to be responsible for new magnetic properties, such as large PMA, as compared to films grown on MgO(001) substrates.[124, 126, 128, 131] The ultimate goal

in the field of FeGa thin films is to link their magnetostrictive properties with the observed magnetic anisotropies.

Motivated by all these interesting observations, we focus on FeGa thin films deposited onto aFM manganese nitride and non-magnetic MgO(001) substrates. With the initial stages of Fe (or FeGa with 0 at.% Ga) depositions onto Mn_3N_2(001) established, we also choose aFM MnN(001) [or the θ phase of the manganese nitride system] for FeGa depositions. Bringing in the magnetic component of the substrate could give rise to some new magnetic properties in the FeGa system as compared to growth on non-magnetic substrates. Since the surface morphology could also impact the film properties, we add a new perspective on these films by studying their surfaces with STM. Similar to the studies of Ga-rich MnGa (presented in Chapter 4), we combine surface studies with *ex-situ* structural, compositional, and magnetic characterizations. The main questions that this study addresses are: What are suitable growth parameters? How is the film quality? How do the magnetic properties change with composition and starting substrate? Do we have new magnetic properties?

6.2 Methods

The $Fe_{1-x}Ga_x$ films are grown by MBE onto three different substrates: non-magnetic MgO(001), aFM Mn_3N_2(001), and aFM MnN(001), the latter having a slightly different *in-plane* lattice constant compared to that of Mn_3N_2(001). MgO(001) is also used as starting substrate for the manganese nitride samples. During Mn_3N_2(001) growth, as already described in Chapter 5, the Mn to N flux ratio is kept at ≈ 0.39; to obtain a MnN(001) film, the Mn to N flux ratio is kept at ≈ 0.24 during growth.[103] The Fe to Ga flux ratios are varied such that samples with compositions x between ≈ 8 at.% Ga and ≈ 24 at.% Ga are obtained. The sample temperature during growth was slightly varied between different samples, with values ranging from ≈ 320°C and ≈ 420°C. Following preparation, the samples are investigated with STM.

Ex-situ measurements are also performed; AFM and MFM are used to probe the large scale morphology and the magnetic domain structure of our films, respectively. The growth orientation and film composition are found by XRD and RBS, respectively. Using VSM, the bulk magnetic properties are determined for two different *in-plane* orientations of the applied field, at angles of 0° and 45°, corresponding to two different crystallographic directions.

6.3 Results and discussion

6.3.1 Growth, composition, and structure

Figure 6.1 shows the RHEED patterns for all six FeGa films, together with those of the starting substrates. The substrate type and growth temperature of each sample are indicated in Table 6.1. We infer from the RHEED patterns that all FeGa films grow with a 45° *in-plane* rotation with respect to their corresponding substrate. Combined with XRD results (discussed below) we find the following epitaxial relationships: FeGa(001) || MgO(001), FeGa[110] || MgO[100], FeGa(001) || MnN(001), FeGa[110] || MnN[100], FeGa(001) || Mn_3N_2(001), and FeGa[110] || Mn_3N_2[100].

Using RBS, the composition of the FeGa films is determined to range between ≈ 7.9 at.% Ga and ≈ 23.6 at.% Ga, with four samples having around 15 at.% Ga in their structure (see Table 6.1).

Referring to samples 822, 823, and 826, all grown on MgO(001) substrates, the FeGa RHEED patterns are streaky, consistent with high-quality epitaxial growth. Faint 2 × streaks are observed for samples 822 (≈ 7.9 at.% Ga) and 823 (≈ 15.2 at.% Ga), indicating the formation of a 2 × 2 surface reconstruction. This is not the case for sample 826 (≈ 15.2 at.% Ga); it is possible that the higher growth temperature (see Table 6.1) prevented the formation of a surface reconstruction.

By looking at the samples grown onto aFM substrates, namely 824, 825, and 828, the spotty pattern for sample 828 (≈ 15.3 at.% Ga) is an indication of rougher surfaces. A

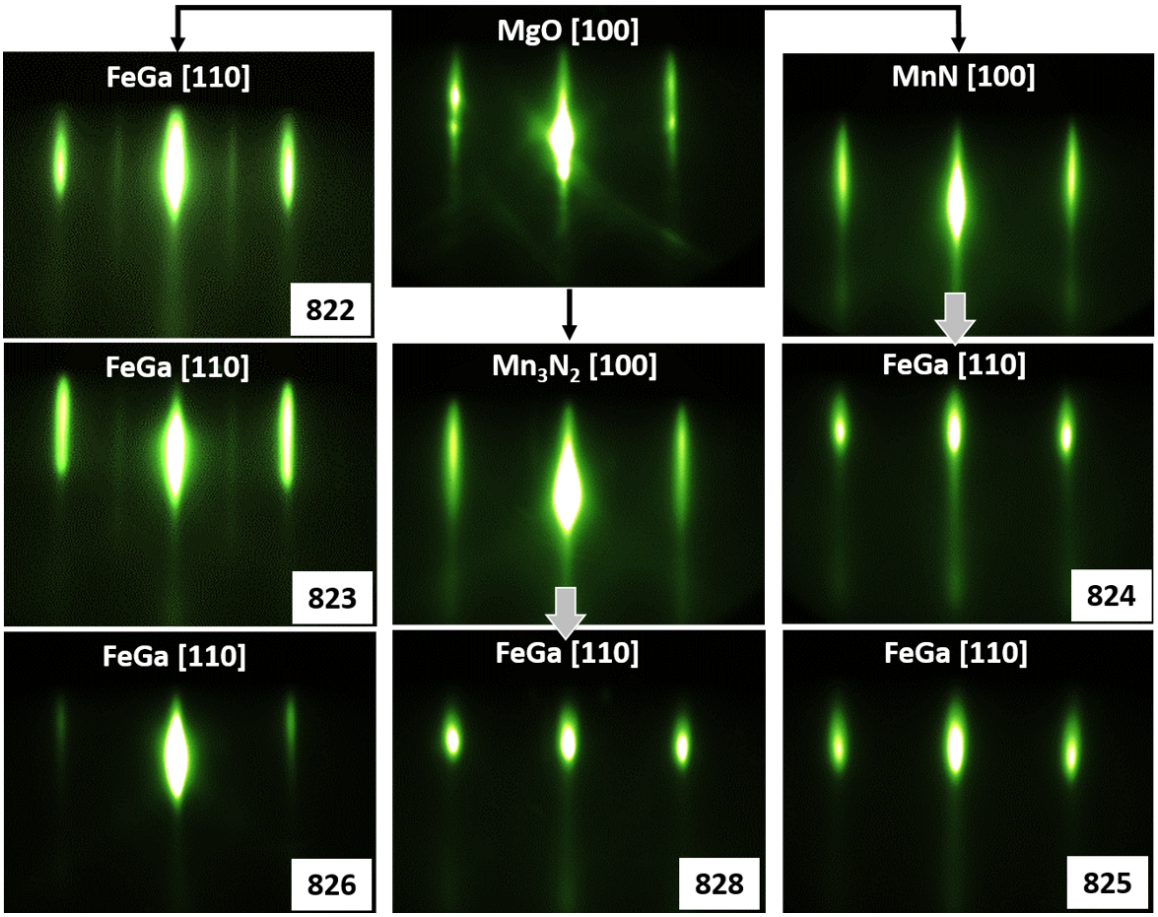

Figure 6.1: RHEED patterns for FeGa films deposited onto MgO(001) [822, 823, and 826], Mn_3N_2(001)/MgO(001) [828], and MnN(001)/MgO(001) [824 and 825] substrates. The FeGa films grow with a 45° *in-plane* rotation with respect to their corresponding substrates.

slightly more streaky pattern is observed for sample 825 (≈ 15.7 at.% Ga), and a further improvement of the RHEED streaks can be seen for sample 824 (which has the highest Ga content of ≈ 23.6 at.%). These differences are consistent with XRD and STM results (discussed below). In addition, no fractional streaks could be observed for the samples grown onto aFM substrates.

Table 6.1 also indicates the thicknesses of our FeGa films, as determined from RBS measurements. Based on their thickness, all films can be considered bulk-like. An exception

Table 6.1: Sample number, corresponding substrate, growth temperature, film thickness, and Ga concentration for the FeGa films.

Sample	Substrate	T_S [°C]	Thickness [nm]	x [at.% Ga]
822	MgO(001)	320 ± 15	109 ± 10	7.9 ± 1.2
823	MgO(001)	360 ± 15	186 ± 16	15.2 ± 1.5
826	MgO(001)	420 ± 20	140 ± 12	15.2 ± 1.5
824	MnN(001)/MgO(001)	320 ± 15	48 ± 4	23.6 ± 2.4
825	MnN(001)/MgO(001)	360 ± 15	116 ± 10	15.7 ± 1.5
828	Mn_3N_2(001)/MgO(001)	390 ± 15	109 ± 10	15.3 ± 1.5

could apply to thinner film 824; however, from RHEED patterns recorded during growth we observe that the *in-plane* lattice constant for this film remains unchanged after less than 20 nm. This observation is similar to studies of FeGa films grown on ZnSe/GaAs(001) substrates, which indicate that the films relax to bulk-like values after only several nm.[126]

Shown in Fig. 6.2 are XRD measurements for the six FeGa films; we find that all films are single-crystalline and grow with a (001) orientation on all substrates. The highest intensity peaks come from the MgO substrate. The positions of the MgO, MnN, and Mn_3N_2 peaks are also identified and labeled on the plot. The inset shows a 2θ span of 5° covering the FeGa peak region. It is evident that the samples grown on MgO substrates (black, red, and green curves) exhibit sharper peaks, whereas the samples grown on MnN and Mn_3N_2 (magenta, purple, and blue curves) present broader peaks indicative of decreased crystal quality, in agreement with RHEED and STM measurements (discussed next). Also, note that the thinnest film 824 (blue curve) has the smallest intensity peak.

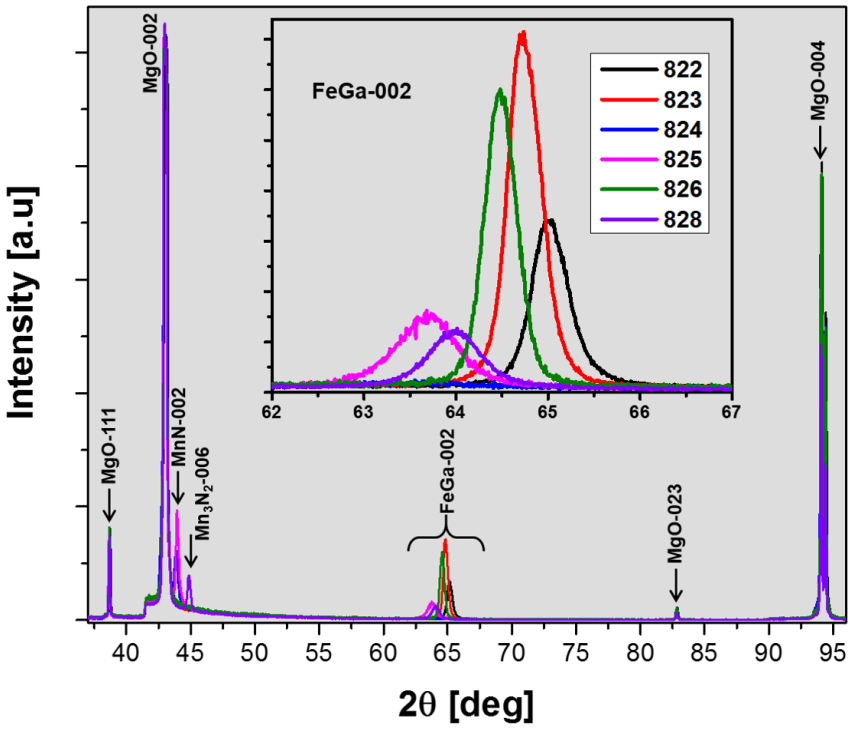

Figure 6.2: (a) θ-2θ XRD plots for all six FeGa films. The inset shows only the FeGa peak region. All films have (001) orientation and are single-crystalline; the smallest intensity peak comes from the thinnest film 824 (blue curve).

6.3.2 Surface morphology

Referring now to the STM investigations, Figs. 6.3(a)-(c) show the surface morphology of the FeGa films deposited onto MgO substrates. The most Fe-rich sample 822 [shown in Fig. 6.3(a)] shows a pyramidal morphology, with an average lateral pyramid size of about 20 nm. By looking at the STM images taken on same-composition samples 823 and 826, each having $\approx$ 15.2 at.% Ga in their structure, it can be observed that the morphologies are very different. Sample 823 [Fig. 6.3(b)] shows a pyramidal morphology similar to that of 822, although the pyramids are about 3 timer larger in lateral size and appear to be more connected. By looking at sample 826 [Fig. 6.3(c)] a spiral morphology can be observed; also, the terraces are considerably larger compared to sample 823 and they also indicate

the presence of vacancy islands. This type of growth could be a result of the increased sample temperature during growth by about 60°C compared to sample 823. The insets from Figs.6.3(a) and (b) show a closer look at the observed pyramidal morphologies for samples 822 and 823, respectively.

For samples 825 and 828 (having similar composition but grown onto MnN and Mn_3N_2, respectively), the surface morphology (not shown) was very similar to that of sample 822 although a lot rougher, making the scanning process very challenging. This is also consistent with RHEED investigations on these samples, which show spottier patterns compared to samples grown on MgO. For the case of sample 824 ($\approx$ 23.6 at.% Ga), although it was found that some regions were rougher that others, a large portion of the imaged areas had a morphology similar to that shown in Fig. 6.3(d). One can see that by increasing the Ga concentration, the surface exhibits a stepped morphology with straight and well-defined step edges. Also noticeable are a variety of different surface arrangements that appear in close proximity to one another, as visible in the inset of Fig. 6.3(d). There one can see two distinct types or rows having different widths (and emphasized by the dotted boxes), together with some featureless areas. Two distinct types of rows could occur if they have different or varying composition. An interesting observation is that the smaller width rows are perfectly parallel to one another, whereas the wider rows exhibit some irregularities and distortions. We do not attribute these differences to a tip effect, since we would then expect for these distortions to occur across several lines on the image.

To understand the different morphologies observed in STM, we next address the phase diagram of FeGa. For compositions lower than $\approx$ 15 at.% Ga (considered to be within the solubility limit of Ga in Fe) the Ga atoms take random positions within the FeGa matrix forming the disordered A2 phase. For concentrations between $\approx$ 15 and $\approx$ 23 at.% Ga, the FeGa alloy is in a mixed region of A2 and more ordered $D0_3$. For higher Ga contents, the FeGa alloy only exhibits ordered phases, $D0_3$ and B2.[114] We could therefore consider

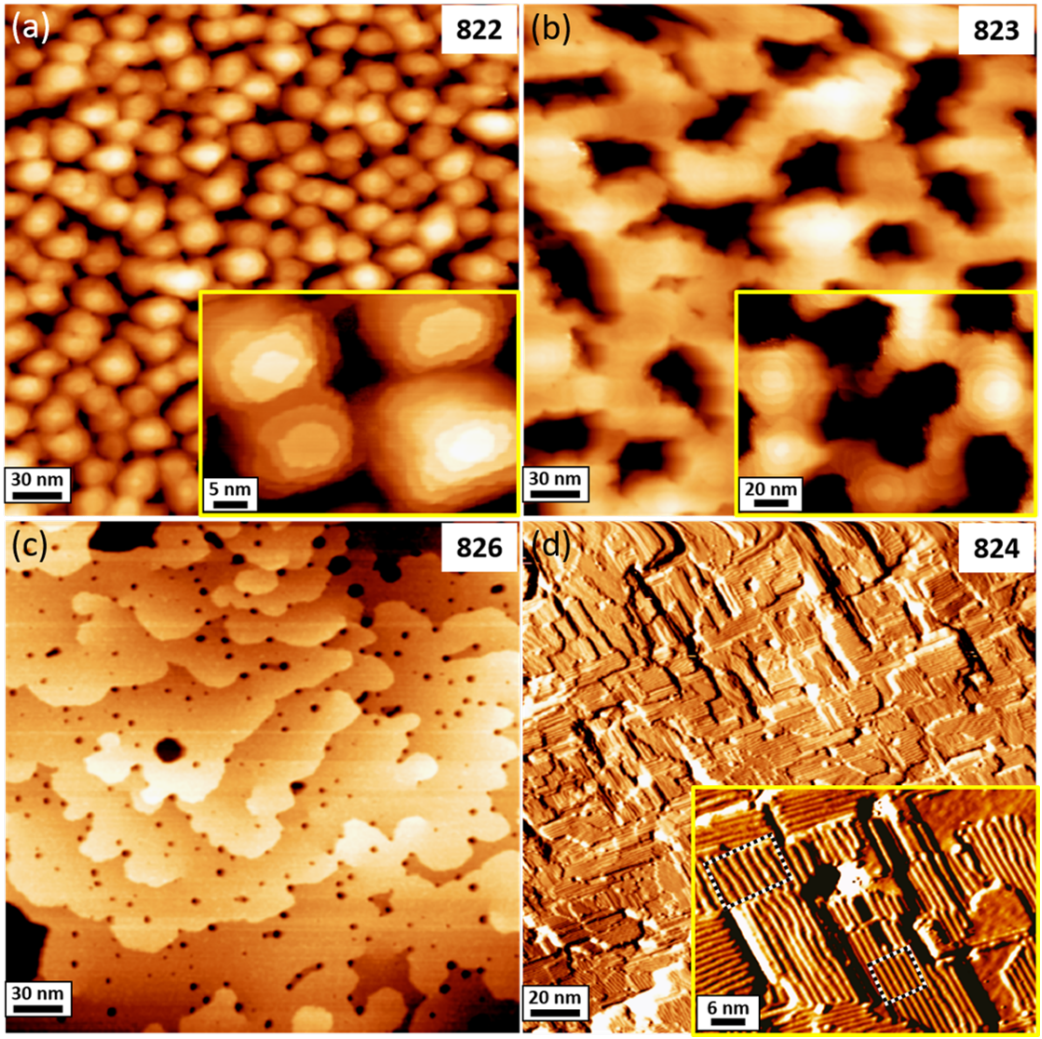

Figure 6.3: (a)-(c) 300 nm × 300 nm STM topographs acquired at room temperature for FeGa films deposited onto MgO substrates. (d) 200 nm × 200 nm room temperature STM topograph (shown in derivative mode) for FeGa deposited onto MnN substrates. The insets in (a), (b), and (d) represent a closer look at the morphology of the larger scale images. The dashed boxes in the inset of (d) emphasize two different row types. Scanning parameters for the images are: V_S = -1V and I_T = 0.05 nA (a), V_S = + 0.3V and I_T = 0.1 nA (b), V_S = + 1V and I_T = 0.05 nA (c), V_S = + 2V and I_T = 0.1 nA (d).

that the areas shown in Figs. 6.3(a)-(c) come most likely from the A2 phase. Since sample 824 is in the right compositional range for a mixture of phases to occur, the observed row-structures could actually be an indication of such ordered phases. Moreover, studies on bulk single crystal FeGa alloys with a composition around 19 at.% Ga found that $D0_3$-phase

nanostructures (smaller than 2 nm) were dispersed within the A2 matrix.[117] Therefore, for higher Ga concentrations (similar to the one for sample 824) such structures should be easily observable by STM. However, since these surfaces are very complex it is difficult at this point to attribute the observed structures to a particular FeGa ordered phase.

6.3.3 Lattice parameters

In order to see if any deviations from the ideal cubic lattice exist in our films, we have compared the *in-plane* lattice constant obtained from RHEED-spacing measurements to the inter-planar distance (or *out-of-plane* lattice constant) obtained from XRD. Since for some samples the RHEED patterns were recorded at temperatures higher than RT, the values obtained from RHEED were corrected for thermal expansion with coefficients for bulk FeGa single crystals taken from literature.[134]

The comparison between RHEED and XRD values is shown in Fig. 6.4 and two observations can be made: 1) For growth on MgO substrates, the *in-plane* lattice constant remains about the same even if the Ga content increased from $\approx$ 7.9 at.% for sample 822 to $\approx$ 15.2 at.% for samples 823 and 826. However, the *out-of-plane* constant increased by about 1% with increasing Ga content, indicative of a slight tetragonal distortion. 2) For growth onto aFM substrates, the differences between the two lattice constants are more noticeable, with the XRD value being larger than the RHEED value by about 2% for sample 824 and by about 2.5% for samples 825 and 828. This indicates a more pronounced *out-of-plane* tetragonal distortion compared with samples grown on MgO substrates. From Fig. 6.4 sample 824 exhibits the largest *in-plane* and *out-of-plane* constants, which is expected given that this sample has the highest Ga content. From the same figure, samples 825 and 828 have the smallest *in-plane* lattice constants from all same-composition samples (823, 826, 825, and 828).

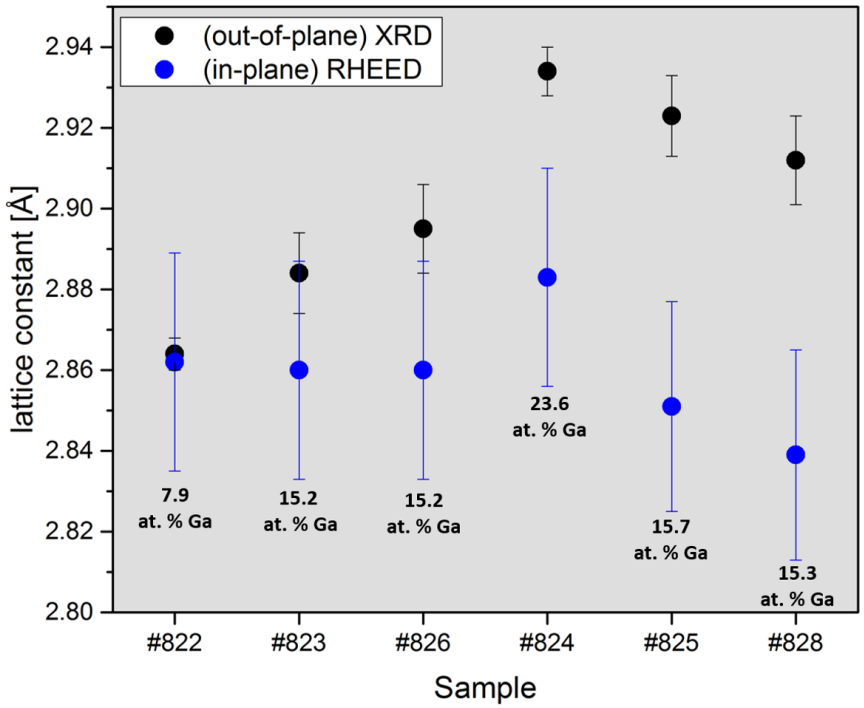

Figure 6.4: Comparison between the *out-of-plane* lattice constants (measured from XRD) and the *in-plane* lattice constants (obtained from RHEED) of FeGa films.

A pronounced tetragonal distortion was also observed for 36-nm thick FeGa films grown onto ZnSe/GaAs(001) substrates at 180°C with compositions ranging from 0 at.%Ga (i.e. pure Fe films) to about 29.4 at.%Ga.[126, 131] Interestingly, while the *out-of-plane* lattice changes considerably and continues to increase with Ga content, the *in-plane* constant remains unchanged and equal to that of pure Fe films. This unusual distortion was attributed to Ga-pairing along the [001] growth direction, in agreement with theoretical predictions also.[138]

Since our films were grown on different substrates and for a limited number of concentrations, it is unclear if we should expect a similar trend to the one described above. Nonetheless, it is clear that by changing substrates we were able to induce various degrees of strain in the FeGa structure. In order to establish a trend for the *in-plane* and *out-of-plane* constants, a careful future study can look at varying-composition samples grown at a single

temperature and on one type of substrate only. As mentioned before, studies have found $D0_3$- and B2-phase nanostructures dispersed within the A2 matrix of FeGa for selected Ga concentrations; such studies seem to disagree however on what type of distortions appear, some finding that the nanostructures are tetragonally distorted, while others imply exactly the opposite.[137, 138] An additional future study could look with STM at surfaces with varying Ga concentration and attempt to answer questions about the amounts of $D0_3$ and B2 clusters present in the structure and their associated lattice constants.

6.3.4 Magnetic properties

Using VSM, we have investigated the bulk magnetic properties of the six FeGa films and the results are shown in Fig. 6.5. The measurements were taken under *in-plane* fields applied along the [100] and [110] crystallographic directions. Starting with the FeGa films grown on MgO and considering the case of the least Ga-rich sample 822, we find that it exhibits anisotropies similar to those of pure Fe films, with the [100] direction as the easy-axis. As the Ga-concentration increases for samples 823 and 826 the Fe-like behavior is still present, with loops very similar to those of sample 822. In fact, the coercive fields H_c are almost identical among all three samples and found to be about 80 Oe. This kind of behavior is consistent with studies of similar composition FeGa films grown on MgO substrates.[124] From the large squareness (i.e. the ratio between the remnant and saturation magnetization values) of the hysteresis loops for samples 822, 823, and 826 (calculated to be ≈ 0.95) we can conclude that the magnetization of the samples stays in the film plane for the most part.

By looking at the results for samples 825 and 828, similar in composition to 823 and 826 but grown onto aFM substrates, we see that the Fe-like anisotropies are completely suppressed, with loops having almost identical behavior along both directions. It is interesting to point out that this loss of anisotropy was also observed for 72 nm thick

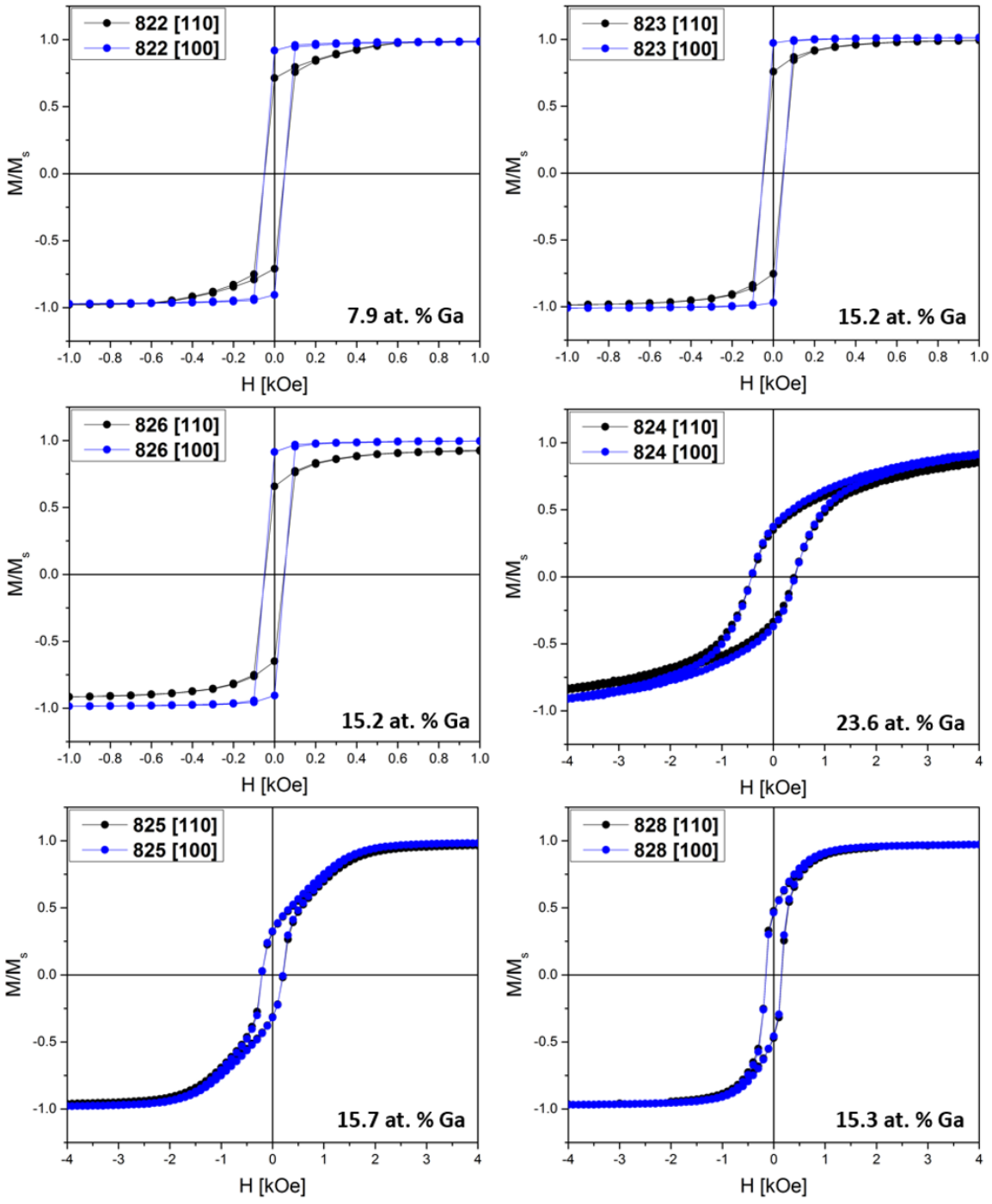

Figure 6.5: *In-plane* normalized magnetization versus applied field VSM loops for all six FeGa films, measured along the [100] and [110] crystallographic directions.

FeGa films of similar-composition grown on ZnSe/GaAs substrates.[128] In addition to the lack of *in-plane* anisotropy, the shapes of the hysteresis loops are very different compared to those of samples grown on MgO substrates. One immediate observation is that the coercivity increases considerably (note the different field values for the plots) and the remnant magnetization M_r decreases, the latter being an indication that the *out-of-plane* component of the magnetization in these films increases. Although samples 825 and 828 show similar behavior, the difference in substrates induces slight changes in the coercivity and remnant magnetization values. For the most Ga-rich sample 824, we again observe a loss of *in-plane* anisotropy and a decrease of the remnant magnetization value; in addition, this sample has the highest coercivity, of about 500 Oe.

From the magnetic behavior of FeGa films extracted from VSM measurements, we can conclude that their properties and magnetic parameters such as remnant magnetization and coercive field can be easily tuned by changing substrates.

We have investigated further the magnetic properties of the FeGa films using MFM imaging to study their domain structure. Figure 6.6 shows a comparison between samples grown onto aFM substrates, namely 824 ($\approx$ 23.6 at.% Ga), 825 ($\approx$ 15.7 at.% Ga), and 828 ($\approx$ 15.3 at.% Ga). Figures 6.6(a), (c), and (e) show the large scale topography, with samples 825 and 828 showing very similar and uniform topographies. For the case of sample 824 interruptions in the surface topography can be seen (some indicated by colored arrows); we believe that these lines come from the MgO substrate, and are visible given the smaller thickness of film 824 compared to that of films 825 and 828. The morphology is also quite interesting, with grid-like patterns visible in the lower left corner of Fig. 6.6(a); from the same image, similar grid-like patterns are also visible in between the substrate lines, although they are not as clear.

By looking at the magnetic signals from Figs. 6.6(b), (d), and (f) an immediate observation is that all samples grown onto aFM substrates exhibit stripe-like magnetic

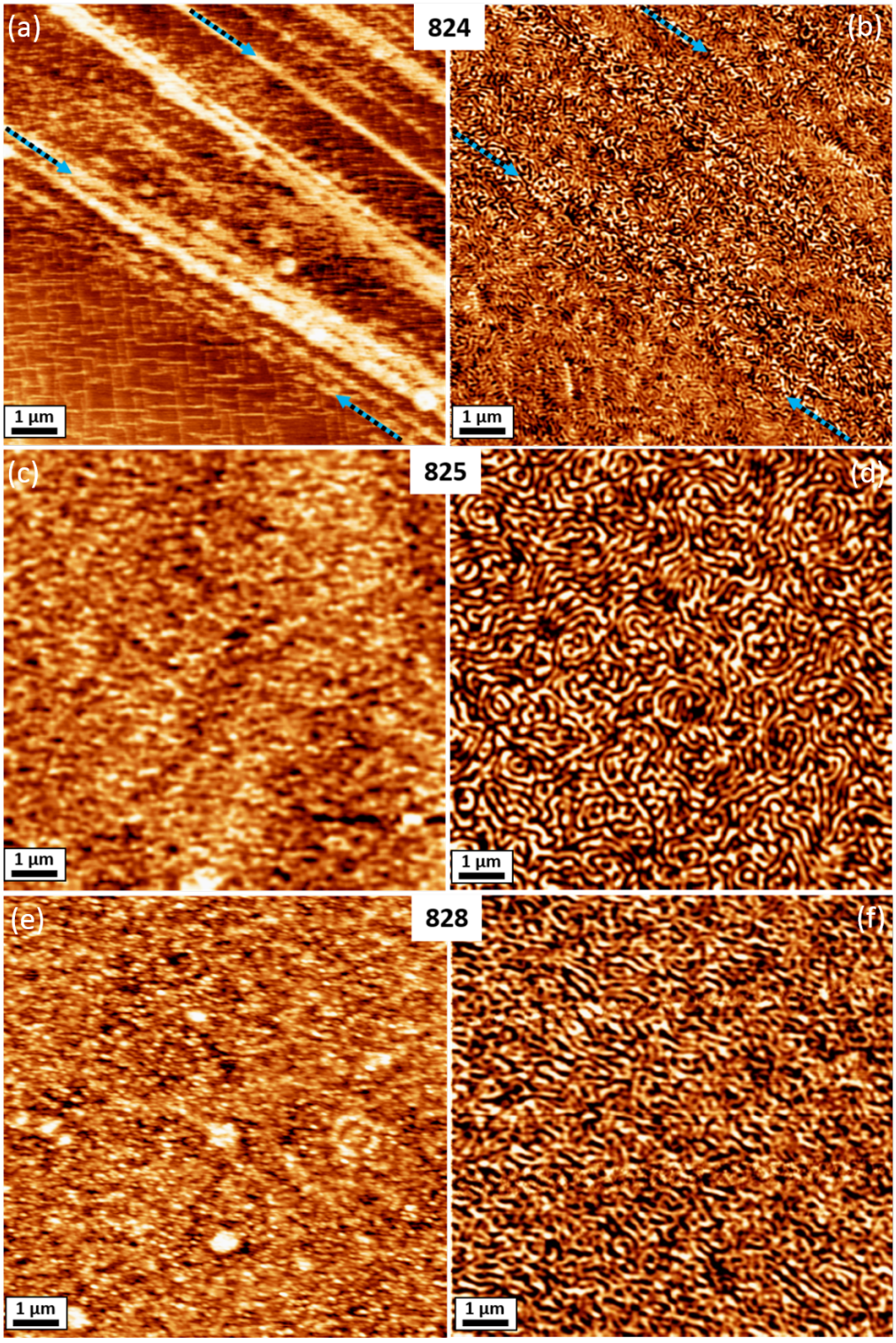

Figure 6.6: (a), (c), (e) 10 µm × 10 µm topography images acquired at room temperature for FeGa films deposited onto MnN (824, 825) and Mn_3N_2 (828) substrates. (b), (d), (f) represent corresponding MFM images acquired under no applied magnetic field.

domain patterns, independent of thickness or composition. We note that no field was applied to these samples before the MFM images were acquired. Such stripe-like domains are associated with an oscillating out-of-plane component of the magnetization in these films.[128, 135, 139] As discussed above, the hysteresis loops for samples 824, 825, and 828 indicate such a behavior by showing a reduction of the remnant magnetization (or an increase in the *out-of-plane* component of the magnetization).

Returning to the case of FeGa films grown on ZnSe/GaAs substrates, in addition to having an almost identical magnetic anisotropy behavior as our films, similar stripe-like domains were also observed. As already mentioned, these films were under compressive strain, with the *in-plane* lattice parameter constant for all compositions but with the *out-of-plane* parameter becoming increasingly larger with increasing Ga. These tetragonal deformations, explained as being a result of Ga-pairing along the [001] growth direction, were also believed to cause the appearance of stripe-like domains and PMA.[126, 128, 131] Although we have not established similar trends in the lattice parameters due to the lack of more than two compositions on a given substrate, from our XRD/RHEED measurements samples 824, 825, and 828 exhibit rather large tetragonal distortions. Whether or not a similar Ga-pairing mechanism is the cause for the observed tetragonal distortions, it is clear that PMA is present in our films.

In order to assess the domain orientation and periodicity, we have performed FFT analyses on parts of the images shown in Figs. 6.6(b), (d), and (f). The results are presented in Fig. 6.7. Interestingly, from the FFT analysis is it evident that samples 824 and 828 have some preferential alignment of domains along the [100] direction [see Figs. 6.7(d) and (f)]. That is not the case for sample 825 however [Fig. 6.7(e)], where the FFT image (which presents a more spherical shape) indicates more randomly oriented domains. Although all FFT images show some domain size non-uniformities, as indicated by diffuse halos with some distribution of radii, we were able to extract some average values for the domain sizes.

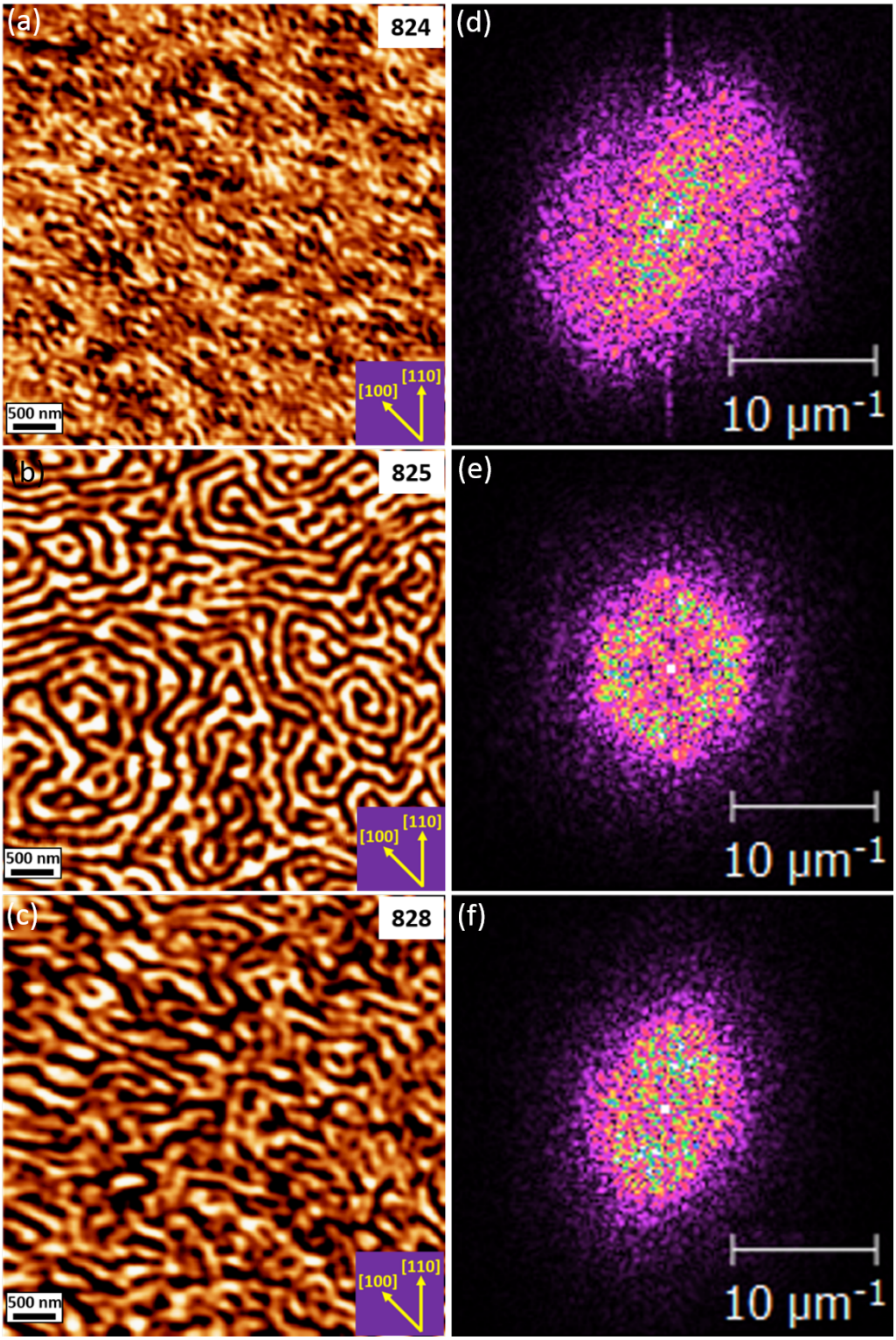

Figure 6.7: (a)-(c) 5 μm × 5 μm MFM images acquired at room temperature and under no magnetic field for FeGa films deposited onto MnN (824 and 825) and Mn_3N_2 (828) antiferromagnetic substrates. (d)-(f) corresponding FFT images.

By comparing domain sizes, it is evident from Figs. 6.7(a), (b) and (c) that the Ga-rich sample 824 exhibits the smallest domains, found to be 103 ± 23 nm. In contrast, the domain sizes for samples 825 and 828 are found to be similar in value with 184 ± 21 nm and 190 ± 26 nm, respectively.

A similar trend as we observe here, specifically a decrease in domain size as the Ga-concentration increases, was observed for both bulk single crystals and MBE-grown FeGa alloys.[116, 118, 119, 128] A direct comparison with the domain size of bulk single crystals cannot be made since they have a lot larger domain sizes than FeGa in thin film form. However, a comparison can be made with FeGa films grown on ZnSe substrates [128]; we find that our values for films 825/828 and 824 are close (although slightly larger) to values of ≈ 150 nm and ≈ 80 nm, respectively, for FeGa/ZnSe. We note that the values we compared with were obtained from MFM images taken at remanence (i.e. after applying a saturating magnetic field).

Figure 6.8 shows the domain structure and corresponding FFT images for same-composition samples 823 and 826, grown on MgO substrates. We note that the MFM images were taken after STM experiments, during which a 0.4 T *out-of-plane* field was applied (well above the saturation field of about 0.06 T for these samples). Since the images were taken in a remnant state, it is possible that what we see are some domains that remained aligned with the field. Nonetheless, as it can be seen, the domains are very different compared to similar composition samples grown on aFM substrates, with not-so-well defined strips running along the [100] crystallographic directions [as also evident from the FFT images from Figs. 6.8(c) and (d)]. Although the surface morphologies from STM are very different for samples 823 and 826 (see Fig. 6.3), their domain structures are extremely similar. This seems to be consistent with previous studies on FeGa bulk single crystal samples, which showed that the magnetic domain patterns have no correlation with the underlying microstructure.[136] A similar domain structure for these samples is

somewhat expected given that their hysteresis loops (shown in Fig. 6.5) have an almost identical behavior.

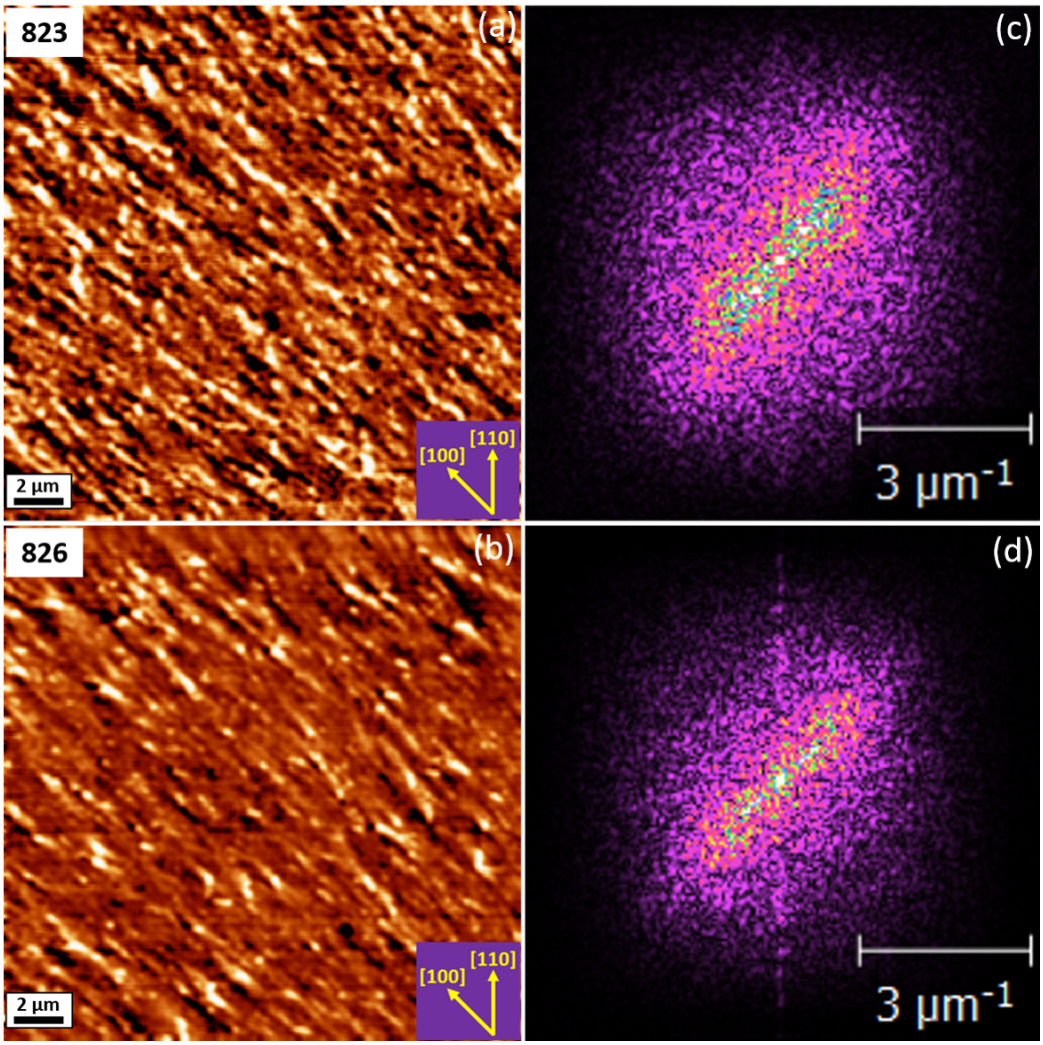

Figure 6.8: (a) and (b) 20 µm × 20 µm MFM images acquired at room temperature for FeGa films deposited onto MgO substrates (823 and 826); the images were taken at remanence after a 0.4 T *out-of-plane* field was applied during STM measurements. (c) and (d) represent the corresponding FFT images of (a) and (b), respectively.

Due to the observed differences in the hysteresis and magnetic domain behavior of the FeGa films, we have to consider the influence of the substrate.

From RBS, we also extract the composition of the manganese nitride substrate layers, finding Mn:N composition ratios of ≈ 1.11 (sample 824) and ≈ 1.16 (sample 825) for MnN, and ≈ 1.50 for Mn_3N_2 (sample 828); these values are in excellent agreement with previously reported values.[133] As discussed in the previous Chapter, the bulk sequence of Mn_3N_2(001) is one Mn layer followed by two MnN layers; In MnN(001), the Mn layer is absent. RBS also indicates the formation of a mixed layer (of a few nm) consisting of an Fe-Mn-Ga-N alloy for samples 824, 825, and 828. This is not surprising for sample 828 based on the results of Chapter 5 where we showed that Fe atoms replace Mn atoms in the Mn layers only, followed by Mn/N release at the surface; however, it is somewhat surprising for samples 824 and 825, due to the lack of Mn layers in the structure of MnN. Even so, note that the Mn:N ratio for the MnN is larger that one, implying that N vacancies are present in the structure, as also determined from previous investigations.[103, 133] A plausible explanation would then be that an Fe and/or Ga incorporation takes place within the MnN subsurface layers of MnN(001), with additional possible releases of Mn and/or N atoms to the surface.

Based on these considerations, the interface layers (which can have a high degree of disorder) are most likely responsible for the decreased crystal quality and rougher surfaces for samples 825 and 828. They can also be responsible for the large discrepancies that we see for the lattice constants between similar composition samples grown on MgO and manganese nitride substrates, which could then have a direct impact on the magnetic properties through the appearance of PMA.

6.4 Conclusions and future directions

These studies serve as a starting point for the FeGa system where the objective was to establish some of their basic properties. The short-term goal with this material system, i.e. growth, structure, and magnetic properties was achieved. We have successfully

grown FeGa films using MBE onto non-magnetic and antiferromagnetic substrates. We found that all films are single-crystalline and grow with a 45° *in-plane* rotation and (001) orientation on all substrates. We also investigated how the surface morphology changes with composition and sample temperature. Their magnetic properties were found to be different depending on the starting substrate. We established an Fe-like behavior for samples grown onto MgO substrates, with the [100] direction as easy-axis. In contrast, a loss of the *in-plane* anisotropy was observed for sample grown onto antiferromagnetic manganese nitride substrates accompanied by the formation of stripe-like domain patterns, consistent with the appearance of perpendicular magnetic anisotropy.

One long-term goal with the FeGa system is to investigate the stripe-like magnetic domains observed for samples grown onto aFM substrates under an applied field and to explore how their structure changes with thickness and composition, thus probing directly the magnetic anisotropies. Also, studying in more detail the effect of the alloyed interface on the resulting properties of FeGa could provide further insight into the tunability of this alloy system. Although not entirely unavoidable, one could try to control the extent of interface alloying by using, for example, lower growth temperatures and/or slower deposition rates.

Another long-term goal is to gain insight into how the magnetostrictive properties of these films affect other properties such as magnetism. Future directions for this material system involve the study of possible DOS changes with an applied magnetic field by means of STS. From VSM measurements, an applied field of 2 kOe (or about 0.2 T) is enough to saturate most samples. Since our STM allows us to apply magnetic fields (in both *in-plane* and *out-of-plane* orientations) of up to ≈ 0.4 T, such experiments are feasible. Furthermore, by obtaining atomic resolution images and establishing structural surface models can perhaps indicate how the Ga atoms are arranged in the overall bulk structure so that comparisons with theoretical predictions can be made.

Finally, by expanding our composition range to include the ≈ 19 at.% Ga value (where the first peak in MS occurs), further trends can be established. For example, using the same substrate and deposition temperature, we can look into how the FeGa lattice constants evolve over a large range of compositions, thus understanding how they affect the observed magnetic anisotropy.

7 CONCLUSIONS

From initial stages of interface formation to overall bulk characterizations, the studies presented here explored the structural and electronic/magnetic properties of ferromagnetic alloys of Mn and Fe with Ga as a function of composition and thickness when coupled with magnetic and/or non-magnetic systems. All material systems were prepared in ultra-high vacuum using molecular beam epitaxy, and their surfaces were investigated using room-temperature scanning tunneling microscopy and Auger electron spectroscopy. Additional theoretical calculations and/or bulk measurements were used to advance our understanding of these systems.

By studying a wide range of Mn:Ga composition ratios MnGa alloys deposited onto semiconducting GaN substrates, we have found that by varying their composition, the properties change in unexpected ways. For example, by growing $L1_0$-structured MnGa under slightly Mn-rich conditions we have established, by theory and experiment, that the surfaces contain about three times more Mn atoms than the bulk, which is found to be stoichiometric. Thus, it may be necessary to grow this material under slightly Mn-rich conditions in order to benefit from the properties of stoichiometric bulk MnGa films. By transitioning into the more Ga-rich regime of the same system we observed that in addition to the expected $L1_0$ phase, more Ga-rich phases develop and coexist over a large range of compositions. Using scanning tunneling microscopy imaging at room temperature, we probed the surface structure and film quality, finding that all films have very smooth and highly reconstructed surfaces. Using magnetometry characterizations, we have revealed that all films exhibit ferromagnetism, including the very Ga-rich ones. Unexpectedly, we have also found that giant perpendicular magnetic anisotropy and an increase in the magnetic moment of Mn are induced by decreasing the film thickness.

Thus, the magnetic properties of MnGa can be tuned not only by varying their composition but also by changing their thickness. Although unclear as to why some of these

properties change so drastically, these unexpected findings reinforce the richness of the MnGa system and open a whole new avenue of explorations. As a result of thorough surface investigations we are now able to distinguish between the surface structures of different stoichiometry films and these findings will play an important role when exploring further the mechanisms responsible for the appearance of perpendicular magnetic anisotropy. For example, since surface effects can become dominating as the film size decreases, a careful future study looking at same-composition films with varying thickness can explore in detail how the observed surface structures evolve with the film thickness.

We have also investigated the interface formation between sub-monolayer amounts of ferromagnetic iron and antiferromagnetic manganese nitride surfaces, using a combination of scanning tunneling microscopy/Auger electron spectroscopy and theoretical calculations. We found an unexpected substitution of Fe for Mn within specific subsurface layers and the formation of Mn (possibly MnN) islands on top. The resulting islands take on an electronic character of the substrate, and the incorporated Fe atoms take on the magnetic character of the substituted sites. Such a complex interfacial structure as we have found in this study can be present in other ferromagnetic/antiferromagnetic systems, and would undoubtedly play a very important role in the overall behavior of, for example, magnetic over-layers containing iron.

By combining Fe with Ga, we have studied magnetostrictive FeGa alloys over a range of Ga concentrations in their structure when deposited onto insulating magnesium oxide and antiferromagnetic manganese nitride substrates. It is the first-time FeGa has been grown onto manganese nitride and our previous results for only Fe depositions onto the same surfaces were found to directly affect the quality and magnetic properties of FeGa. Using molecular beam epitaxy with *in-situ* reflection high energy electron diffraction we were able to obtain single-crystalline films with extremely smooth surfaces for samples grown onto magnesium oxide substrates. For films grown onto manganese nitride, the surfaces were

found to have increased roughness, with the exception of Ga-rich alloys; the Ga-rich surfaces were found to exhibit about three different surface structures which can be attributed to more ordered FeGa phases. In terms of magnetism, we have revealed that the magnetic properties of FeGa films can be easily tuned by choosing different underlying substrates. Also, we have found alloyed interface layers between manganese nitride and FeGa over-layers which could be responsible for the complete loss of *in-plane* anisotropy and for the appearance of perpendicular magnetic anisotropy. Future studies looking closer at such interface effects could perhaps help understand further the observed magnetic anisotropies.

All these studies can potentially advance our understanding of the coupling between a ferromagnet and semiconducting or antiferromagnetic surfaces. In many cases, the simple A on B model is found to be unrealistic, and strain and interface effects have to be taken into account when interpreting results. Establishing the differences in magnetic properties at the atomic level and in bulk films can help identify the underlying factors responsible for their unique properties, leading perhaps to more successful devices.

REFERENCES

[1] P. A. Grünberg, Sensor Actuat. A **91**, 153 (2001).

[2] A. Fert, Revs. of Mod. Phys. **80**, 1517 (2008).

[3] S. A. Wolf, D. D. Awschalom, R. A. Buhrman, J. M. Daughton, S. von Molnár, M. L. Roukes, A. Y. Chtchelkanova, and D. M. Treger, Science **294**, 1488 (2001).

[4] E. Lu, D. C. Ingram, A. R. Smith, J. W. Knepper and F. Y. Yang, Phys. Rev. Lett. **97**, 146101 (2006).

[5] K. Wang and A. R. Smith, Nano Lett. **12**, 5443 (2012).

[6] E. M. Summers, T. A. Lograsso, and M. Wun-Fogle, J. Mater. Sci. **42**, 9582 (2007).

[7] A. Y. Cho and J. R. Arthur, Prog. Solid State Chem. **10**, 157 (1975).

[8] A. Y. Cho, Thin Solid Films **100**, 291 (1983).

[9] J. R. Arthur, Surf. Sci. **500**, 189 (2002).

[10] C. T. Foxon, J. Cryst. Growth **251**, 1 (2003).

[11] B. A. Joyce and T. B. Joyce, J. Cryst. Growth **264**, 605 (2004).

[12] J. E. Mahan, K. M. Geib, G. Y. Robinson, and R. J. Long, J. Vac. Sci. Technol. A **8**, 3692 (1990).

[13] A. Ichimiya and P. I. Cohen, *Reflection High Energy Electron Diffraction*, Cambridge University Press, Cambridge, UK (2004).

[14] N. W. Ashcroft and N. D. Mermin, *Solid State Physics*, Brooks/Cole, Belmont, CA (1976).

[15] G. Binnig, H. Rohrer, Ch. Gerber, and E. Weibel, Phys. Rev. Lett. **49**, 57 (1982).

[16] G. Binnig and H. Rohrer, Surf. Sci **126**, 236 (1982).

[17] R. Wiesendanger, *Scanning Probe Microscopy and Spectroscopy: methods and applications*, Cambridge University Press, Cambridge, UK (1994).

[18] S. N. Magonov and M.-H. Whangbo, *Surface Analysis with STM and AFM: experimental and theoretical aspects of image analysis*, VCH Verlagsgesellschaft mbH, Weinheim (Federal Republic of Germany) and VCH Publishers, Inc., New York, NY (1996).

[19] R. Wiesendanger, H.-J. Güntherodt, G. Güntherodt, R. J. Gambino, and R. Ruf, Phys. Rev. Lett. **65**, 247 (1990).

[20] M. Bode, Rep. Prog. Phys. **66**, 523 (2003).

[21] A. R. Smith, R. Yang, H. Yang, A. Dick, J. Neugebauer, and W. R. L. Lambrecht, Microsc. Res. Tech. **66**, 72 (2005).

[22] A. R. Smith, J. Scann. Probe Microsc. **1**, 3 (2006).

[23] R. Wiesendanger, Rev. Mod. Phys. **81**, 1495 (2009).

[24] J. Tersoff and D. R. Hamann, Phys. Rev. B **31**, 805 (1985).

[25] D. Wortmann, S. Heinze, Ph. Kurz, G. Bihlmayer, and S. Blügel, Phys. Rev. Lett. **86**, 4132 (2001).

[26] *Handbook of Auger Electron Spectroscopy*, Physical Electronics, Inc., Eden Prairie, MN (1995).

[27] T. E. Gallon and J. A. D. Matthew, Rev. Phys. Technol. **3**, 31 (1972).

[28] R. Shimizu, Jpn. J. Appl. Phys. **22**, 1631 (1983).

[29] Y. Goldstein, A. Many, O. Millo, S. Z. Weisz, and O. Resto, J. Vac. Sci. Technol. A **6**, 3130 (1988).

[30] K. Wang, W. Lin, A. V. Chinchore, Y. Liu, and A. R. Smith, Rev. Sci. Instrum. **82**, 053703 (2011).

[31] J. P. Corbett, S. G. Pandya, A.-O. Mandru, J. Pak, M. E. Kordesch, and A. R. Smith, Rev. Sci. Instrum. **86**, 026401 (2015).

[32] I. Horcas, R. Fernandez, J. M. Gomez-Rodriguez, J. Colchero, J. Gomez-Herrero and A. M. Baro, Rev. Sci. Instrum. **78**, 013705 (2007).

[33] F. J. Giessibl, Rev. Mod. Phys. **75**, 949 (2003).

[34] S. Porthun, L. Abelmann, and C. Lodder, J. Magn. Magn. Mater. **182**, 238 (1998).

[35] U. Hartmann, Annu. Rev. Mater. Sci. **29**, 53 (1999).

[36] A. Schwarz and R. Wiesendanger, Nano Today **3**, 28 (2008).

[37] C. S. Neves, P. Quaresma, P. V. Baptista, P. A. Carvalho, J. P. Araújo, E. Pereira, and P. Eaton, Nanotechnology **21**, 305706 (2010).

[38] M. Mayer, *Rutherford backscattering spectrometry (RBS)*, Lectures given at the Workshop on Nuclear Data for Science and Technology: Materials Analysis, Trieste (2003).

[39] S. Foner, Rev. Sci. Instrum. **30**, 548 (1959).

[40] R. L. Fagaly, Rev. Sci. Instrum. **77**, 101101 (2006).

[41] R. Kleiner, D. Koelle, F. Ludwig, and J. Clarke, Proc. IEEE, **92**, 1534 (2004).

[42] T. Graf, C. Felser and S. Parker, Prog. Solid State Chem. **39**, 1 (2011).

[43] X.Y. Dong, J.W. Dong, J.Q. Xie, T.C. Shih, S. McKernan, C. Leighton and C.J. Palmstrom, J. Cryst. Growth **254**, 384 (2003).

[44] H. G Meissner, K. Schubert, and T. R. Anantharaman, Proc. Ind. Acad. Sci. A **61**, 340 (1965).

[45] L. J. Zhu, D. Pan, S. H. Nie, J. Lu, and J. H. Zhao, Appl. Phys. Lett. **102**, 132403 (2013).

[46] S.-H. Kim, M. Boström, and D.-K. Seo, J. Am. Chem. Soc. **130**, 1384 (2008).

[47] J. Aoki, K. Morii, T. Matsui, and Y. Nakayama, Mater. Sci. Eng. **B10**, L5 (1991).

[48] M. Tanaka, J. P. Harbison, J. DeBoeck, T. Sands, B. Philips, T. L. Cheeks, and V. G. Keramidas, Appl. Phys. Lett. **62**, 1565 (1993).

[49] M. V. Dorokhin, D. A. Pavlov, A. I. Bobrov, Yu. A. Danilov, P. B. Demina, B. N. Zvonkov, A. V. Zdoroveishchev, A. V. Kudrin, N. V. Malekhonova and E. I. Malysheva, Phys. Solid State **56**, 2131 (2014).

[50] A. W. Arins, H. F. Jurca, J. Zarpellon, J. Varalda, I. L. Graff, W. H. Schreiner, and D. H. Mosca, IEEE Trans. Magn. **49**, 5595 (2013).

[51] W. Feng, D. D. Dung, Y. Shin, D. Van Thiet, S. Cho, and X. Hao, J. Korean Phys. Soc. **56**, 1382 (2010).

[52] K. K. Wang, E. Lu, J. W. Knepper, F. Y. Yang, and A. R. Smith, Appl. Phys. Lett. **98**, 162507 (2011).

[53] T. J. Nummy, S. P. Bennett, T. Cardinal, and D. Heiman, Appl. Phys. Lett. **99**, 252506 (2011).

[54] S. Mizukami, T. Kubota, F. Wu, X. Zhang, T. Miyazaki, H. Naganuma, M. Oogane, A. Sakuma, and Y. Ando, Phys. Rev. B **85**, 014416 (2012).

[55] T. Saito and R. Nishimura, J. Appl. Phys. **112**, 083901 (2012).

[56] F. Wu, S. Mizukami, D. Watanabe, H. Naganuma, M. Oogane, Y. Ando, and T. Miyazaki, Appl. Phys. Lett. **94**, 122503 (2009).

[57] F. Wu, E. P. Sajitha, S. Mizukami, D. Watanabe, T. Miyazaki, H. Naganuma, M. Oogane, and Y. Ando, Appl. Phys. Lett. **96**, 042505 (2010).

[58] H. Kurt, K. Rode, M. Venkatesan, P. Stamenov, and J. M. D. Coey, Phys. Rev. B **83**, 020405(R) (2011).

[59] J. Z. Wei, R. Wu, Y. B. Yang, X. G. Chen, Y. H. Xia, Y. C. Yang, C. S. Wang, and J. B. Yang, J. Appl. Phys. **115**, 17A736 (2014).

[60] Z. Li-Jun, N. Shuai-Hua, and Z. Jian-Hua, Chin. Phys. B **22**, 118505 (2013).

[61] L. Zhu, S. Nie, K. Meng, D. Pan, J. Zhao, and H. Zheng, Adv. Mater. **24**, 4547 (2012).

[62] A. Bedoya-Pinto, C. Zube, J. Malindretos, A. Urban and A. Rizzi, Phys. Rev. B **84**, 104424 (2011).

[63] A. R. Smith, V. Ramachandran, R. M. Feenstra, D. W. Greve, M.-S. Shin, M. Skowronski, J. Neugebauer, and J. E. Northrup, J. Vac. Sci. Technol. A **16**, 1641 (1998).

[64] A. R. Smith, R. M. Feenstra, D. W. Greve, M.-S. Shih, M. Skowronski, J. Neugebauer, and J. E. Northrup, J. Vac. Sci. Technol. B **16**, 2242 (1998).

[65] V. P. LaBella, M. R. Krause, Z. Ding, and P. M. Thibado, Surf. Sci. Rep. **60**, 1 (2005).

[66] A.-O. Mandru, R. Garcia-Diaz, K. Wang, K. Cooper, M. Haider, D. C. Ingram, N. Takeuchi, Appl. Phys. Lett. **103**, 161606 (2013).

[67] P. Giannozzi, S. Baroni, N. Bonini, M. Calandra, R. Car, C. Cavazzoni, D. Ceresoli, G. L. Chiarotti, M. Cococcioni, I. Dabo, A. Dal Corso, S. Fabris, G. Fratesi, S. de Gironcoli, R. Gebauer, U. Gerstmann, C. Gougoussis, A. Kokalj, M. Lazzeri, L. Martin-Samos, N. Marzari, F. Mauri, R. Mazzarello, S. Paolini, A. Pasquarello, L. Paulatto, C. Sbraccia, S. Scandolo, G. Sclauzero, A. P. Seitsonen, A. Smogunov, P. Umari, and R. M. Wentzcovitch, J.Phys.: Condens. Matter. **21**, 395502 (2009).

[68] J.P. Perdew, K. Burke, and M. Ernzerhof, Phys. Rev. Lett. **77**, 3865 (1996).

[69] K. Laasonen, A. Pasquarello, R. Car, C. Lee, and D. Vanderbilt, Phys. Rev. B **47**, 10142 (1993).

[70] J. Tersoff and D. R. Hamman, Phys. Rev. Lett. **50**, 1998 (1983).

[71] H. Niida, T. Hori, H. Onodera, Y. Yamaguchi, and Y. Nakagawa, J. Appl. Phys. **79**, 5946 (1996).

[72] A. Sakuma, J. Magn. Magn. Mater. **187**, 105 (1998).

[73] J. Aoki, K. Morii, T. Matsui, and Y. Nakayama, J. Mater. Sci. Lett. **11**, 941 (1992).

[74] K. Donishi, K. Morii, and Y. Nakayama, Mater. Trans. JIM **30**, 455 (1989).

[75] M. Boström and S. Hovmöller, J. Solid State Chem. **153**, 398 (2000).

[76] M. Tillard and Claude Belin, Intermetallics **29**, 147 (2012).

[77] A. O. Mandru, J. P. Corbett, J. M. Lucy, A. L. Richard, F. Yang, D. C. Ingram, and A. R. Smith, Appl. Surf. Sci. **367**, 312 (2016).

[78] J. S. Wu and K. H. Kuo, Metall. Mater. Trans. A **28A**, 729 (1997).

[79] K. K. Wang, N. Takeuchi, A. V. Chinchore, W. Lin, Y. Liu, and A. R. Smith, Phys. Rev. B **83**, 165407 (2011).

[80] J. Tersoff, Phys. Rev. Lett. **81**, 3183 (1998).

[81] J. E. Guyer and P. W. Voorhees, Phys. Rev. B **54**, 11710 (1996).

[82] S. Pereira, M. R. Correia, E. Pereira, K. P. O'Donnell, E. Alves, A. D. Sequeira, N. Franco, I. M. Watson, and C. J. Deatcher, Appl. Phys. Lett. **80**, 3913 (2002).

[83] A. G. Cullis, D. J. Robbins, A. J. Pidduck, and P. W. Smith, J. Cryst. Growth **123**, 333 (1992).

[84] T. Wiebach, M. Schmidbauer, M. Hanke, H. Raidt, R. Köhler, and H. Wawra, Phys. Rev. B **61**, 5571 (2000).

[85] Z. Yang, J. Li, D.-S. Wang, K. Zhang, and X. Xie, J. Magn. Magn. Mater. **182**, 369 (1998).

[86] G. Kim, Y. Sakuraba, M. Oogane, Y. Ando, and T. Miyazaki, Appl. Phys. Lett. **92**, 172502 (2008).

[87] K. Barmak, J. Kim, L. H. Lewis, K. R. Coffey, M. F. Toney, A. J. Kellock, and J.-U. Thiele, J. Appl. Phys. **98**, 033904 (2005).

[88] T. Seki, S. Mitani, K. Yakushiji, and K. Takanashi, Appl. Phys. Lett. **88**, 172504 (2006).

[89] T. Seki, T. Shima, K. Takanashi, Y. Takanashi, E. Matsubara, and K. Hono, Appl. Phys. Lett. **82**, 2461 (2003).

[90] N. Nakajima, T. Koide, T. Shidara, H. Miyauchi, H. Fukutani, A. Fujimori, K. Iio, T. Katayama, M. Nývlt, and Y. Suzuki, Phys. Rev. Lett. **81**, 5229, (1998).

[91] A.-O. Mandru, J. Pak, A. R. Smith, J. Guerrero-Sanchez, and N. Takeuchi, Phys. Rev. B **91**, 094433 (2015).

[92] I. Vobornik, G. Panaccione, J. Fujii, Z.-H. Zhu, F. Offi, B. R. Salles, F. Borgatti, P. Torelli, J. P. Rueff, D. Ceolin, A. Artioli, M. Unnikrishnan, G. Levy, M. Marangolo, M. Eddrief, D. Krizmancic, H. Ji, A. Damascelli, G. van der Laan, R. G. Edgell, and R. J. Cava, J. Phys. Chem. C **118**, 12333 (2014).

[93] V. Sessi, F. Otte, S. Krotzky, C. Tieg, M. Wasniowska, P. Ferriani, S. Heinze, J. Honolka, and K. Kern, Phys. Rev. B **89**, 205425 (2014).

[94] S. J. Pearton, C. R. Abernathy, M. E. Overberg, G. T. Thaler, D. P. Norton, N. Theodoropoulou, A. F. Hebard, Y. D. Park, F. Ren, J. Kim, and L. A. Boatner, J. Appl. Phys. **93**, 1 (2003).

[95] W. Lin, A.-O. Mandru, A. R. Smith, N. Takeuchi, and H. A. H. Al-Brithen, Appl. Phys. Lett. **104**, 171607 (2014).

[96] T. Lan Anh Tran, D. Çakir, P. K. Johnny Wong, A. B. Preobrajenski, G. Brocks, W. G. van der Wiel, and M. P, de Jong, Appl. Mater. Interfaces **5**, 837 (2013).

[97] A. Reserbat-Plantey, P. Gava, N. Bendiab, and A. M. Saitta, EPL **96**, 57001 (2011).

[98] J. Nogués and I. K. Schuller, J. Magn. Magn. Mater. **192**, 203 (1999).

[99] R. L. Stamps, J. Phys. D: Appl. Phys. **33**, R247 (2000).

[100] R. Ravlić, M. Bode and R. Wiesendanger, J. Phys.: Condens. Matter **15**, S2513 (2003).

[101] Y. J. Choi, I. C. Jeong, J.-Y. Park, S.-J. Kahng, J. Lee and Y. Kuk, Phys. Rev. B **59**, 10918 (1999).

[102] G. Kreiner and H. Jacobs, J. Alloy. Compd. **183**, 345 (1992).

[103] H. Yang, H. Al-Brithen, E. Trifan, D. C. Ingram and A. R. Smith, J. Appl. Phys. **91**, 1053 (2002).

[104] David Vanderbilt, Phys. Rev. B **11**, 7892 (1990).

[105] M. Methfessel and A. T. Paxton, Phys. Rev. B **40**, 3616 (1989).

[106] H. J. Monkhorst and J. D. Pack, Phys. Rev. B **13**, 5188 (1976).

[107] W. R. L. Lambrecht, M. Prikhodko, and M. S. Miao, Phys. Rev. B **68**, 174411 (2003).

[108] G.-X. Qian, R. M. Martin, and D. J. Chadi, Phys. Rev. B **38**, 7649 (1988).

[109] J. Guerrero-Sanchez, A. O. Mandru, K. Wang, N. Takeuchi, J. H. Cocoletzi, and A. R. Smith, Appl. Surf. Sci. **355**, 623 (2015).

[110] J. Guerrero-Sanchez, A. O. Mandru, N. Takeuchi, J. H. Cocoletzi, and A. R. Smith, Appl. Surf. Sci. **363**, 651 (2016).

[111] A. V. Chinchore, K. Wang, M. Shi, Y. Liu, and A. R. Smith, Appl. Phys. Lett. **100**, 061602 (2012).

[112] A. E. Clark, J. B. Restorff, M. Wun-Fogle, T. A. Lograsso, and D. L. Schlagel, IEEE Trans. Magn. **36**, 3238 (2000).

[113] A. E. Clark, K. B. Hathaway, M. Wun-Fogle, J. B. Restorff, T. A. Lograsso, V. M. Keppens, G. Petculescu, and R. A. Taylor, J. Appl. Phys. **93**, 8621 (2003).

[114] E. M. Summers, T. A. Lograsso, and M. Wun-Fogle, J. Mater. Sci. **42**, 9582 (2007).

[115] H. Okamoto, Bull. Alloy Phase Diagr. **11**, 576 (1990).

[116] F. Bai, J. Li, D. Viehland, D. Wu, and T. A. Lagrasso, J. Appl. Phys. **98**, 023904 (2005).

[117] S. Bhattacharyya, J. R. Jinschek, A. Khachaturyan, H. Cao, J. F. Li, and D. Viehland, Phys. Rev. B **77**, 104107 (2008).

[118] F. Bai, H. Zhang, J. Li, and D. Viehland, Appl. Phys. Lett. **95**, 152511 (2009).

[119] J. Zhang, T. Ma, and M. Yan, Physica B **405**, 3129 (2010).

[120] J. Atulasimha and A. B. Flatau, Smart Mater. Struct. **20**, 043001 (2011).

[121] J. L. Weston, A. Butera, T. Lagrasso, M. Shamsuzzoha, I. Zana, G. Zangari, and J. Barnard, IEEE Trans. Magn. **38**, 2832 (2002).

[122] A. Butera, J. Gómez, J. L. Weston, and J. A. Barnard, J. Appl. Phys. **98**, 033901 (2005).

[123] O. M. J. van 't Erve, C. H. Li, G. Kioseoglou, A. T. Hanbicki, M. Osofsky, S.-F. Chen, and B. T. Jonker, Appl. Phys. Lett. **91**, 122515 (2007).

[124] A. McClure, E. Arenholz, and Y. U. Idzerda, J. Vac. Sci. Tech. A **28**, 969 (2010).

[125] D. A. Resnik, A. McClure, C. M. Kuster, P. Rugheimer, and Y. U. Idzerda, J. Appl. Phys. **109**, 07A938 (2011).

[126] M. Eddrief, Y. Zheng, S. Hidki, B. Rache Salles, J. Milano, V. H. Etgens, and M. Marangolo, Phys. Rev. B **84**, 161410(R) (2011).

[127] D. E. Parkes, S. A. Cavill, A. T. Hindmarch, P. Wadley, F. McGee, C. R. Staddon, K. W. Edmonds, R. P. Campion, B. L. Gallagher, and A. W. Rushforth, Appl. Phys. Lett. **101**, 172402 (2012).

[128] M. Barturen, B. Rache Salles, P. Schio, J. Milano, A. Butera, S. Bustingorry, C. Ramos, A. J. A. de Oliveira, M. Eddrief, E. Lacaze, F. Gendron, V. H. Etgens, and M. Marangolo, Appl. Phys. Lett. **101**, 092404 (2012).

[129] D. E. Parkes, L. R. Shelford, P. Wadley, V. Holý, M. Wang, A. T. Hindmarch, G. van der Laan, R. P. Campion, K. W. Edmonds, S. A. Cavill, and A. W. Rushforth, Sci. Rep. **3**, 2220 (2013).

[130] B. Gobaut, R. Ciprian, B. R. Salles, D. Krizmancic, G. Rossi, G. Panaccione, M. Eddrif, M. Marangolo, and P. Torelli, J. Magn. Magn. Mater. **383**, 56 (2014).

[131] M. Barturen, J. Milano, M. Vásquez Mansilla, C. Helman, M. A. Barral, A. M. Llois, M. Eddrief, and M. Marangolo, Phys. Rev. B **92**, 054418 (2015).

[132] A. McClure, S. Albert, T. Jaeger, H. Li, P. Rugheimer, J. A. Schaefer, and Y. U. Idzerda, J. Appl. Phys. **105**, 07A938 (2009).

[133] F. Lihl, P. Ettmayer, A. Kutzelnigg, Z. Metallk. **53** 715 (1962).

[134] S. Datta, M. Huang, J. Raim, T. A. Lograsso, A. B. Flatau, Mater. Sci. Eng., A **435-436**, 221 (2006).

[135] E. Sallica Leva, R. C. Valente, F. Martínez Tabares, M. Vásquez Mansilla, R. Roshdestwensky, and A. Butera, Phys. Rev. B **82**, 144410 (2010).

[136] Q. Xing and T. A. Lagrasso, Appl. Phys. Lett. **93**, 182501 (2008).

[137] H. Cao, P. M. Gehring, C. P. Devreugd, J. A. Rodriguez-Rivera, J. Li, and D. Viehland, Phys. Rev. Lett. **102**, 127201 (2009).

[138] Hui Wang, Y. N. Zhang, Teng Yang, Z. D. Zhang, L. Z. Sun, and R. Q. Wu, Appl. Phys. Lett. **97**, 262505 (2010).

[139] A. Hubert and R. Schäfer, *Magnetic Domains: The Analysis of Magnetic Microstructures*, Springer, Berlin (2000).

Appendix A: STM Body Construction

Some of the details behind constructing the back-up STM body are described below. This is part of a more extensive document that includes all the equipment and materials used, together with a detailed step-by-step procedure. Initially, the body was constructed as a spare for the RT system in lab 151, with the scope of saving a lot of time and effort in case the existing one malfunctions. However, it can be easily implemented into a low- or variable-temperature STM system with high magnetic fields applied, and it can work in both horizontal and vertical orientations.

This project was possible by constant communication with the machine shop technicians, whose help with the machining of various parts was crucial. These parts had been previously developed by KangKang Wang and Wenzhi Lin.[30] KangKang also provided me with invaluable support during the construction stage. Building a new STM body was an extremely beneficial experience for me, as it required constant evaluation and improvement of my laboratory skills. It also gave me a chance to understand better some of the aspects that one has to be careful with when operating the STM.

Figure A.1 shows images taken at various stages of the construction process.

As with the existing STM body, the coarse approach is achieved through six piezo-ceramic stacks mounted onto phosphor-bronze beams [see Fig. A.1(a)] and in contact with a sapphire prism via high-purity Alumina plates. One of the most challenging parts was preparing the actual piezo-stacks. The four pieces that make a single stack are cut out of a larger $0.6'' \times 0.6''$ plate [see inset of Fig. A.1(a)] using a band saw; the polarization direction of a plate is indicated by the red arrows. Due to their brittleness, extreme care has to be taken during the cutting process. A single stack is prepared by glueing four individual pieces (each with alternating polarization directions) together using conductive epoxy. Additional care is needed during the glueing step, since just the right amount of epoxy has to be applied in order to prevent shorting of the stack due to spills. Electrical connections for each stack

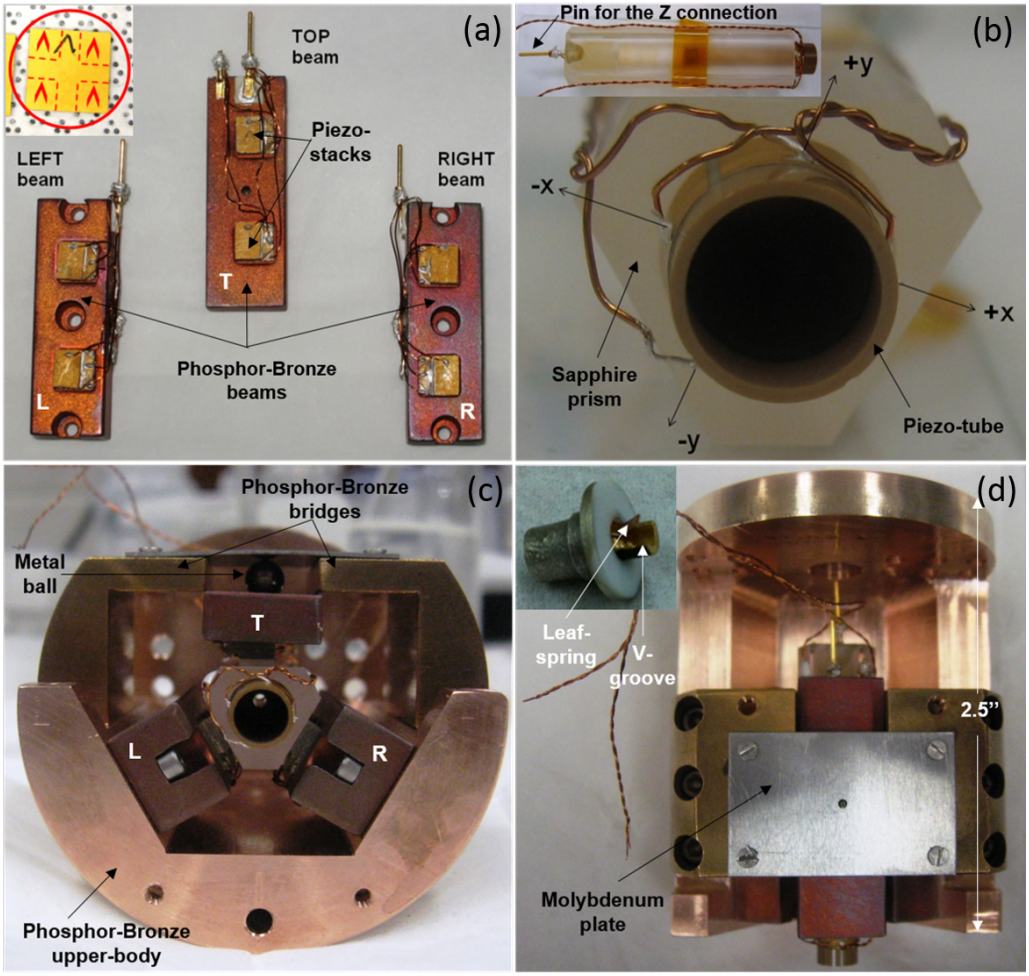

Figure A.1: Partial assembly process of the STM body. (a) Six piezo-stacks already mounted onto the three phosphor-bronze beams that will later enclose the sapphire prism for the coarse approach motion; the inset shows the square piezo-plate from which the four pieces for each stack were cut (the red arrows indicate the polarization direction). (b) Piezo-tube mounted inside the sapphire prism, showing the ± X and ± Y wire connections; the inset shows a top-view of the prism and piezo-tube assembly, with the Z connection visible. (c) and (d) Front- and top- views of the completed STM body, with all components mounted onto the phosphor-bronze upper-body. The inset in (d) shows an assembly consisting of a MACOR bushing, a phosphor-bronze V-groove, and a leaf-spring, which will be later mounted inside the exposed part of the piezo-tube.

are done using 0.008″ diameter Cu wires. Once all six stacks are prepared, they are glued onto the three beams (T-top, L-left, and R-right) visible in Fig. A.1(a), using conductive epoxy. Further steps include finalizing the electrical connections for each beam, and capping the top of each stack with small Alumina pads (not shown).

The scanning is possible by using a five-electrode piezo-ceramic tube (1″ in length, 0.25″ in outer diameter, and 0.02″ in thickness) glued inside the sapphire prism via a MACOR scanner support. The prism-tube assembly is shown in Fig. A.1(b). A voltage applied to the four (± X and ± Y) outer electrodes bends the tube and allows it to raster across the sample, whereas a voltage applied to the inner (Z) electrode expands or contracts the tube along its axis. The ± X and ± Y connections (consisting of 0.008″ diameter Cu wires) are attached to the four quadrants of the piezo-tube using conductive epoxy. The electrical connection for the Z motion is made inside the piezo-tube and it is visible in the inset of Fig. A.1(b).

Next steps involve: i) mounting the left and right beams onto the upper STM body; ii) bolting the left and right phosphor-bronze bridges onto the upper body; iii) resting the prism-tube assembly onto the two lower beams; iv) placing the top beam on the prism; v) placing the metal ball onto the top beam; vi) attaching the thin molybdenum plate on top of everything, making sure that the metal ball rests at the center of the plate. The molybdenum plate is used for controlling the pressure applied to the piezo-prism contact, whereas the metal ball is merely used for equal distribution of pressure.

Figures A.1(c) and A.1(d) show two different views of the final STM body. Subsequently, the metallic tip used in scanning is fit snugly inside a tungsten holder (not shown) and mounted inside the assembly seen in the inset of Fig. A.1(d). This assembly is glued inside the exposed end of the piezo-tube, and consists of a MACOR bushing (for support), a phosphor-bronze V-groove (for inserting the tip holder) and a leaf spring (for adjusting the tension exerted on the piezo-tube when the tip holder is inserted).

As a final note regarding the choice of materials, phosphor-bronze is used for the main body, coarse approach beams, bridges, and V-groove due to its low cost, malleability, low susceptibility, and high thermal conductivity.

Appendix B: Determination of Sensitivity Factors for the AES Analyzer

In order to calibrate our system, we have prepared three control samples using MBE: i) body-centered cubic Fe(001) grown on MgO(001); ii) MnN(001) grown on MgO(001); and iii) GaN(000$\bar{1}$) grown on sapphire. Thus, we are able to obtain sensitivity factors for Fe, Mn, N, and Ga. We investigated binary samples with surface elemental composition ratios very similar to bulk values. The θ phase of manganese nitride was chosen since its surface Mn:N ratio is closest to 1:1; the GaN control sample was prepared with a 1×1 termination as observed from RHEED at RT. The RHEED patterns (not shown here) for all samples were very streaky, indicative of smooth surfaces.

Following sample preparation, Auger spectra were acquired with an incident beam energy of 5 keV and within the same energy window, 350 eV to 1125 eV, for all samples. Other parameters, such as primary electron beam current, emission current, multiplier voltage, step size, and dwell time, were also kept the same for all spectra. Figure B.1 shows the resulting dN(E)/dE versus Auger electron energy spectra obtained for the three samples. The differentiation process removes the background and also allows one to measure accurately the intensity of a particular peak (given by the peak-to-peak amplitude). A five-point smoothing followed the differentiation process. The main peaks are labeled on each spectrum and they correspond to the KLL transition for N_{389}, and to the LMM transitions for Fe_{705}, Ga_{1069}, and Mn_{592}.[26]

Sensitivity factors are then calculated with respect to a given reference sample [26]; we choose as reference the spectrum of the Fe sample, for which we measure the peak-to-peak amplitude of Fe_{705} LMM transition, I_r, and we set its sensitivity factor S_r to be 1. Based on the approach in reference [26], for a sample made of a single element A (such as Cr) the

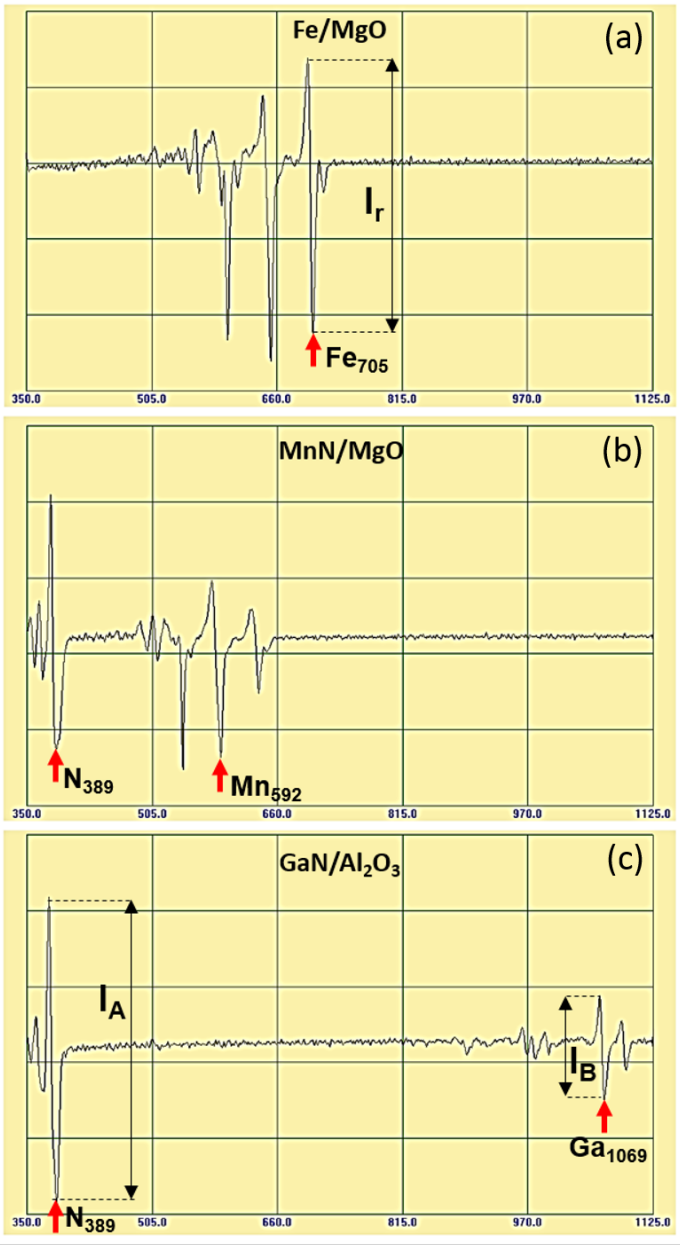

Figure B.1: dN(E)/dE versus Auger electron energy spectra, followed by a 5 point smoothing for three control samples used to determine the sensitivity factors of our analyzer: Fe/MgO (a), MnN/MgO (b), and GaN/Sapphire (c). The peaks corresponding to the main transitions are indicated on each spectrum by red arrows. The *x* axis is the same for all spectra, i.e. 350 - 1125 eV.

following equation is used to determine the unknown sensitivity factor S_A:

$$S_A = \left(\frac{\rho_r}{\rho_A}\right)\frac{I_A}{I_r}S_r \ , \tag{B.1}$$

where ρ_r is the atomic density of Fe, I_A is the peak-to-peak amplitude for element A, and ρ_A is the atomic density of element A. For a compound sample A_xB_y (such as GaN or MnN) the ratio of the densities in equation (B.1) can be replaced by the molecular formula of the compound [26], and the resulting sensitivity factor S_A of element A is given by:

$$S_A = \left(\frac{x+y}{x}\right)\frac{I_A}{I_r}S_r \ . \tag{B.2}$$

For element B, the sensitivity factor S_B is given by:

$$S_B = \left(\frac{x+y}{y}\right)\frac{I_B}{I_r}S_r \ , \tag{B.3}$$

where I_B is the peak-to-peak amplitude for element B.

Even with reliable sensitivity factors, the error in the elemental ratios extracted from AES measurements is rather large. Sources of error can come from: i) changes in the chemistry of a given element when part of different compounds, which can have an impact on the peak shape and position; ii) surface roughness; or iii) matrix effects, that can affect the electron escape depth. For our case, we estimate the error in the elemental ratios to be at the very most 20%. Using the new values for the sensitivity factors together with simple modeling allowed us to successfully probe the locations of atomic species within various structures, resulting in excellent agreement with experimental and theoretical results.[66, 91, 95]

Appendix C: List of Publications

1. "Structure and Magnetism in Ga-rich MnGa/GaN Thin Films and Unexpected Giant Perpendicular Anisotropy in the Ultra-Thin Film Limit", **Andrada-Oana Mandru**, Joseph P. Corbett, Jeremy M. Lucy, Andrea L. Richard, Fengyuan Yang, David C. Ingram, and Arthur R. Smith, *Appl. Surf. Sci.* **367**, 312 (2016).

2. "Understanding the Stability of Fe Incorporation within $Mn_3N_2(001)$ Surfaces: An ab-initio Study", Jonathan Guerrero-Sanchez, **Andrada-Oana Mandru**, Noboru Takeuchi, Gregorio H. Cocoletzi, and Arthur R. Smith, *Appl. Surf. Sci.* **363**, 651 (2016).

3. "Structural, Electronic, and Magnetic Properties of $Mn_3N_2(001)$ Surfaces", Jonathan Guerrero-Sanchez, **Andrada-Oana Mandru**, Kangkang Wang, Noboru Takeuchi, Gregorio H. Cocoletzi, and Arthur R. Smith, *Appl. Surf. Sci.* **355**, 623 (2015).

4. "Molecular Beam Epitaxial Growth and Scanning Tunneling Microscopy Studies of the Gallium Rich Trench Line Structure on N-polar w-GaN$(000\bar{1})$", Zakia Alhashem, **Andrada-Oana Mandru**, Jeongihm Pak, and Arthur R. Smith, *J. Vac. Sci. Technol. A* **33**, 061404 (2015).

5. "Surface structure of manganese gallium quantum height islands on wurtzite GaN$(000\bar{1})$ studied by scanning tunneling microscopy", Jeongihm Pak, **Andrada-Oana Mandru**, Abhijit Chinchore, and Arthur R. Smith, *Appl. Phys. A* **120**, 1027 (2015).

6. "Interface formation for a ferromagnetic/antiferromagnetic bilayer system studied by scanning tunneling microscopy and first-principles theory", **Andrada-Oana Mandru**, Jeongihm Pak, Arthur R. Smith, Jonathan Guerrero-Sanchez, and Noboru Takeuchi, *Phys. Rev. B* **91**, 094433 (2015).

7. "Note: Advancement in tip etching for preparation of tunable size scanning tunneling microscopy tips", J. P. Corbett, S. G. Pandya, **A.-O. Mandru**, J. Pak, M. E. Kordesch, and A. R. Smith, *Rev. Sci. Instrum.* **86**, 026104 (2015).

8. “Iron on GaN(0001) pseudo-1 $\times$ 1 (1+1/12) investigated by scanning tunneling microscopy and first-principles theory”, Wenzhi Lin, **Andrada-Oana Mandru**, Arthur R. Smith, Noboru Takeuchi, and Hamad A. H. Al-Brithen, *Appl. Phys. Lett.* **104**, 171607 (2014).

9. “Heteroepitaxial Growth and Surface Structure of $L1_0$-MnGa(111) Ultra-thin Films on GaN(0001)”, **Andrada-Oana Mandru**, Reyes Garcia Diaz, Kangkang Wang, Kevin Cooper, Muhammad Haider, David C. Ingram, Noboru Takeuchi, and Arthur R. Smith, *Appl. Phys. Lett.* **103**, 161606 (2013).

10. “Manganese 3 $\times$ 3 and $\sqrt{3} \times \sqrt{3}$-R30° Structures and Structural Phase Transition on w-GaN(000$\bar{1}$) Studied by Scanning Tunneling Microscopy and First-principles Theory”, Abhijit V. Chinchore, Kangkang Wang, Meng Shi, **Andrada Mandru**, Yinghao Liu, Muhammad Haider, Arthur R. Smith, Valeria Ferrari, Maria Andrea Barral, and Pablo Ordejon, *Phys. Rev. B* **87**, 165426 (2013).

11. “Formation of Manganese Delta-doped Atomic Layer in Wurtzite GaN”, Meng Shi, Abhijit Chinchore, Kangkang Wang, **Andrada-Oana Mandru**, Yinghao Liu, and Arthur R. Smith, *J. Appl. Phys.* **112**, 053517 (2012).

Appendix D: List of First-Author Oral/Poster Presentations

1. AVS 62nd International Symposium 2015, San Jose, California; oral presentation - *awarded the 2015 Leo M. Falicov student award*.

2. AVS 62nd International Symposium 2015, San Jose, California; oral presentation - *awarded the 2015 Russell and Sigurd Varian award*.

3. APS March Meeting 2015, San Antonio, Texas; oral presentation.

4. 5th International Conference on Spin-Polarized STM 2014, Huron, Ohio; oral presentation.

5. NQPI/CMSS Joint Poster Session 2014, Ohio University; poster - *awarded first place poster award*.

6. Student Research and Creative Activity Expo 2014, Ohio University; poster - *awarded first place poster award*.

7. APS March Meeting 2014, Denver, Colorado; oral presentation.

8. NQPI Nanoforum Seminar 2013, Ohio University; oral presentation.

9. Student Research and Creative Activity Expo 2013, Ohio University; poster.

10. 29th North American Molecular Beam Epitaxy Conference 2012, Stone Mountain Park, Georgia; poster.

Thesis and Dissertation Services